



**NTNU – Trondheim**  
Norwegian University of  
Science and Technology

# Position controlled Growth of GaAs/AlGaAs core-shell Nanowires - more uniform in their structural and optical Properties?

**Julie Stene Nilsen**

Nanotechnology

Submission date: June 2014

Supervisor: Antonius Theodorus Johann Van Helvoort, IFY

Norwegian University of Science and Technology  
Department of Physics



**Julie Stene Nilsen**

Position controlled Growth of  
GaAs/AlGaAs core-shell  
Nanowires - more uniform in their  
structural and optical Properties?

Master thesis

Trondheim, June 2014

Norwegian University of Science and Technology  
Faculty of Natural Sciences and Technology  
Department of Physics

Supervisor: Associate Prof. A. T. J. van Helvoort

Cover image: GaAs/AlGaAs core-shell nanowire tip imaged in BF TEM mode.



# Abstract

Semiconducting nanowires (NWs), especially those with a direct band gap, could be promising building blocks in future optoelectronic devices. Position controlled, self catalyzed GaAs/AlGaAs core-shell NWs with an AlGaAs axial insert, grown using molecular beam epitaxy, are studied structurally and optically, and compared to similar, but random grown, core-shell NWs as well as position controlled bare-core NWs. The characterization tools used include transmission electron microscopy, photoluminescence, scanning (transmission) electron microscopy, high angle annular dark field scanning transmission electron microscopy and energy dispersive spectrometry. In addition to the effect of growing NWs in regular, predefined patterns, the structure and morphology of the NWs are explained through the growth parameters, and the optical properties studied on the exact same NWs are related to their structure. Position controlled NWs are found to be highly uniform both structurally and optically. The NWs show excitonic emission related to a pure, defect free zinc blende segments. Small, defect related, structural variations seen in the tip and bottom, induced by the growth and consumption of the Ga catalyst droplet, are believed to cause variations in the emission below the free exciton energy. Shell growth is found to cause variations in morphology as well as a varying high energy emission in the range 1.6 - 1.8 eV, which is hypothesized to be due to confined GaAs in the AlGaAs shell.



# Sammendrag

Halvledende nanotråder, spesielt de med direkte båndgap, kan bli lovende byggesteiner for fremtidige optoelektroniske enheter. I dette arbeidet studeres de strukturelle og optiske egenskapene til posisjonskontrollerte, selvkatalyserte GaAs/AlGaAs kjerne-skallnanotråder med et aksielt AlGaAs segment laget med molekylærstråleepitaksi. Disse sammenlignes med lignende kjerne-skall nanotråder som er grodd tilfeldig posisjonert, samt posisjonskontrollerte nanotråder uten skall. Karakteriseringsverktøyene som er brukt inkluderer transmisjonselektronmikroskopi, fotoluminescence, sveipe(transmisjons) - elektromikroskopi, høyvinkel annular mørkefeltssveipetransmisjonselektronmikroskopi og energispredningsspektrometri. I tillegg til å se på effekten av å gro nanotrådene i predefinerte mønstre, brukes vekstparametrene til å forklare nanotrådenes struktur og morfologi, samt relatere strukturen til de eksakt samme nanotrådene til deres optiske egenskaper. Studien viser at posisjonskontrollerte nanotråder er veldig uniforme både strukturelt og optisk. Nanotrådene viste eksitonrelatert emisjon som ble knytta til et defektfritt segment med ren zinc blende-fase. Små, defektrelaterte, strukturelle variasjoner observert i tuppen og bunnen av nanotråden, indusert av vekst og konsumering av Ga-katalysatordråpen, menes å være grunnen til variasjoner i emisjon lavere enn eksitonenergien. Det er også funnet at skallvekst forårsaker variasjoner i morfologi så vel som varierende høyenergiemisjon i området 1.6 - 1.8 eV, som kan tenkes kommer fra bunnede tilstander knytta til områder med lite Al i AlGaAs-skallet.



# Preface

This master thesis work has been carried out at the Department of Physics at the Norwegian University of Science and Technology (NTNU), and is a continuation of the project work carried out in the fall of 2013. The work has been done at the TEM Gemini Center and NTNU Nanolab under supervision from Associate Prof. A.T.J. van Helvoort. The NWs studied in this work are grown in the MBE lab and optically characterized in the Nano Photonics lab at the Department of Electronics and Telecommunication (IET). The growth and optical characterization was conducted by the Nanophotonics group at IET led by Prof. Helge Weman.

First of all, I would like to thank my supervisor. Ton, this work would not have been possible without you. I am forever grateful for all the time you have spent helping me in the lab and answering my emails, even on a sunny Saturday afternoon. I really appreciate the many interesting discussions we have had throughout the year, and all the feedback you have given me on this report. I have learned so much from you, and it has been very inspiring to feel that you really care about my work. Thank you for believing in me and all your encouragement, it has been invaluable for my motivation.

A big thank you also goes to the PhD candidates Johannes Reinertsen and Lyubomir Ahhapodov. First of all for doing the optical characterization of the NWs in this work, but also for the many discussions about the results. A special thanks to Johannes for answering all my questions early and late, it has been appreciated. I would also like to thank Bjørn Gunnar Soleim for assistance on the TEM, and especially for crawling on the floor helping me find the TEM holder piece I had lost.

Lastly, I would like to thank friends and family for supporting me throughout the year; you all know who you are. Thank you for everything from helping me with computer problems, plotting in Python, LaTeX problems and proof-reading, to giving moral support and encouragement. And of course, thank you to the best class mates ever! Coffee breaks, dinners at Timinikontoret, HGDN-tråden; it has all made this work bearable. Thank you for the best five years of my life, it would not have been the same without you.

I hereby declare that this is an independent work in accordance with the regulations at the Norwegian University of Science and Technology.

Trondheim, June 21, 2014

Julie Stene Nilsen

# List of abbreviations

<b>AlGaAs</b>	Aluminum gallium arsenide
<b>BFP</b>	Back Focal Plane
<b>BF</b>	Bright field
<b>CB</b>	Conduction band
<b>CCD</b>	Charged coupled device
<b>CTF</b>	Contrast transfer function
<b>DF</b>	Dark field
<b>DP</b>	Diffraction pattern
<b>EDS</b>	Energy dispersive spectrometry
<b>EHP</b>	Electron hole pair
<b>FCC</b>	face centered cubic
<b>FFP</b>	Front focal plane
<b>FFT</b>	Fast Fourier transform
<b>FIB</b>	Focused ion beam
<b>GaAs</b>	Gallium arsenide
<b>HAADF</b>	High angle annular dark field
<b>HCP</b>	Hexagonal close packed
<b>HRTEM</b>	High resolution transmission electron microscopy
<b>MBE</b>	Molecular beam epitaxy
<b>ML</b>	Monolayer

<b>NIL</b>	Nanoimprint lithography
<b>NW</b>	Nanowire
<b>PL</b>	Photoluminescence
<b>SAD</b>	Selected area diffraction
<b>SC</b>	Self catalyzed
<b>SE</b>	Secondary electrons
<b>SEM</b>	Scanning electron microscopy
<b>SF</b>	Stacking fault
<b>SiN</b>	Silicon nitride
<b>SNOM</b>	Near-field scanning optical microscopy
<b>STEM</b>	Scanning transmission electron microscopy
<b>TEM</b>	Transmission electron microscope
<b>VB</b>	Valence band
<b>VLS</b>	Vapor-liquid-solid
<b>VS</b>	Vapor-solid
<b>WPOA</b>	Weak phase-object approximation
<b>WZ</b>	Würtzite
<b>ZB</b>	Zink blende

# Contents

<b>1</b>	<b>Introduction and motivation</b>	<b>1</b>
<b>2</b>	<b>Theory</b>	<b>3</b>
2.1	Crystallography and electron diffraction . . . . .	3
2.1.1	Lattice types . . . . .	3
2.1.2	Crystal defects . . . . .	5
2.1.3	Reciprocal space . . . . .	5
2.1.4	Diffraction . . . . .	6
2.1.5	Dynamical scattering . . . . .	8
2.2	Electron microscopy . . . . .	10
2.2.1	Scanning electron microscopy . . . . .	11
2.2.2	Transmission electron microscopy . . . . .	12
2.2.3	Scanning transmission electron microscopy . . . . .	17
2.2.4	Energy-dispersive spectrometry . . . . .	18
2.3	Photoluminescence . . . . .	21
2.3.1	Optical properties of semiconductors . . . . .	21
2.3.2	Power dependent PL . . . . .	24
2.4	Nanowire growth . . . . .	25
2.5	Nanowire crystal structure and morphology . . . . .	27
<b>3</b>	<b>Experimental</b>	<b>32</b>
3.1	Nanowire growth . . . . .	32
3.1.1	Sample Main . . . . .	32
3.1.2	Sample BareCore . . . . .	33
3.1.3	Random1, Random2 and Random3 . . . . .	33
3.2	Specimen preparation . . . . .	34
3.3	Optical characterization . . . . .	35
3.4	Structural characterization . . . . .	35
3.5	Data processing . . . . .	36

---

<b>4</b>	<b>Results</b>	<b>37</b>
4.1	Structural characterization of random grown samples . . . . .	37
4.1.1	Sample Random1 . . . . .	37
4.1.2	Sample Random2 . . . . .	38
4.1.3	Sample Random3 . . . . .	40
4.2	Positioned NW growth . . . . .	42
4.3	Sample BareCore . . . . .	44
4.3.1	Phases . . . . .	44
4.3.2	Morphology . . . . .	45
4.4	Sample Main . . . . .	46
4.4.1	Phases . . . . .	46
4.4.2	Morphology . . . . .	49
4.4.3	Defects . . . . .	52
4.4.4	Shell characterization . . . . .	56
4.5	Optical characterization . . . . .	61
4.5.1	Sample Random1 . . . . .	61
4.5.2	Sample Random2 . . . . .	62
4.5.3	Sample Random3 . . . . .	63
4.5.4	Sample Main . . . . .	66
<b>5</b>	<b>Discussion</b>	<b>69</b>
5.1	Morphology . . . . .	69
5.2	Nanowire shell growth . . . . .	73
5.3	Crystal structure, phases and defects . . . . .	76
5.4	Optical properties . . . . .	83
5.5	Method . . . . .	87
<b>6</b>	<b>Conclusions</b>	<b>89</b>
<b>7</b>	<b>Further work</b>	<b>91</b>
	<b>Bibliography</b>	<b>92</b>
	<b>Appendices</b>	<b>97</b>
<b>A</b>	<b>Nanowire structural data</b>	<b>98</b>
<b>B</b>	<b>Indexing diffraction patterns</b>	<b>101</b>
<b>C</b>	<b>HAADF STEM imaging</b>	<b>103</b>

# Chapter 1

## Introduction and motivation

Semiconducting nanowires (NWs) are predicted a bright future due to their novel properties not seen in the bulk material [1, 2] and possible electronic applications, including solar cells [3–5], light emitting diodes [6–8], transistors [9–11] and lasers [12–14]. NWs are easily grown using a vapor-liquid-solid (VLS) mechanism, and can be grown on different types of lattice mismatched substrates due to the small area of contact and strain relaxation on the surface [15]. Commonly, gold is used as a catalyst during growth [16], but recently also the use of Ga-assisted self-catalyzed (SC) NWs have been investigated [17]. The latter has many advantages, including the avoidance of Au deep levels in the NW, but is not yet well understood and optimized as the Au-catalyzed NWs are.

For photovoltaic applications, the use of NWs as the optically active material can give several advantages. Their small size reduces the path the carriers have to travel to the electrodes, thus decreasing the chance of recombination and thereby increasing the solar cell efficiency. NW arrays in solar cells also have the possibility of light trapping [18]. In addition, less active material is needed compared to planar solar cells due to their high surface-to-volume ratio.

High demands to purity are placed on the NWs, as a defect free material is crucial to avoid trapping and non-radiative recombination of charge carriers [19]. To achieve structure optimization, the growth process has to be understood thoroughly. However, as NWs are subject to large variations within a growth batch, and no NW is identical [20], the work of assigning different growth conditions to the resulting structure is challenging. For optoelectronic applications such as solar cells and light emitting diodes, it is important to be able to be able to grow NWs with desirable optoelectronic properties. However, the structural influence on these properties as seen in photoluminescence (PL)

studies has been a heavily debated subject as of late. This is because different studies are often contradicting, and the property-structure relations are not well understood today. Most of the uncertainty is related to the origin of the low energy emission as the peaks are not consistent in the spectrum, but they seem to be defect related. Planar defects are easily detected using transmission electron microscopy (TEM), while point defects are not directly observable. In addition, many of the studies conducted are not done correlated, i.e. different NWs are studied in TEM and PL, and due to the mentioned variations within the growth batch, conclusions from these studies are highly uncertain.

To obtain more uniform properties, the NWs can be grown position controlled on the substrate. This is a relatively new process and limited studies report on the optoelectronic properties or compare random and positioned growth. With equal distance between the NWs on the substrate, scanning electron microscopy (SEM) studies have shown that the NWs display a more uniform morphology [21], which is also believed to give more similar optical properties of the NWs. The aim of this work is to confirm that position controlled NWs are more uniform, both structurally and optically. To do so, NWs grown position controlled are compared with randomly grown NWs of similar type with respect to their crystallographic structure, morphology and optical properties. The growth mechanism is attempted explained, and the optical properties are related to the observed structure of the NWs.

The main sample in this work is GaAs/AlGaAs core-shell NWs grown position controlled, while GaAs core-only position controlled NWs are used as a reference sample. Three random grown samples are studied; they are similar to the main sample, but the NWs do not have an AlGaAs insert. The three samples differs in their V/III ratio. All the NWs are grown through the SC VLS method using molecular beam epitaxy (MBE) and characterized using TEM, PL, scanning (transmission) electron microscopy (S(T)EM), high angle annular dark field (HAADF) STEM and electron dispersive spectrometry (EDS). The PL-TEM study is done correlated, i.e. the exact same NWs are studied with the two techniques. The position controlled growth is achieved by covering the substrate with a SiO<sub>2</sub> mask made using nanoimprint lithography (NIL) and wet etching.

The NWs studied are a part of an ongoing work on the optimization of the growth process. In the end, the NWs should have a highly reproducible structure giving the desired optical properties for photovoltaic devices. This means that the NWs should have a low defect density, and have optical emission related to the free exciton. As randomly grown NWs give large variations in structure, the optical properties are also subject to large variations. As it is crucial for NW based solar cell that all the NWs have the excitonic property, the position controlled NWs in this work are an attempt to see if this is achievable. In addition, this work will give more insight in the growth process and how it affects the properties of the NWs.

# Chapter 2

## Theory

This chapter will provide the theoretical background required to be able to interpret the results presented in this thesis. First, the periodic nature of crystals and how it relates to electron diffraction will be discussed. This is important both to understand the properties of the NWs and how TEM can be used to characterize their internal structure. Furthermore, the different characterization techniques used in this work are explained. The last two sections of the chapter are devoted to explain the growth technique used for the NWs studied, as well as the final NW morphology.

### 2.1 Crystallography and electron diffraction

Crystalline materials are an interesting topic in condensed matter physics due to the properties arising from their periodic structure. In this section, the focus will be on how a crystalline material can be seen in both real and reciprocal space, and relate this to how electrons interact with the material. The following theory is based on Kittel [22] (section 2.1.1 - 2.1.3) and Williams and Carter [23] (section 2.1.4 - 2.1.5) unless otherwise stated.

#### 2.1.1 Lattice types

The atoms in a crystal are organized in a lattice constituted by repetitive units. The smallest repetitive unit in a crystal is called a unit cell. A basis is associated with each lattice point in the unit cell and can consist of one or more unique atoms. It is defined by the translation vectors  $\mathbf{a}_1$ ,  $\mathbf{a}_2$  and  $\mathbf{a}_3$ . The position of an atom in the basis relative to the associated lattice point can be expressed as

$$\mathbf{r}_j = x_j \mathbf{a}_1 + y_j \mathbf{a}_2 + z_j \mathbf{a}_3 \quad (2.1)$$

where the origin normally is arranged so that  $0 \leq x_j, y_j, z_j \leq 1$ . Zinc blende (ZB) is a common structure for semiconductor crystals, and is one of the crystal phases of GaAs. It has two different atoms in the basis (Ga and As), located at  $(x_j, y_j, z_j) = (0, 0, 0)$  and  $(\frac{1}{4}, \frac{1}{4}, \frac{1}{4})$ . Another GaAs crystal phase structure is Würtzite (WZ), which also has two atoms in the basis. These are located at  $(x_j, y_j, z_j) = (0, 0, 0)$  and  $(\frac{2}{3}, \frac{1}{3}, \frac{1}{2})$ .

Lattice types are defined according to the relative lengths of the translation vectors and the angles between them. In a cubic lattice, the translation vectors are of equal lengths  $a_1 = a_2 = a_3$ , and the angles between these vectors are all  $90^\circ$ . The ZB structure has a face centered cubic (FCC) lattice, and with two atoms in the basis it has a crystal structure as illustrated in fig. 2.1 (a). Figure 2.1 (b) shows that the WZ structure has a hexagonal close-packed (HCP) lattice, which is another lattice type. The system is described by four vectors where  $a_1 = a_2 = a_3 \neq c$ , and the angles between  $\mathbf{a}_1$ ,  $\mathbf{a}_2$  and  $\mathbf{a}_3$  are  $120^\circ$ .

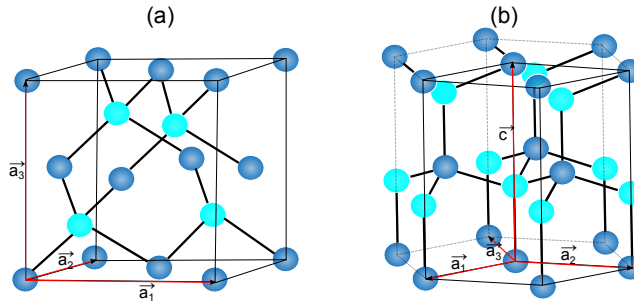


**Figure 2.1:** Unit cell of the (a) ZB and (b) WZ structure. ZB has a FCC structure with two different atoms in the basis. WZ is a hexagonal structure with two atoms in the basis.

A crystal plane is defined as how it cuts the axis of the lattice vectors  $\mathbf{a}_1$ ,  $\mathbf{a}_2$  and  $\mathbf{a}_3$ , and is named by the Miller indexing system. The Miller indices  $(hkl)$  are found by taking the reciprocal of the intercepts of the axis, and finding the smallest whole numbers with the same ratio. Hexagonal lattices are normally described by the Miller- Bravais system, which uses four indices  $(hkil)$ , where  $i = -(h + k)$  [24]. As seen in fig. 2.1 (b), the system is based on four axis, where  $\mathbf{a}_1$ ,  $\mathbf{a}_2$  and  $\mathbf{a}_3$  are in the same plane, called the basal plane, which the fourth axis is perpendicular to.

The crystallographic direction is given by the vector  $[uvw]$ , and correspond to the projections along the  $\mathbf{a}_1$ ,  $\mathbf{a}_2$  and  $\mathbf{a}_3$  directions. For the hexagonal crystal, the conversion to the four index system  $([u'v'w'])$  to  $[uvtw]$  is as follows [24]:

$$\begin{aligned}
u &= \frac{1}{3}(2u' - v') \\
v &= \frac{1}{3}(2v' - u') \\
t &= -(u + v) \\
w &= w'.
\end{aligned} \tag{2.2}$$

The inter planar spacing between equivalent planes for a cubic cell ( $a_1 = a_2 = a_3 = a_0$ ) is

$$d_{hkl} = \frac{a_0}{\sqrt{h^2 + k^2 + l^2}}. \tag{2.3}$$

For the HCP lattice the same distance is given as [25]

$$1/d_{hkl}^2 = \frac{4}{3a^2}(h^2 + k^2 + hk) + \frac{l^2}{c^2}. \tag{2.4}$$

### 2.1.2 Crystal defects

When determining the stacking sequence for crystals, one commonly considers the close packed plane, or in other words, the [111] direction for ZB and the [0001] direction for WZ. The ZB structure has the *ABCABCABC* stacking sequence, while WZ has the sequence *ABABAB*. Each letter (*A, B, C*) represents a basis containing both a Ga and an As atom. However, during NW growth, crystal defects such as stacking faults (SFs) and twinning might occur. Twinning is the most common defect in the ZB phase, and is a rotation around the  $\langle 111 \rangle$  axis. The stacking sequence will then be *ABCABCBACBA*, i.e. *C* becomes a mirror plane of the stacking sequence. Twinning might occur in WZ too, giving a *ABABBABA* stacking sequence.

A SF is defined as a single, additional layer or a single missing layer in an otherwise perfect crystal [26], and is the most common defect type in the WZ phase. A SF in WZ might for example be *ABABCAB*, giving one layer of ZB stacking (*ABC*) in the WZ structure. For ZB, a SF might be *ABCACBABC*, where two of the planes are interchanged.

If the stacking sequence is alternating between different types, it is called polytyping and is considered a separate phase. In GaAs NWs, the most common polytype sequence is *ABACABAC* which is named 4H after the Ramsdell notation [27].

### 2.1.3 Reciprocal space

As the crystal lattice consists of repetitive units, it is ideal for Fourier analysis. When expanding an arbitrary function  $n(x)$  in one dimension with period  $a$ ,

$$n(x) = n_0 + \sum_{p>0} [C_p \cos(2\pi px/a) + S_p \sin(2\pi x/p)] = \sum_p n_p \exp(i2\pi x/a), \quad (2.5)$$

where  $p$  is an integer and  $C_p$  and  $S_p$  are the Fourier coefficients, the factor  $2\pi p/a$  tells what terms in the Fourier series are allowed and are called the reciprocal lattice points. Extending this to three dimensions one gets the local electron concentration

$$n(\mathbf{r}) = \sum_{\mathbf{G}} n_{\mathbf{G}} \exp(i\mathbf{G} \cdot \mathbf{r}) \quad (2.6)$$

with

$$\mathbf{G} = v_1 \mathbf{b}_1 + v_2 \mathbf{b}_2 + v_3 \mathbf{b}_3 \quad (2.7)$$

being the reciprocal lattice vector ( $v_1$ ,  $v_2$  and  $v_3$  are integers).  $\mathbf{b}_1$ ,  $\mathbf{b}_2$  and  $\mathbf{b}_3$  are the primitive vectors of the reciprocal lattice and shows the connection between real and reciprocal space:

$$\mathbf{b}_1 = 2\pi \frac{\mathbf{a}_2 \times \mathbf{a}_3}{\mathbf{a}_1 \cdot \mathbf{a}_2 \times \mathbf{a}_3}; \quad \mathbf{b}_2 = 2\pi \frac{\mathbf{a}_3 \times \mathbf{a}_1}{\mathbf{a}_1 \cdot \mathbf{a}_2 \times \mathbf{a}_3}; \quad \mathbf{b}_3 = 2\pi \frac{\mathbf{a}_1 \times \mathbf{a}_2}{\mathbf{a}_1 \cdot \mathbf{a}_2 \times \mathbf{a}_3}. \quad (2.8)$$

### 2.1.4 Diffraction

Electron diffraction is closely related to the reciprocal space through the diffraction condition. When a beam with wave vector  $\mathbf{k}$  hits a crystal lattice, it will experience a phase shift of

$$\Delta \mathbf{k} = \mathbf{k}' - \mathbf{k} \quad (2.9)$$

where  $\mathbf{k}'$  is the scattered wave vector. The scattering amplitude is given by [22]

$$A_{scattering} = \sum_{\mathbf{G}} \int dV n_{\mathbf{G}} \exp[i(\mathbf{G} - \Delta \mathbf{k}) \cdot \mathbf{r}], \quad (2.10)$$

which is maximum for  $\Delta \mathbf{k} = \mathbf{G}$  and approximately zero otherwise. As can be seen from fig. 2.2, only certain points in the reciprocal space will have a scattering amplitude, depending on the angle  $\theta$  between the incoming wave vector  $\mathbf{k}$  and the crystal plane. This is when the diffraction condition is met (Bragg's law in reciprocal space):

$$\Delta \mathbf{k} = \mathbf{g}_{hkl}, \quad (2.11)$$

where

$$\mathbf{g}_{hkl} = h\mathbf{b}_1 + k\mathbf{b}_2 + l\mathbf{b}_3 \quad (2.12)$$

is a reciprocal lattice vector representing a set of parallel planes in real space with inter planar distance  $d_{hkl}$ . The latter can be found when comparing the diffraction condition with Bragg's law,  $2d \sin \theta = n\lambda$ , for an elastic scattering event. When the scattering from all the crystal planes are put together, one gets a diffraction pattern (DP) unique for the crystal structure.

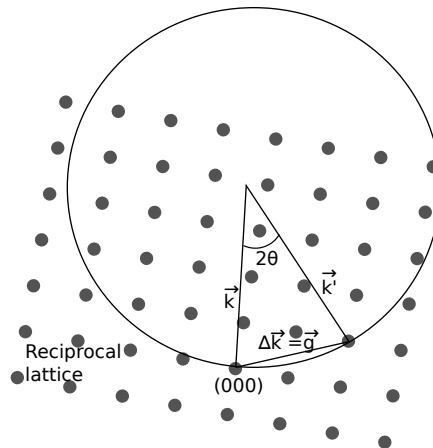


**Figure 2.2:** A 2D representation of the Ewald sphere in reciprocal space. All reflections lying on the sphere will be visible in the DP, which is when the diffraction condition is met. The radius of the sphere is equal to the incoming wave vector  $\mathbf{k}$ .

Since the length of  $\mathbf{g}_{hkl}$  is  $1/d_{hkl}$ , what is big in real space will be small in reciprocal space, and vice versa. In reality, a diffraction spot (from now on called a reflection) might be visible in the DP even though the diffraction condition is not met exactly. Due to the thin TEM specimen, the reflections are associated with a reciprocal lattice rod, called a relrod, see fig. 2.3. A deviation parameter  $\mathbf{s}$  is used to describe how big the difference can be and still have a reflection:

$$\Delta\mathbf{k} = \mathbf{g}_{hkl} + \mathbf{s}. \quad (2.13)$$

If  $\Delta\mathbf{k}$  is within the relrod, the reflection will have an intensity, but maximum intensity is when  $s = 0$ .

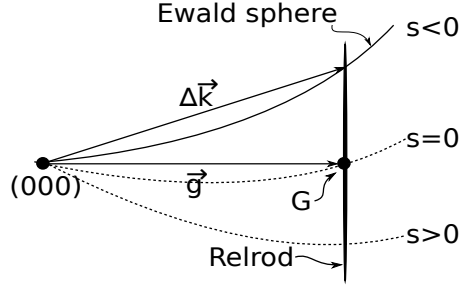


**Figure 2.3:** Schematic of the deviation from diffraction condition. The reflection in reciprocal space will be rod shaped as the specimen is thin. If the Ewald sphere is within the relrod, the reflection will be visible in the DP. The deviation parameter  $s$  tells how far one is from the diffraction condition.  $s$  is negative if the reciprocal lattice point is outside the sphere, and positive if it is inside.

When the diffraction condition in (2.11) is satisfied, the scattering amplitude (2.10) for a crystal with  $N$  repetitive units and  $j$  atoms in each unit, may be written as  $A_{scattering} = NF_{\mathbf{g}_{hkl}}$  [22] where

$$F_{\mathbf{g}_{hkl}} = \sum_j f_j \exp(-i\mathbf{g}_{hkl} \cdot \mathbf{r}_j) = \sum_j f_j \exp[i2\pi(hx_j + ky_j + lz_j)] \quad (2.14)$$

is the structure factor of the basis and

$$f_j = \int dV n_j(\mathbf{r} - \mathbf{r}_j) \exp[-i\mathbf{g}_{hkl} \cdot (\mathbf{r} - \mathbf{r}_j)] \quad (2.15)$$

is the atomic scattering factor. The latter is a measure of the scattering power of one atom in the unit cell and depends on the electron distribution of the atom and the incident angle of the incoming wave. For low angle elastic scattering the atomic scattering factor depends on the atomic number, the electron wavelength and the scattering angle. The structure factor gives the intensity of the reflection as  $I \propto F^2$ . A reflection will be visible in the DP if  $F \neq 0$ . For  $F = 0$ , so called extinction rules for a crystal structure can be determined. Extinction rules for ZB and WZ are given in section 2.5.

### 2.1.5 Dynamical scattering

Up until now, diffraction has been treated kinematically; each reflection is a result of one single scattering event. In TEM, however, the incoming beam will experience multiple scatterings before it exits the specimen. In GaAs, the kinematic theory would hold for a 2 nm thick specimen, while the NWs in this

work are more than 100 nm thick. When a beam has been diffracted by a plane once, it is necessarily in perfect orientation to be diffracted again by the same set of planes, as seen in fig. 2.4. The beam will then be diffracted back into the direct beam, which again will be rediffracted. The chance of this happening many times increase with specimen thickness. In other words, the structure factor is not enough to predict what reflections will be visible in the DP as refraction, extinction and interference effects must be taken into account.

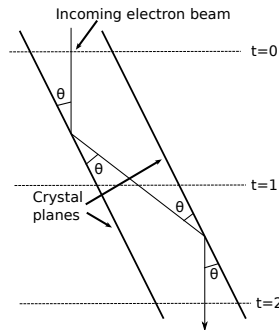


**Figure 2.4:** When the electron beam is diffracted by a crystal plane, it will be in perfect position to be rediffracted back into the direct beam by the adjacent plane.  $t$  is the thickness of the specimen. For  $0 < t < 1$  the kinematic theory holds.

In kinematic scattering, the intensity of the diffracted beam is given by

$$I_{\mathbf{g}} = \left( \frac{\pi}{\xi_{\mathbf{g}}} \right)^2 \frac{\sin^2(\pi t s)}{(\pi s)^2} \quad (2.16)$$

where  $t$  is the specimen thickness,  $s$  is the previously mentioned deviation parameter and  $\xi_{\mathbf{g}}$  is the extinction length;

$$\xi_{\mathbf{g}} = \frac{\pi V_c \cos \theta_B}{\lambda S_{\mathbf{g}}}. \quad (2.17)$$

$\xi_{\mathbf{g}}$  depends on the incident angle  $\theta_B$ , the unit cell volume  $V_c$  and structure factor  $S_{\mathbf{g}}$ , making the intensity  $I_{\mathbf{g}}$  proportional to the square of the structure factor of reflection  $\mathbf{g}$  as stated earlier. In the dynamical theory, however, the deviation parameter is replaced by an effective extinction error;

$$s_{\text{eff}} = \sqrt{s^2 + \frac{1}{\xi_{\mathbf{g}}^2}}. \quad (2.18)$$

The dynamical theory is complex and many approximations are used to deduce this simple result. One of them is the two beam approximation where

only the direct beam and one diffracted beam are considered. The idea is that the amplitude of the two beams depends on the amplitude of both beams, and that they are constantly changing, i.e. they are dynamic. The relation between the intensity of the direct and diffraction beam would be  $I_{000} = 1 - I_g$ . The two beam condition is however impossible to meet for a thin TEM specimen, as can be seen in DPs where there is always more than one diffracted spot visible. However, despite its limitations, it is useful for giving insight in the complex scattering process.

## 2.2 Electron microscopy

The term electron microscopy refers to a series of techniques that uses an electron probe to analyze a material. When this electron probe interacts with the material, many different signals are emitted and can be detected, which is illustrated in fig. 2.5. The main difference between the various electron microscopy techniques lies in what signals they utilize, in addition to smaller differences on how the probe is created and how the signal is detected. The theory in this section is based on [23], except section 2.2.1 which is based on [28].

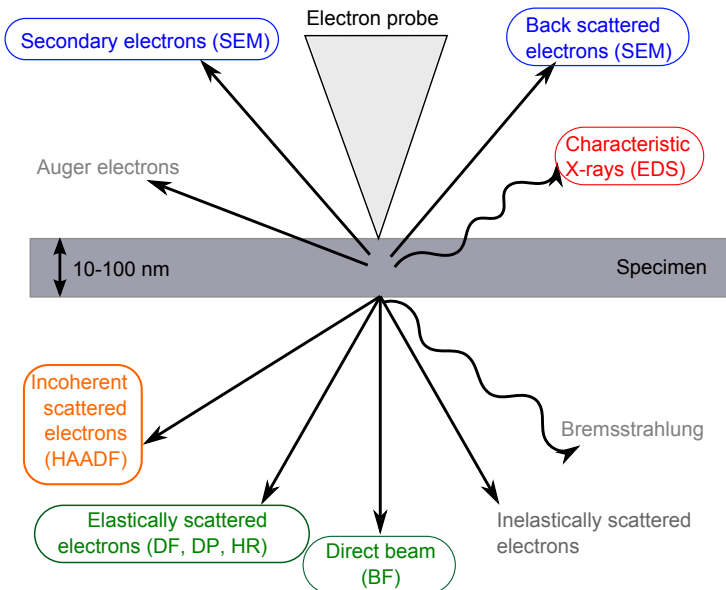


**Figure 2.5:** The different signals produced when an electron probe hits a thin specimen. The figure indicates what signals are used for the different characterization techniques described in this theory.

### 2.2.1 Scanning electron microscopy

Scanning electron microscopy (SEM) uses a focused electron probe to scan the surface in two directions and detect the secondary and the backscattered electrons. The probe must be as small as possible as the resolution can never be better than the diameter of the probe. A schematic of the SEM lens system can be seen in fig. 2.6 (a). The condenser lenses are used to make the beam convergent, while the objective lens makes the final electron focus point very sharp (about 1 nm, smaller for a field emission gun source (explained in TEM)). The scan coils are used to translate the beam across the specimen during scanning. The detector(s) can be placed either as shown in the figure, or it might be an in-lens system where the detector(s) are placed in the middle of the lens system and the specimen within the magnetic field of the lenses. The latter gives a better resolution due to less electrostatic distortion.

When the accelerated electrons enters the specimen, many of them will be inelastic scattered. A chain of scattering events will lead to the electrons gradually losing their kinetic energy, and the distance they reach into the material before they are absorbed is called the penetration depth. The interaction volume, which is the volume in which the scattering happens, depends on the energy of the incoming electrons ( $E_0$ , typically 1- 30 kV), as well as the average atomic number  $Z$  of the atoms in the material (fig. 2.6 (b)). The dependency is illustrated by the following approximate formula:

$$\rho R \approx aE_0^r \quad (2.19)$$

where  $R$  is the penetration depth,  $\rho$  is the density of the material,  $E_0$  is the incident electron energy in keV,  $r \approx 1.35$  and  $a \approx 10\mu \text{ g/cm}^2$ .

Secondary electrons are loose outer shell electrons that easily can gain enough kinetic energy from the scattering process to be ejected from the material. Since only the secondary electrons in the surface region are able to actually escape from the material and be detected by the electric field of the detector, the secondary electrons mainly give a topographical contrast in the image. Elevations on the sample will have a bright outline in the image as electrons on the edges will have higher chances of escaping. Also, the angle between the incoming beam and the topographical feature is important, as this may cause shadowing effects. In addition, asymmetry will often arise as the detector is located on one side of the column and give shadowing in the image. An in-lens detector, however, will give no shadowing effects, but less topographical contrast. The latter type of detector will also only capture the secondary electrons created by the incident beam, and thus give better resolution than the conventional detector, which also captures secondary electrons created by other secondary electrons.

Backscattered electrons (BSE) are electrons being elastically scattered more than  $90^\circ$  and re-enters the vacuum surrounding the sample. Such high angle

elastic scattering is proportional to the square of the atomic number, and the images will thus give contrast due to variation in composition. As heavier elements scatter more, they will also appear brighter in the image. The BSE signal comes from deeper in the material (about half the penetration depth) and therefore gives little topography contrast.

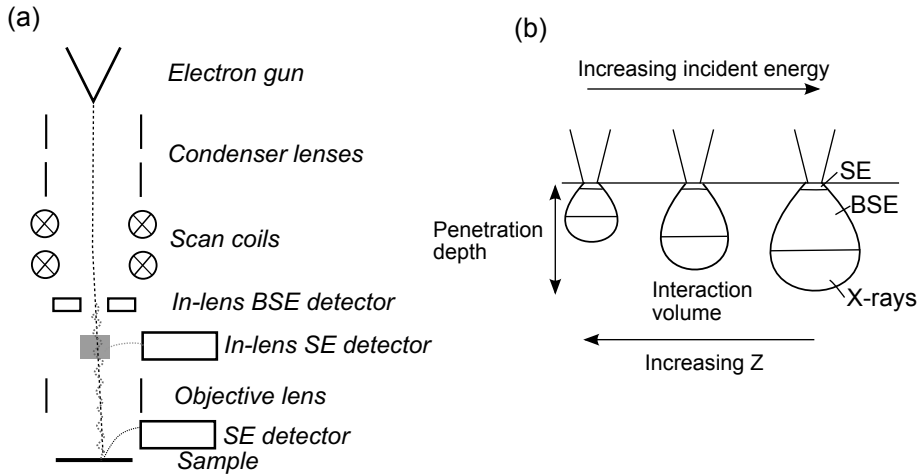


**Figure 2.6:** (a) Schematic of the electron column in a SEM. (b) Schematic of how the interaction volume and penetration depth changes with increasing energy of the incident electrons and decreasing atomic number.

## 2.2.2 Transmission electron microscopy

Contrary to the SEM, the TEM uses the transmitted signals for imaging, which in normal mode means the direct (non scattered) beam as well as the elastically scattered beam. For optimum imaging, the electron beam needs to be parallel, and a schematic of a system to create such a beam is presented in fig. 2.7. The electron source can either be thermionic or a field-emission source. For thermionic emission, the electron source, which is either a W filament or a LaB<sub>6</sub> crystal, is heated up until the electrons have high enough energy to escape the surface. The electron source in a field emission gun is always W, and electrons are generated by applying a large potential between the source and an anode. The acceleration voltage is between 100 - 300 kV, as the electrons must have high enough energy to be transmitted through the specimen.

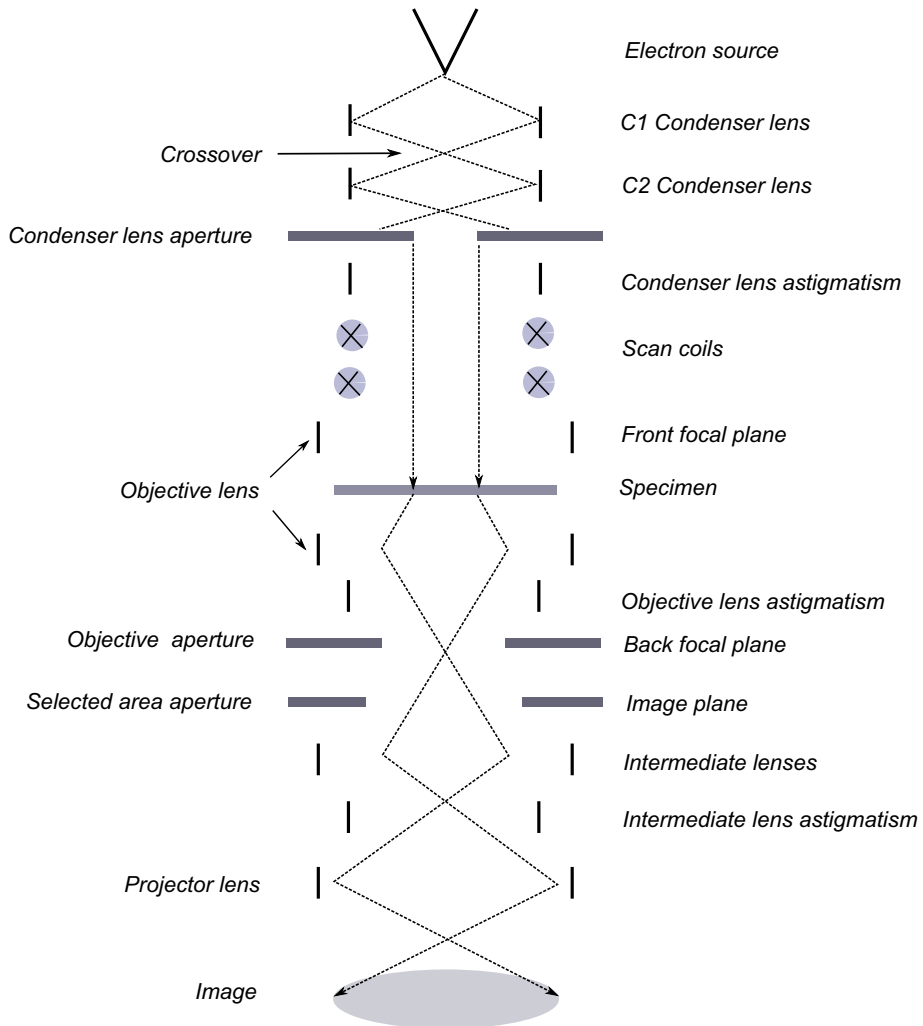


**Figure 2.7:** Ray diagram for a transmission electron microscope. Above the specimen, the lenses and apertures create an optimum electron beam, while the lenses below the specimen transmits and magnifies the image onto the viewing screen.

The condenser lenses are used to create either a parallel or convergent beam, depending on what mode the TEM is to be used in. The first crossover (called spot), which is an image of the electron source, acts as the object for the first condenser lens (C1). To create a parallel beam, the second condenser lens (C2) creates an image of the crossover in the front focal plane (FFP) of the upper

objective lens. For a convergent beam, C2 focuses the image of the crossover on the specimen rather than in the FFP. The condenser lens aperture is inserted to make the electron beam more parallel, as it selects only the central part of the beam. Astigmatism arises when the beam is not perfectly round, and is corrected for by the condenser lens astigmatism as well as the other astigmatism lenses. The scan coils are used to tilt or translate the beam, which is essential in center dark field imaging. This will be discussed later.

After the beam is transmitted through the specimen, the lower objective lens disperses the scattered and direct electrons to create the DP in the back focal plane (BFP), before they are recombined to form an image in the image plane. The objective aperture can be used to select either the direct beam or one of the diffracted beams, depending on the desired operation mode. The selected area aperture is used to reduce the area of the specimen contributing to the DP (called selected area diffraction (SAD)). As the DP is important in determining the different crystal phases and orientations in the NWs, being able to choose what part of the specimen the DP originates from enables the determination of where the different phases are present. The intermediate and projector lenses are used to change the magnification of the image of the specimen on the viewing screen. The strength of the intermediate lenses also determines if the DP or the image will be projected on the screen, as well as their magnification.

### **Contrast mechanisms in TEM**

The contrast in TEM is governed by different mechanisms, and which of them is dominating depends on the conditions the microscope is operated in. The contrast mechanisms are mainly divided into two groups; amplitude contrast and phase contrast, both of which will be explained below.

There are two types of amplitude contrast; mass-thickness contrast and diffraction contrast. Either one can be chosen to be the dominating mechanism in the image by using the objective aperture. If the aperture selects only the central beam in the DP, mass-thickness contrast will dominate the image as only the directly transmitted and low angle scattered electrons are selected. Areas with high mass or thickness will appear dark in the image, as these areas will scatter the electrons more and the aperture will exclude them from the image. For the same reason, thin or low mass areas will appear bright as they scatter less. The microscope is then said to be in bright field (BF) mode, and is illustrated in fig. 2.8 (a).

Diffraction contrast arises from the variation in coherent elastically scattering at certain Bragg angles, and is the main contrast mechanism for crystalline samples. Diffraction contrast is the dominating contrast mechanism in dark field (DF) mode, where the objective aperture selects only one of the diffraction spots in the DP. Only the atomic planes corresponding to this reflection will appear bright in the image. To avoid astigmatism in DF imaging, the

beam should be tilted so that the desired reflection is in the center of the image, rather than shifting the objective aperture, as illustrated in fig. 2.8 (b).

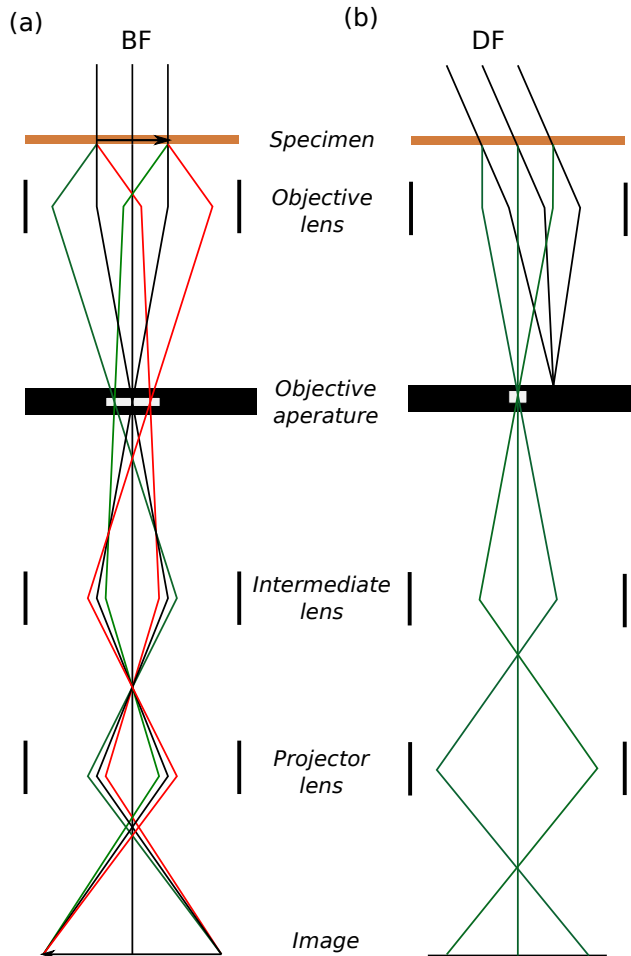


**Figure 2.8:** Ray diagram showing the difference between BF and DF imaging. In BF mode, the direct beam is selected with the objective aperture, while a diffracted beam is selected in DF mode. However, the beam is tilted in DF mode so that the selected beam is on the optical axis..

Two effects seen in TEM caused by diffraction contrast are thickness fringes and bending contours, which is also often observed when imaging NWs. Bending contrast arises because whether the diffraction condition is fulfilled or not will vary with the bending of the specimen. The planes aligned with the incom-

ing beam will appear dark in the image, but the bending will create a gradual transition to planes fulfilling the diffraction condition. As understood from (2.16), the intensity changes with the deviation parameter, and contours will be seen in the image.

Thickness fringes are a result of changing thickness of the specimen. As the NWs are imaged from the side, the electrons will experience the NW as thinner on the edges than in the middle, and fringes will be visible in the image. These fringes are also understood from (2.16), as the intensity varies with sinus squared of the thickness. The periodicity of the fringes is related to the extinction distance  $\xi_g$  [29]. As this parameter is material dependent, the distance between the fringes will be different for each material.

The last important contrast mechanism in regular TEM imaging, phase contrast, arises due to interference between two or more electron beams with different phases, and is the basis of high resolution (HR) TEM imaging. The intensity will vary sinusoidally with a periodicity related to  $1/g$ , and therefore the distance between the interference peaks is related to the inter planar spacing  $d_{hkl}$ . When the material is aligned on a zone axis, the atomic columns will be seen as bright spots on a dark background in the image. How the information from the specimen is transferred to the image is described by the contrast transfer function (CTF)

$$T(\mathbf{u}) = A(\mathbf{u})E(\mathbf{u})2 \sin \chi(\mathbf{u}) \quad (2.20)$$

where  $\mathbf{u}$  is the reciprocal lattice vector.  $A(\mathbf{u})$  represents the apertures,  $E(\mathbf{u})$  expresses the attenuation of the wave, while the aberration of the lens is represented by  $2 \sin \chi(\mathbf{u})$ .  $\chi(\mathbf{u})$  is the phase distortion function

$$\chi(\mathbf{u}) = \pi \Delta f \lambda u^2 + \frac{1}{2} \pi C_s \lambda^3 u^4. \quad (2.21)$$

However, this is only an approximation where only the two most important terms are included.  $\Delta f$  is the defocus value changed by the operator,  $\lambda$  is the electron wavelength and  $C_s$  is the spherical aberration representing the lens quality, which is important due to imperfections of the magnetic lenses.  $C_s$  is fixed and instrument dependent. When deriving this expression, the weak phase-object approximation (WPOA) is used, which is a major simplification. The WPOA states a linear relationship between the amplitude of the CFT and the projected potential of the specimen. This is true for very thin specimens, but in reality the specimen is not thin enough to meet this criterion. Figure 2.9 shows a qualitative sketch of the CTF, where  $T(\mathbf{u}) < 0$  means positive contrast and the spots representing the atoms are dark. The point where the curve crosses the x-axis for the first time represents the resolution limit for when dark spots can directly be interpreted as atoms. Below this point, the image must be interpreted by simulation software as  $T(\mathbf{u})$  changes sign with spatial frequency. The information limit is defined as where the CTF approaches zero.

Above the resolution limit, there is an optimal value for  $\Delta f$  where the phase is almost constant for all the beams, which is given by the Scherzer defocus:

$$\Delta f_{Sch} = -1.2(C_s \lambda)^{1/2}. \quad (2.22)$$

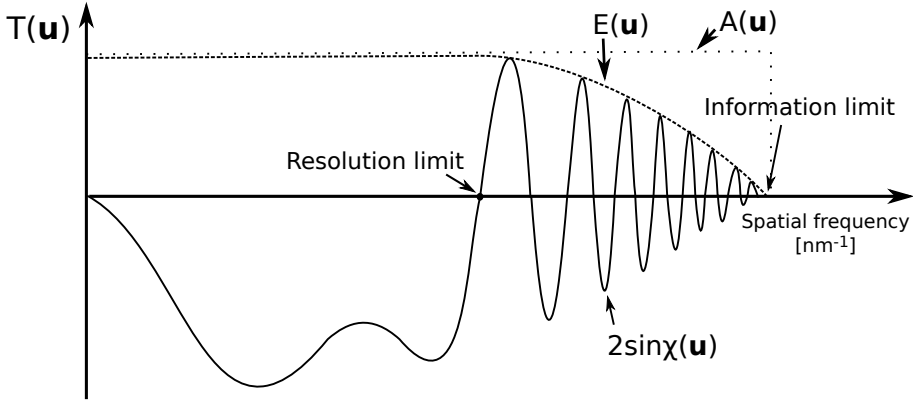


**Figure 2.9:** Qualitative sketch of the contrast transfer function  $T(\mathbf{u})$  (CTF) which is a product of  $A(\mathbf{u})$ ,  $E(\mathbf{u})$  and  $2\sin\chi(\mathbf{u})$  representing the apertures, attenuation of the wave and aberration of the lenses, respectively. The latter function is cut off and damped by the two first. Where the CTF crosses the x-axis for the first time represents the point-to-point resolution, while the information limit is where the CTF approaches zero.

### 2.2.3 Scanning transmission electron microscopy

Scanning transmission electron microscopy (STEM) is very similar to TEM, except that it uses a focused, scanning electron probe instead of a parallel beam. The beam needs to be parallel to the optic axis at all times as the diffraction condition will change if the beam hits the specimen from an angle. To achieve this, a smaller condenser aperture is inserted, and two sets of scan coils shift the beam twice before a third condenser lens ensures that the electrons are parallel when hitting the surface. An image of the C1 crossover is then formed in the specimen plane, and a constant DP is formed in the BFP even if the beam is scanning. Hence, the resolution in a STEM is limited by the beam dimensions just like in SEM, except that the interaction volume is a very thin disk. The resolution is not dependent on the imaging lenses below the specimen as in TEM, in fact, they might as well be absent.

The detector system in STEM is also different than in TEM. Instead of inserting an objective aperture, an electron detector below the specimen is used to select the electrons scattered over a certain angle range. The detector

is places to select only the BF (the central part of the DP) or DF (scattered) signal, as seen in fig. 2.10. The image is not projected onto a viewing screen, but rather built on the computer screen, as the computer knows at any given time what area is being illuminated. For DF imaging, an annular detector is used. The ADF detector actually surrounds the BF detector as a ring, picking up all electrons scattered at a certain angle.

Yet another detector can be used in STEM, picking up electrons scattered at a larger angle than what the DF detector picks up. This technique is called high angle annular dark field (HAADF) STEM, and utilizes the incoherent scattered electrons. The diffraction contrast effect will be greatly reduced, while mass-thickness contrast will be dominating if the detector only gathers electrons scattered more than  $\sim 3^\circ$ . The scattering angle range can be changed by adjusting the distance between the detector and the specimen or the camera length if lenses are present below the specimen

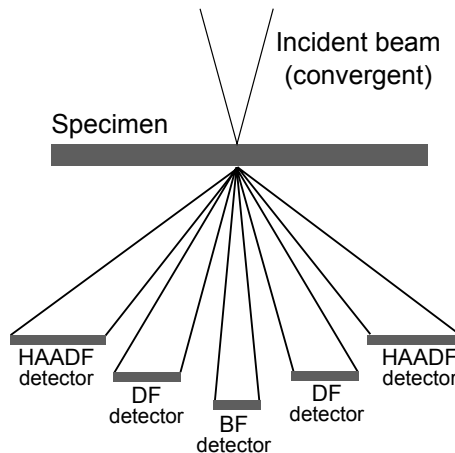


**Figure 2.10:** Schematic of the different detectors that can be used in a STEM. The BF and DF detector gathers the directly transmitted and elastically scattered electrons, respectively. The HAADF detector gathers the incoherent scattered electrons.

## 2.2.4 Energy-dispersive spectrometry

Energy dispersive spectrometry (EDS) utilize the characteristic X-rays to analyze which elements are present in the specimen. As can be seen from fig. 2.6 (b), the interaction volume for X-rays is larger than that for electrons, and hence, for thick or bulky specimens, the spatial resolution is poorer. When an electron is inelastically scattered, it interacts with an inner-shell electron in the atom. If enough energy is transferred from the incoming electron, the core electron can be excited to a higher energy state and leave a hole in the

inner shell. The now ionized atom returns to its original energy state by filling the hole with an electron from an outer shell. In this process, an X-ray can be emitted (alternatively an Auger electron), characteristic of the energy difference between the inner hole and the outer shell electron filling the hole. This energy difference is unique for that transition and hence for that atom. A schematic of the process can be seen in fig. 2.11. The critical ionization energy ( $E_c$ ) is the energy the electron beam must transfer to the inner shell electron in order to eject it from the atom, and atoms with higher mass will have a higher  $E_c$ . The energy of the X-ray peaks in the spectrum will also increase with atomic number. As there are many possible transitions in an atom, there are several X-ray energies associated with each atom. The relationship between X-ray wavelength and atomic number  $Z$  is given by the following formula

$$\lambda = \frac{B}{(Z - C)^2} \quad (2.23)$$

where  $B$  and  $C$  are constants. When the hole created by the incident electron is filled with an electron from an outer shell, a new hole is generated. This hole is filled creating a new X-ray, and the process continues until a hole is filled with a free electron.

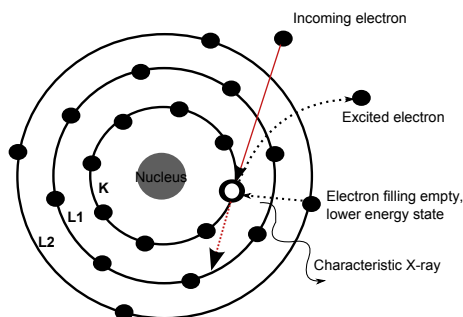


**Figure 2.11:** Schematic picture of how characteristic X-rays are created in an atom. The incoming electron excites an inner shell electron so it escapes the attractive field of the nucleus. An outer shell electron fills the empty energy state, and in doing so the excess energy is emitted as an X-ray characteristic for the energy difference between the two states.

There is a separate nomenclature system for naming the different transitions in an atom. The shells in an atom are named from K to O, where K is the innermost shell. Each shell consist of several subshells, except the K shells which only has one level. The transition is given the capital letter K-O depending on in which of the shells the hole that is filled is located. The letter is sub-named depending on the original energy level of the electron filling the hole. If the electron came from the L shell it is named  $\alpha$ , from the M and N

shells it is named  $\beta$ , while it is named  $\gamma$  if it is from the O shell. The Greek index letter is numbered from 1-5 depending on which subshell the electron is coming from. So a transition from the outermost L shell to the K shell would be named  $K_{\alpha_1}$ .

The incoming electron might interact with the nucleus instead of an electron, a process that may create an X-ray as well. These X-rays are called bremsstrahlung and is seen as a continuous background noise in the X-ray energy spectrum.

The X-ray energy is analyzed by a detector located above the specimen. The detector generates a charged pulse proportional to the X-ray energy, which in turn is changed into a voltage, amplified and identified electronically. The computer assigns the signal to the appropriate energy channel. The number of pulses, or counts, in each channel are turned into a spectrum showing counts versus energy, which is readable for the user. A typical microscope uses 2048 channels with an energy range of 5-10 eV per channel, but the energy resolution is about 140 eV. Therefore, it could be that some peaks overlap.

When doing EDS analysis, it is important to be aware of artifacts present in the energy spectrum, for example peaks from elements not present in the illuminated area. There are two possible reasons for such peaks. One is that the signal is due to spurious X-rays, which are coming from the specimen, but not generated by the incident beam, i.e. generated by bremsstrahlung X-rays and scattered electrons. The other possibility is that the signal is coming from system X-rays, which are produced by scattered electron hitting other things than the specimen, e.g. the holder. This can for example cause a Cu signal in the spectrum.

Several artifacts in EDS can also arise during signal detection and processing. An example of a detection artifact is an escape peak, which comes from a small loss in energy of an X-ray in the detector, i.e. not turned into an electron hole pair (EHP). The peak will then show a lower energy than the true energy in the spectrum. Processing artifacts can for example arise when the count rate is higher than the detector's ability to distinguish between individual signals. However, this should not be a problem if the count rate is less than 10 000 channels per second (cps).

When doing EDS analysis, it is possible to quantify the relative amounts of each element, and not just qualitatively state that it is present. If the intensities  $I$  of two elements A and B above the background (i.e. the area under the peak in the spectrum) are measured, the weight percent ratio of each element is given by the following formula

$$\frac{C_A}{C_B} = k_{AB} \frac{I_A}{I_B}. \quad (2.24)$$

$k_{AB}$  is the sensitivity factor dependent on the atomic number as well as the TEM-EDS system and the acceleration voltage, and is thus not a constant. The

latter is important as the energy of the incident beam determines the size of the interaction volume and therefore the area from which the signal is generated. For the best possible quantification, it is important to get rid of as much of the artifacts as possible. For example, the specimen should not be tilted to avoid spurious electrons. In this work, the NWs are often tilted to be aligned on zone, however, this will make the EDS signal less reliable as the X-rays are generated in a slightly different area than the one directly below the surface illuminated.

## 2.3 Photoluminescence

Photoluminescence (PL) is a method for characterizing the optoelectronic properties of the material. In short, it is a non-destructive technique where light is used to excite electrons and create EHPs in the material, and study the emission from the recombination process. In this section, a short introduction to the optical properties of semiconductors will be given as a background to understand the spectra presented in the results section, followed by a description of power dependent PL, which is the technique used for this work. The theory is based on [30] unless otherwise stated.

### 2.3.1 Optical properties of semiconductors

As PL measures the radiative emission from quantized transitions between states in or close to the conduction band (CB) to states in or close to the valence band (VB), the band structure (dispersion relation) of the material is determining for its properties. Due to the Pauli exclusion principle, which states that two fermions can not be in the same one-particle state [31], the distribution of energy levels are split into bands. The band structure is complex and dependent on the interatomic spacing in the material, however, a simplistic view of the bands can be seen in fig. 2.12. The energy difference between the VB and the CB constitutes the band gap energy  $E_g$ , which is modest for semiconductors and making the the transitions discussed here possible. If the CB minimum is located directly above the VB maximum, the band gap is considered direct, otherwise it is indirect. GaAs is a direct band gap material.

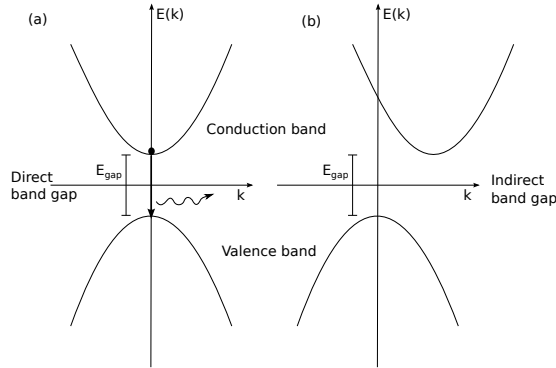


**Figure 2.12:** The dispersion relation for a direct and indirect band gap.

The absorption and emission of light is described by the time dependent perturbation theory in quantum mechanics. The total probability for a transition between energy states per unit time is described by Fermi's Golden Rule [31]

$$w_{i \rightarrow f} = \frac{2\pi}{\hbar} |V_{if}|^2 \rho(E_f) \quad (2.25)$$

where  $i$  and  $f$  stands for the initial and final states, respectively.  $V_{if}$  is the perturbation,  $\rho(E_f)$  is the density of states and  $E_f = E_i + \hbar\omega$  is the energy of the final state.  $E_i$  is the energy of the initial state, and  $\hbar\omega$  is the photon energy.

There are many types of possible recombination processes in a semiconductor, and some of them are illustrated in fig. 2.13. Recombination of a free electron in the CB with a free hole in the VB is a band-to-band transition. If the recombination energy is greater than  $E_g$ , the recombination is said to be due to hot carriers, which have not relaxed to the bottom of the CB and/or the top of the VB. Impurities in the crystal give rise to donor and acceptor levels that can be a part of a sub-band recombination process. There are two possible free-to-bound transitions: An electron bound to a donor impurity recombine with a free hole in the VB, or a hole bound to an acceptor impurity recombine with a free electron in the CB. Donor to acceptor transitions are also possible, but dependent on the distance between the impurities. Indirect transitions can also occur, and involves both radiative (photon) and non-radiative (phonon) transitions. Recombination via deep level are normally non-radiative and thus less interesting for PL characterization.

The last important transition is the one associated with a free exciton. An exciton is a quasi particle arising from a Coulomb attraction between a hole in the VB and an electron in the CB. This correlated EHP has a hydrogen like state and is loosely coupled in a semiconductor. Excitons can be ionized into a free electron and a hole, and thus have a binding energy  $E_b$  lower than the

gap energy:

$$E_b = E_g - E_t \quad (2.26)$$

where  $E_t$  is the transition energy of the exciton. The excitonic emission gives rise to distinct, narrow emission lines in the spectrum, in contrast to the other types of recombination which have broader lines in the spectra.

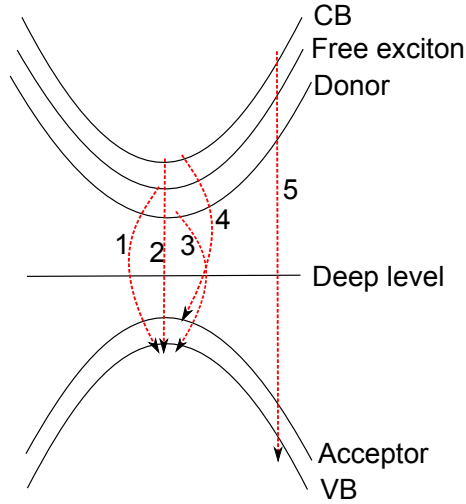


**Figure 2.13:** Some of the possible transitions in a direct band gap. 1: Exciton recombination, 2: Band-to-band, 3: Donor to valence band, 4: Conduction band to acceptor, 5: Hot carrier transition.

Nanostructuring of semiconductors does also have an effect on the optical properties, and must be considered. For GaAs/AlGaAs core-shell NWs, quantum wells might be formed due to the close lattice match between GaAs and AlGaAs. A nanosized layer of GaAs in the AlGaAs shell, for example, can lead to quantum confinement of electrons and is described by the 1D particle-in-a-box problem in quantum mechanics. The allowed energies in a quantum well is given as [31]

$$E_n = \frac{\pi^2 \hbar^2 n^2}{2mL^2} \quad (2.27)$$

which is found solving the Schrödinger equation. Here,  $m$  is the (effective) electron mass,  $n$  is the quantum number and  $L$  is the width of the quantum well. In the spectrum, emission peaks due to quantum confined states are sharp due to the localized energy states.

### 2.3.2 Power dependent PL

An example of a PL setup is shown in fig. 2.14. A laser is directed towards the sample and focused on the desired NW with an objective. The emitted luminescence is directed back through the objective and collected by a spectrometer and recorded by a charged coupled device (CCD) camera. Many types of PL measurements can be made, but in this work power dependent PL was used. This means that the emitted signal is recorded for various excitation powers of the laser, typically ranging between  $0.01 - 100 \mu\text{W}$ . As the lowest available energy states will be filled first, one can study how the signal is changing, as the lower states will be saturated and higher energy states will be dominating at higher power. From the emission spectrum, one can get information about the recombination process as well as the type of defects present.

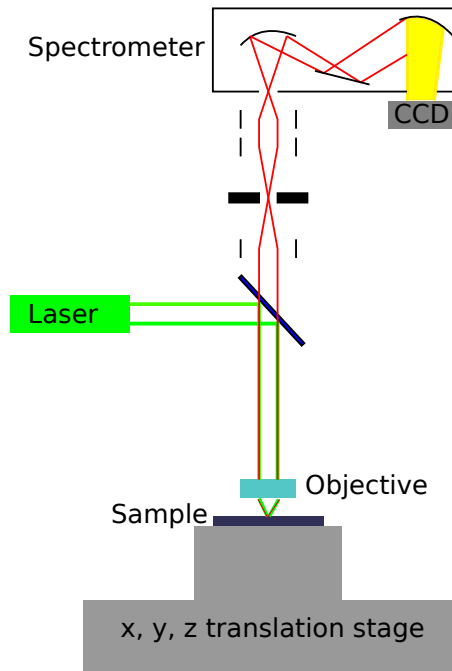


**Figure 2.14:** Schematic of a PL setup. The light from the laser is directed onto the sample where it excites the electrons. The luminescence from the recombination process is collected by a spectrometer and recorded by a CCD camera.

## 2.4 Nanowire growth

The NWs in this work have been grown using molecular beam epitaxy (MBE) through the vapor-liquid-solid (VLS) growth mechanism. The VLS theory is based on [32], while the description of MBE is based on [33] unless otherwise stated.

The VLS mechanism is illustrated in fig. 2.15. First, catalyst droplets are formed on the substrate, which is done by heating the desired catalyst material. For NWs, this material is commonly gold, but as mentioned in the introduction, self catalyzed (SC) NWs are becoming more common. SC means that the catalyst material is also a growth material, for example using Ga as a catalyst to grow GaAs NWs, which is the case in this work. This takes away the risk of Au-deep levels in the material, which will affect the optical properties negatively. The SC technique also gives better control of, and more a homogeneous, catalyst droplet size. To start the growth, a vapor flux of the growth material is directed towards the substrate. The liquid phase is the preferred deposition for the vapor [34], and when supersaturation is reached, nuclei will form and precipitate in the catalyst-substrate interface. Further growth will happen in the catalyst-NW interface, which in turn will make the catalyst droplet grow away from the surface. The growth stops when the catalyst droplet is solidified. For SC NWs, the droplet can be consumed before solidification, as the catalyst material can be incorporated into the NW if the flux of that material is stopped. The diameter of the NW is dependent on the droplet size and can therefore to a certain extent be tuned to the desired thickness. However, the cross section of the NW tend to be larger than the initial droplet size due to the alloying process [35]. There will also be unintentional vapor-solid (VS) growth directly on the NW facets, affecting the final thickness. The composition of the NW is controlled by the composition of the vapor phase, which makes it possible to grow multi-layered or doped NWs.

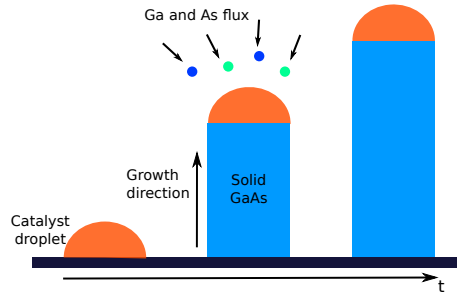


**Figure 2.15:** The growth process of a NW with the VLS mechanism. At elevated temperature the catalyst will form droplets on the substrate. A flux of atoms directed towards the surface will alloy the catalyst, and when the supersaturation is reached, nuclei will precipitate in the interface between the substrate and the droplet. Further growth will happen in the droplet-NW interface, and the droplet will grow away from the substrate. The growth stops when the temperature is lowered and the catalyst droplet is solidified.

The VLS technique is utilized when growing NWs in the MBE, which is one of the main methods for growing NWs. A schematic of the MBE growth chamber is seen in fig. 2.16, where the deposition takes place under ultra high vacuum and elevated temperatures. The substrate is placed on a rotating holder and heated from underneath. The effusion cells contain the material to be deposited. The material is evaporated with heating coils, and when the shutter of a cell is opened into the reaction chamber, a gas flux of the material will be directed towards the substrate. The high vacuum gives a large mean free path so that the atoms do not collide before they reach the substrate surface. Advantages of the MBE include epitaxial growth, fine control of the deposited material and in-situ measurements of the crystal structure of the deposited material by the RHEED system. The growth is terminated when the emission cells are closed and gas flux stopped, except for residual atoms that can still precipitate. In addition to the size of the catalyst droplet, parameters affecting the final structure of the NWs are temperature and gas flux in the MBE.

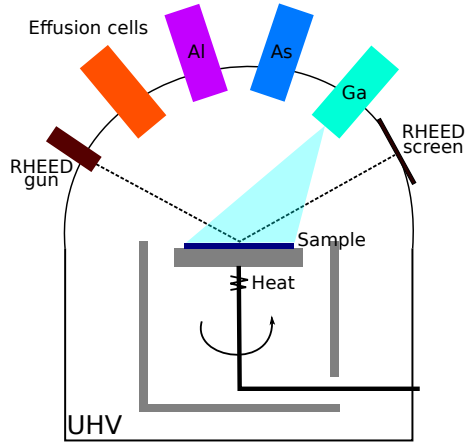


**Figure 2.16:** Schematic of the growth chamber in a MBE. The chamber is kept at ultra high vacuum, and the sample is placed on a rotating holder and heated from underneath. The growth species are kept in effusion cells which are heated to create the vapor, and the growth is started when the shutter of the cell is opened and a flux of atoms is directed towards the sample surface. The growth can be monitored in-situ using a RHEED system.

## 2.5 Nanowire crystal structure and morphology

GaAs NW can take two different crystal phases; ZB and WZ. What structure is formed depends on the growth conditions and what catalyst is used. When using a gold catalyst, the WZ phase is dominating, while most of the NW will be ZB structure if the SC technique is used [36]. This is due to a much lower surface energy in liquid Ga than in Ga-Au alloys [37]. The ZB phase is also the preferred phase for bulk GaAs [38].

The structure factor for WZ and ZB can be calculated by inserting the coordinates for the atoms in the unit cell in (2.14), which can be used to determine their extinction rules, i.e. what reflections in the reciprocal lattice are kinematically forbidden. The atom coordinates in the ZB structure are

$$(x, y, z)_{Ga}^{ZB} = (0, 0, 0), \left(\frac{1}{2}, \frac{1}{2}, 0\right), \left(\frac{1}{2}, 0, \frac{1}{2}\right), \left(0, \frac{1}{2}, \frac{1}{2}\right) \quad (2.28)$$

for Ga and

$$(x, y, z)_{As}^{ZB} = \left(\frac{1}{4}, \frac{1}{4}, \frac{1}{4}\right), \left(\frac{3}{4}, \frac{3}{4}, \frac{1}{4}\right), \left(\frac{3}{4}, \frac{1}{4}, \frac{3}{4}\right), \left(\frac{1}{4}, \frac{3}{4}, \frac{3}{4}\right) \quad (2.29)$$

for As. When substituting these values in the expression for the structure factor, (2.14) becomes

$$F_{ZB} = (f_{Ga} + f_{As} e^{\frac{i\pi}{2}(h+k+l)}) \{1 + e^{i\pi(h+k)} + e^{i\pi(h+l)} + e^{i\pi(k+l)}\}, \quad (2.30)$$

where  $f_{Ga}$  and  $f_{As}$  are the atomic form factors for the two different atoms. This gives the following extinction rules:

- $F_{ZB} = 0$  if  $h, k, l$  mixed,
- $F_{ZB} = 4(f_{Ga} \pm i f_{As})$  if  $h, k, l$  all odd,
- $F_{ZB} = 4(f_{Ga} - f_{As})$  if  $h, k, l$  all even and  $h + k + l = 2N$  where  $N$  is odd,
- $F_{ZB} = 4(f_{Ga} + f_{As})$  if  $h, k, l$  all even and  $h + k + l = 2N$  where  $N$  is even.

This means that for example the (100) reflection will not be seen in the DP, while (111) is visible. The (002) reflection will also be visible, but since  $f_{Ga} \approx f_{As}$  the reflection will be weak. The reason why it is often visible in the DP is due to dynamical effects, in this case plural scattering on the {111} planes.

The structure factor for WZ is found the same way. Only two atoms need to be included in the unit cell for the HCP lattice, and since the three-index system is used to derive the structure factor, the atom coordinates are

$$(x, y, z)_{Ga}^{WZ} = \left(\frac{1}{3}, \frac{2}{3}, 0\right), \left(\frac{2}{3}, \frac{1}{3}, \frac{1}{2}\right) \quad (2.31)$$

for the Ga atoms, and

$$(x, y, z)_{As}^{WZ} = \left(\frac{1}{3}, \frac{2}{3}, \frac{3}{8}\right), \left(\frac{2}{3}, \frac{1}{3}, \frac{7}{8}\right) \quad (2.32)$$

for the As atoms. The structure factor is then

$$F_{WZ} = f_{Ga} [e^{i2\pi(\frac{1}{3}h + \frac{2}{3}k)} + e^{i2\pi(\frac{2}{3}h + \frac{1}{3}k + \frac{1}{2})}] + f_{As} [e^{i2\pi(\frac{1}{3}h + \frac{2}{3}k + \frac{3}{8})} + e^{i2\pi(\frac{2}{3}h + \frac{1}{3}k + \frac{7}{8})}], \quad (2.33)$$

which gives the following extinction rules (using three indices):

- $F_{WZ} = 0$  if  $l$  is odd and  $h - 2k = 3m$ ,
- $F_{WZ} = \sqrt{3}(f_{Ga} + f_{As})$  if  $l$  is odd and  $h - k \neq 3m$ ,
- $F_{WZ} = \pm 2\sqrt{f_{Ga}^2 + f_{As}^2}$  if  $l = 4m + 2$  and  $h - 2k = 3m$ ,

- $F_{WZ} = \pm\sqrt{f_{Ga}^2 + f_{As}^2}$  if  $l = 4m + 2$  and  $h - k \neq 3m$ ,
- $F_{WZ} = 2(f_{Ga} + f_{As})$  if  $l = 4m$  and  $h - k = 3m$ ,
- $F_{WZ} = f_{Ga} + f_{As}$  if  $l = 4m$  and  $h - k \neq 3m$ .

Accordingly, for WZ the (0001) reflection will be kinematically forbidden, while (0002) will be visible. The third index is found by using  $i = -(h+k)$  as defined in section 2.1.1. However, some forbidden reflections are visible due to dynamic scattering in the specimen. The DP for ZB and WZ can be seen in fig. 2.17 (a) and (b), respectively. As these are real DPs, reflections do to dynamical effects can be seen, e.g. the (0001) reflection in fig. 2.17 (b).

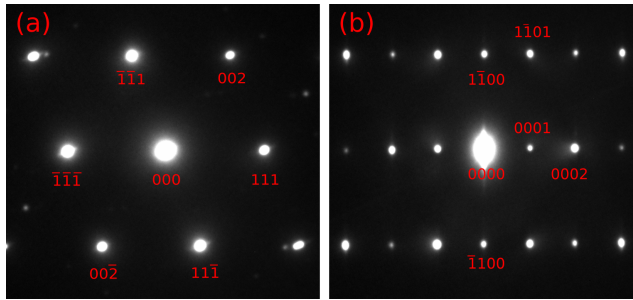


**Figure 2.17:** DPs for the GaAs crystal phases (a) ZB on the  $[1\bar{1}0]$  zone axis and (b) WZ on the  $[11\bar{2}0]$  zone axis. Some of the kinematically forbidden/weak reflections are visible in the DP such as (002) for ZB and (0001) for WZ.

The NWs in this work has an  $\text{Al}_x\text{Ga}_{x-1}\text{As}$  shell as well as an  $\text{Al}_x\text{Ga}_{x-1}\text{As}$  insert, where  $0 < x < 1$  is the alloying content of Al in the GaAs structure. As the lattice constant for AlGaAs is very similar to that of GaAs, the two materials have very similar crystal structural properties [39]. However, as  $Z_{Al} > Z_{Ga}$ , the structure factor will be different as  $f_{Al} > f_{Ga}$ . In the DP, some reflections will be very bright, e.g. the (002) reflection, instead of weak as is the case for GaAs. Thus, DF images recorded when using the (002) reflection will have a higher contrast, indicating the presence of AlGaAs.

GaAs NWs grown in the  $[111]$  direction for ZB and  $[0001]$  direction for WZ on a Si substrate has a hexagonal shape as these axis have a threefold symmetry [40]. ZB grows in either the  $[111_A]$  or  $[111_B]$  direction, as illustrated in fig. 2.18. *A* and *B* refers to the two possible twinning directions in ZB. As the growth rate in the  $[111_A]$  direction is low, the growth is nearly always in the  $[111_B]$  direction. The faceting of the NWs is also illustrated in the figure. By VS growth, a shell can be grown on the facets. As all facets are of the same direction, the shell growth will be similar on all facets.

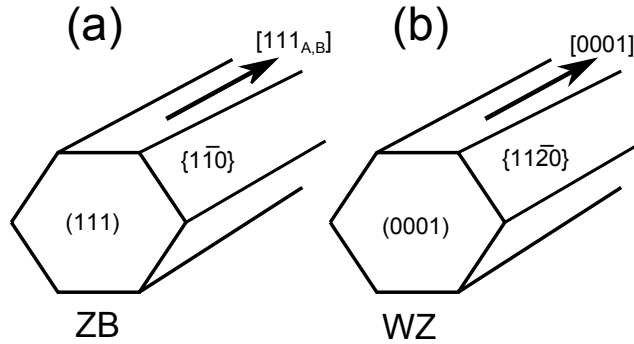


**Figure 2.18:** Faceting and growth direction for (a) ZB and (b) WZ GaAs NWs.

As the NWs has a core-shell structure, the intensity profiles from HAADF STEM and element profiles from EDS will have a different shape than if the the NWs were core-only. This is because when scanning a core-shell structure, two parameters (thickness and mass) will be changing simultaneously, while in a core-only NW, only the thickness will vary. Also, the profiles will be different depending on what zone axis the NW is on. This is illustrated in fig. 2.19. The  $[110]$  zone axis is the most common, while one gets the  $[112]$  zone axis by tilting the NW by  $30^\circ$ . As HAADF STEM is both thickness and mass sensitive, the intensity profile will be change both with the thickness of the NW and how much of each element is present. The EDS element profile also gets a characteristic shape for the group III elements Al and Ga due to the thickness variations and that Al has a higher atomic number, which is illustrated in the figure.

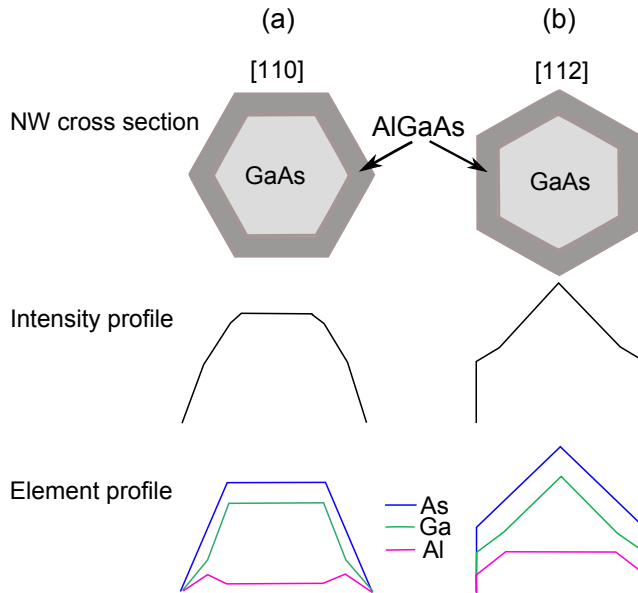


**Figure 2.19:** The shape of the intensity and EDS profiles for two different orientations of the NW; (a)  $[110]$  and (b)  $[112]$ .

# Chapter 3

## Experimental

### 3.1 Nanowire growth

The NWs studied in this work were grown through a VLS mechanism using a Varian Gen II Modular MBE system under ultrahigh vacuum ( $1 \times 10^{-10}$  Torr). The SC technique was used for all the NWs, and the growth was initiated by opening the As and Ga shutters in the MBE simultaneously. For the purpose of this report, the samples have been given logical names; their corresponding internal names can be seen in table 3.1.

**Table 3.1:** *The internal names of the samples together with the names used in this report.*

Internal name	Report name
SC 276	Random1
SC 277	Random2
SC 278	Random3
SC 335	BareCore
SC 343	Main

#### 3.1.1 Sample Main

The NWs on sample Main were grown position controlled on a p-doped Si(111) substrate. To achieve this, the substrate was covered with a  $\sim 40$  nm thick SiO<sub>2</sub> mask, where the array pattern was created using NIL and subsequent wet etching. The Si NIL stamp used had circular bumps of diameter 75 nm and 100 nm height, 1  $\mu$ m apart in a hexagonal pattern. After etching the transferred holes in the SiO<sub>2</sub> mask was about 100 nm wide [21].

The Si substrate with the NIL patterned SiO<sub>2</sub> mask was subsequently used in the MBE for NW growth. The Ga catalyst droplet will only form where

the underlying Si substrate is exposed. The growth conditions for the NWs are listed in table 3.2. The core is pure GaAs, with an  $\text{Al}_{0.33}\text{Ga}_{0.67}\text{As}$  axial segment in the tip, grown before droplet solidification. The AlGaAs shell and GaAs cap layer was grown at the same temperature, but done after solidification to limit further axial growth.

**Table 3.2:** Growth parameters for the core, shell and cap layer for the self catalyzed core-shell GaAs NWs on sample Main with an axial AlGaAs segment before droplet solidification. The droplet was solidified during 10 min with an  $\text{As}_2$  flux of  $1 \times 10^{-5}$  mbar. ML/s = monolayers per second.

Part of NW	Ga flux [ML/s]	$\text{As}_2$ flux [mbar]	Al flux [ML/s]	Time [min]	Temp. [°C]
GaAs core	0.6	$5.5 \times 10^{-6}$	-	25	630
Axial AlGaAs	0.3	$5.5 \times 10^{-6}$	0.15	5	630
AlGaAs shell	0.3	$1 \times 10^{-5}$	0.15	20	630
GaAs cap	0.3	$1 \times 10^{-5}$	-	8	630

### 3.1.2 Sample BareCore

As a reference sample to the core-shell NWs on sample Main, core-only NWs with approximately the same growth conditions and position controlled growth were studied. In this way, the effect of shell growth and droplet consumption could be better understood for the NIL sample. The substrate was first annealed for 5 min at 690°C before the Ga catalyst droplet was created by a 50 s long predeposition time. The growth parameters for the sample are listed in table 3.3. The droplet was not consumed before the growth was stopped.

**Table 3.3:** Growth conditions for the core only NWs on sample BareCore.

Part of NW	Ga flux [ML/s]	$\text{As}_2$ flux [mbar]	Al flux [ML/s]	Time [min]	Temp. [°C]
GaAs core	0.6	$5.0 \times 10^{-6}$	-	10	630

### 3.1.3 Random1, Random2 and Random3

As reference to the position controlled grown samples, three random grown samples were studied as well; Random1, Random2 and Random3. The NWs on the three samples were all grown on a fresh native oxide p-doped Si(111) substrate 5° off axis. The difference between the three samples is the V/III ratio, which was achieved by changing the As-flux in the MBE. To get similar length of the NWs on the three samples, the growth time was decreased when the flux was increased. After core growth, the Ga catalyst was consumed before the shell could be grown to limit further axial growth. The consumption was

done by stopping the Ga-flux, lowering the temperature to 460°C and setting the As flux to  $1.3 \times 10^{-5}$  mbar for 10 min. The growth conditions for the GaAs core,  $\text{Al}_{0.33}\text{Ga}_{0.67}\text{As}$  shell and GaAs cap layer for the three samples are listed in table 3.4.

**Table 3.4:** Growth parameters for the core, shell and cap layer for the self catalyzed core-shell GaAs NWs on Random1, Random2 and Random3. The shell and cap layer growth conditions are the same for all three samples.

Sample	Ga flux [ML/s]	As <sub>4</sub> flux [mbar]	Al flux [ML/s]	Time [min]	Temp. [°C]
Random1 core	0.7	$5.5 \times 10^{-6}$	-	30	640
Random2 core	0.7	$7.5 \times 10^{-6}$	-	25	640
Random3 core	0.7	$9.5 \times 10^{-6}$	-	20	640
Shell	0.2	$1.8 \times 10^{-5}$	0.1	30	460
Cap	0.2	$1.8 \times 10^{-5}$	-	20	460

## 3.2 Specimen preparation

Four silicon nitride (SiN) PL-TEM specimens were prepared, one for each growth batch to be measured using PL (Main, Random1, Random2 and Random3). The specimen has nine frames that are 100  $\mu\text{m}$  wide and covered by a 50 nm thick SiN film. The NWs were harvested from the sample by scraping them off the substrate with a fine (60  $\mu\text{m}$ ) scraper in roughly the [112] direction, and dispersing them in a droplet of isopropanol placed on top of the sample using a pipette. The SiN specimen was placed upside down on the droplet to transfer some of the NWs from the dispersion to the specimen, before it was left to dry. An example of a frame on this specimen can be seen in fig. 3.1 (a).

As the SiN film is very fragile and relatively thick, which affects the (S)TEM imaging, Cu/graphene TEM specimens were prepared as well from the Main sample. The specimens are made out of two TEM grids glued on top of each other using Ag paste. The bottom one is a 2000 mesh Cu grid with a window size of  $7.5 \times 7.5 \mu\text{m}$ , covered with a graphene thin film. On top is a numbered Cu grid with window size  $100 \times 100 \mu\text{m}$ , making tracking of the NWs possible. The NWs are transferred to this specimen using the same method as for the SiN specimen. The Cu/graphene specimen was used for correlated S(T)EM and TEM characterization, and can be seen in fig. 3.1 (b). The NW position mapping of both the SiN and the Cu/graphene specimens was done using a TM3000 tabletop SEM at 15 kV. The SEM uses BS electrons for imaging.

A regular holey carbon covered, 300 mesh, Cu grid TEM specimen was made for sample Main as well as for the BareCore sample. For the Main sample, this was mainly for HRTEM, HAADF STEM and EDS purposes.

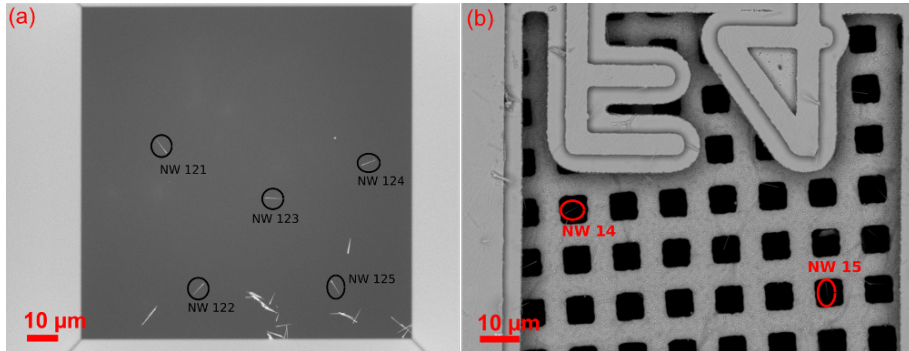


**Figure 3.1:** The images show NW mapping using a TM3000 tabletop SEM of (a) a SiN and (b) a graphene specimen. The SiN specimen has nine windows one can navigate between, while the graphene specimen has a numbered Cu grid on top to enable tracking of NWs in PL, TEM and  $S(T)EM$  experiments.

### 3.3 Optical characterization

Sample Main as well as Random1, Random2 and Random3 (all SiN PL-TEM specimens) were optically characterized using PL. This was done before the structural characterization as the 200 kV electron beam in a TEM induces point defects in the NWs making them optically inactive [20].

The laser beam used in the experiment to excite the NWs on the sample was created by a 532 nm wavelength laser diode. Part of the laser light was reflected towards the sample with a beam splitter cube, while a lens focused the light onto single NWs. The emitted PL signal from the NWs was transmitted back through the splitter cube and a filter before it entered an Andor Shamrock spectrometer. An Andor Newton Si CCD camera was used to detect the signal, which is a Thermo-Electrically cooled EMCCD, Andor iDus InGaAs detector array. LABview software was used to operate the camera, while Andor SOLIS was used for the spectroscopy. A cryostat of the type Cryo Industries RC102-CFM Microscopy was used to keep a continuous flow of liquid Helium-4 (4.2 K) to keep the temperature at 12 K during experiments.

### 3.4 Structural characterization

For this work, a Jeol JEM-2100 with a LaB<sub>6</sub> source at 200 kV was used to make the BF and DF TEM images. The images were captured using a Gatan 2k Orius<sup>TM</sup> CCD camera, and the TEM software used was Gatan's Digital Micrograph. The HRTEM and HAADF images and the EDS spectra was obtained using a Jeol JEM-2100F microscope with a 200 kV Schottky field

emission gun. A Gatan 2k UltraScan CCD camera (bottom mounted) was used to capture the HRTEM images, using Gatan's Digital Micrograph software. The X-ray detector used on the JEM-2100F is an Oxford X-Max 80 SDD EDX operated with the Aztec software. The EDX line profiles were recorded with a 1 nm probe in analytical TEM mode and a condenser lens aperture of 50  $\mu\text{m}$ .

For the BF STEM and SEM characterization of the NWs, a Hitachi S-5500 S(T)EM was used. The S(T)EM uses a cold cathode field emission gun electron source and an in lens system. When characterizing the as-grown samples as well as the NW facets, the SEM was operated at 10 kV using secondary electrons for imaging. When doing BF STEM the microscope was operated at 30 kV.

### 3.5 Data processing

The TEM images have been processed in ImageJ, including doing FFT and measuring the dimensions of the NW. Inkscape and GIMP have been used to make the images presentable for this text. The PL data as well as the intensity profiles from HAADF STEM and the EDS line scans were plotted using Python. The PL data have been scaled so that the highest intensity for all plots is set to one, and each plot is shifted to facilitate easier reading.

# Chapter 4

## Results

In this chapter, the characterization of the five samples is presented. First, TEM, S(T)EM, HAADF STEM and EDS characterization of the structure and morphology is given, before the results of the optical measurements in PL will be presented in the last section. The characterization of the three random grown samples (Random1, Random2 and Random3) is shown first, followed by an overview of positioned versus random grown NWs as seen in SEM before they are broken off the substrate. The core-only (BareCore) and core-shell (Main) NIL samples are presented lastly.

### 4.1 Structural characterization of random grown samples

The three random grown samples that previously have been characterized on a graphene PL-TEM specimen, were re-characterized on a SiN specimen. This was because SiN is better suited for PL studies as graphene might contribute to the signal,. SiN therefore gives a more accurate characterization. The SiN specimen is also easier to handle in TEM as the NWs are less bended due to a flat surface. However, HRTEM is very difficult because the NWs lie on a 50 nm thick substrate. The SiN specimen is also very fragile and cracks easily.

#### 4.1.1 Sample Random1

On sample Random1, 13 NWs were characterized in TEM, where all of them showed very similar structural properties. The average size of the WZ segment was found to be 160 nm, while the mixed phase segment was 180 nm on average. This is also very similar to the average NW on the equivalent graphene specimen. NW 225 was chosen as a representative NW, and is presented in fig. 4.1. Both the WZ segment and the mixed phase is 160 nm long. One of

the NWs characterized also had the bottom intact, where short segments of WZ was present in a mixed phase region (not shown). The NWs on Random1 generally had a low twin density compared to the NWs on samples Random2 and Random3.

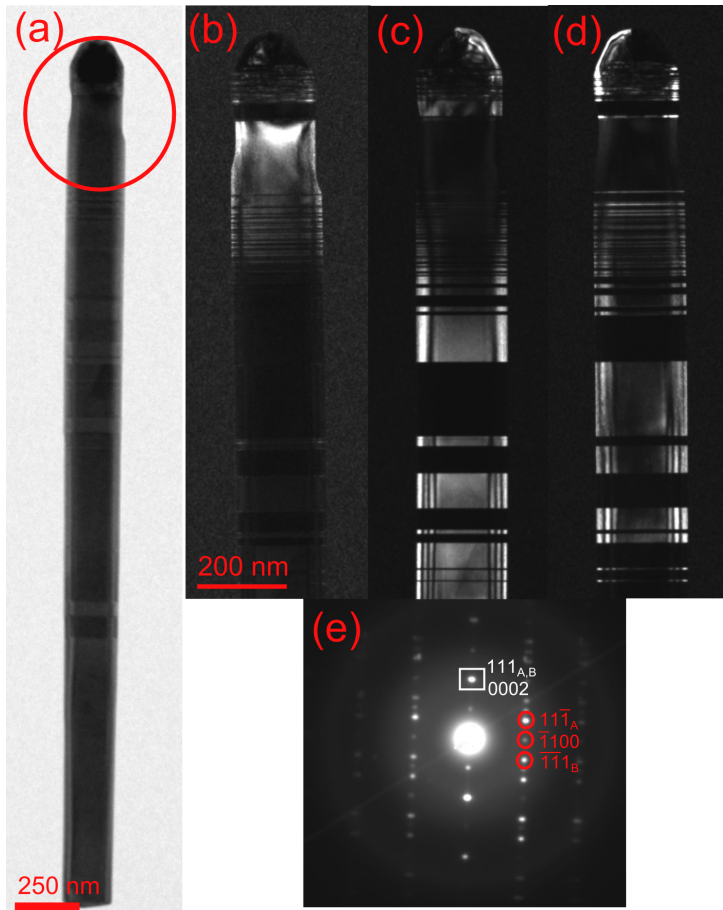


**Figure 4.1:** TEM characterization of NW 225 on sample Random1. (a) BF image of the NW. (b), (c) and (d): DF images of the NW taken using the following reflections: (b)  $\bar{1}100$  (WZ), (c)  $\bar{1}\bar{1}1_B$  ( $ZB_B$ ), (d)  $11\bar{1}_A$  ( $ZB_A$ ). (e) DP of the tip of the NW.

#### 4.1.2 Sample Random2

On sample Random2, nine NWs were characterized in TEM. All the NWs had a WZ segment, with the average size being 140 nm, which is the same as the

average size on the graphene specimen. Two NWs had a longer WZ segment (590 and 450 nm), and is not included in the average. The average size of the mixed phase segment was found to be 400 nm, but with large variations; the smallest being 50 nm, and the largest about 930 nm. NW 311 shown in fig. 4.2 was chosen as a representative NW, even though the length of the WZ segment, being only 50 nm, is shorter than the average, and a mixed phase segment of 580 nm is larger than the average. The NW still shows what is important to note: A very high SF and twin density in the tip area and also further down on the NW.

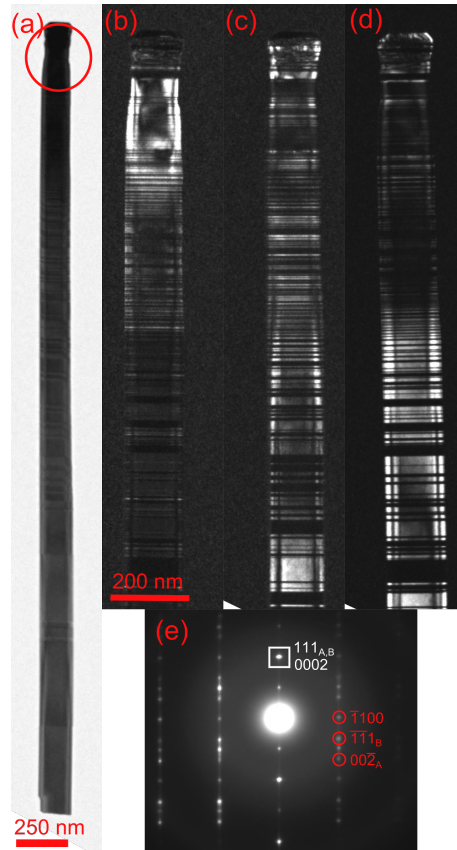


**Figure 4.2:** TEM characterization of NW 311 on sample Random2. (a) BF image of the NW. The red circle indicates where the DP is taken. (b), (c) and (d): DF images of the NW taken using the following reflections: (b)  $\bar{1}100$  (WZ), (c)  $00\bar{2}_A$  ( $ZB_A$ ), (d)  $\bar{1}\bar{1}1_B$  ( $ZB_B$ ). (e) DP of the tip of the NW.

### 4.1.3 Sample Random3

Of the 23 NWs on sample Random3 on SiN that was characterized with PL, only five were possible to characterize in TEM. The specimen was covered with dirt and oil, which made the characterization very difficult. Two attempts to plasma clean the samples were made, the results of which were somewhat successful. Additionally, many of the windows on the specimen were cracked.

Of the five NWs characterized, two of them contained no WZ segment. The other three contained WZ, but with varying size of the segments. On the graphene specimens studied earlier, no NWs were found to lack a WZ region. NW 126 in fig. 4.3 illustrates these two NWs.

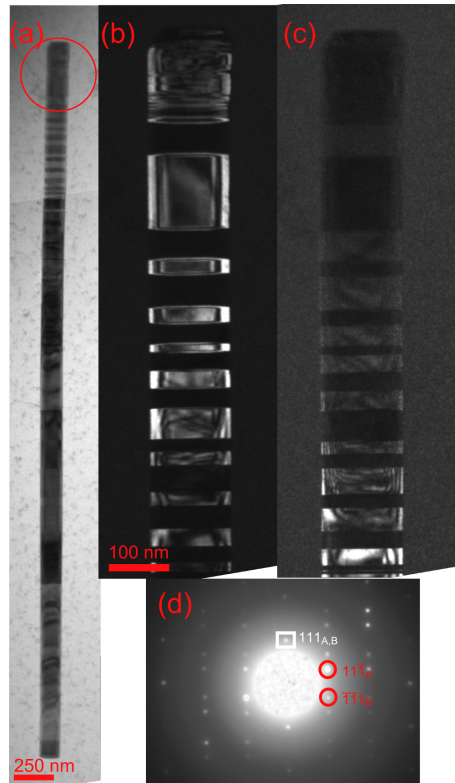


**Figure 4.3:** TEM characterization of NW 126 on Random3. (a) BF image of the NW. The red circle indicates where the DP is taken. (b) and (c) DF images of the NW, taken using the  $11\bar{1}_A$  ( $ZB_A$ ) and  $\bar{1}11_B$  ( $ZB_B$ ) reflections, respectively. (d) DP of the tip of the NW.

The DF images in fig. 4.3 (c) and (d) are made using the reflections from the two different orientations of ZB. The images have complementary dark and

bright areas, indicating that there is no WZ present. The SADP of the tip in fig. 4.3 (d) does not show any WZ reflections, further confirming the finding. It is interesting to notice the shape of the tip, which is considerably different than what has been observed previously on NWs containing WZ. The consumed catalyst droplet has approximately the same diameter as the rest of the NW, and there is no tapering below the droplet as observed when WZ is present.

NW 127 had a short WZ segment, followed by a long mixed phase segment, making it similar to the representative NW on sample Random2 and about half of the NWs on Random3 characterized on graphene. The NW is shown in fig. 4.4.

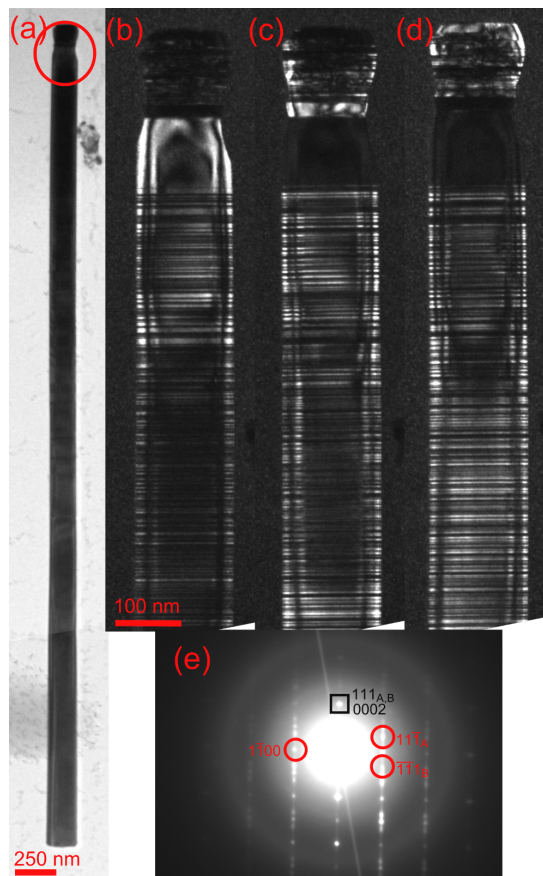


**Figure 4.4:** TEM characterization of NW 127 on sample Random3. (a) BF image of the NW. The red circle indicates where the DP is taken. (b), (c) and (d): DF images of the NW taken using the following reflections: (b)  $0003$  (WZ), (c)  $11\bar{1}_A$  ( $ZB_A$ ), (d)  $\bar{1}\bar{1}1_B$  ( $ZB_B$ ). (e) DP of the tip of the NW.

The WZ segment is measured to be 105 nm long, while the mixed phase segment is more than 700 nm long. This is consistent with the average sizes measured on graphene. NW 134 shown in fig. 4.5 represents the two NWs with a long WZ segment. For this NW, the WZ segment was measured to be 440 nm long, while the mixed phase segment is about 380 nm long. As for NW 126, this is also consistent with the findings on graphene.

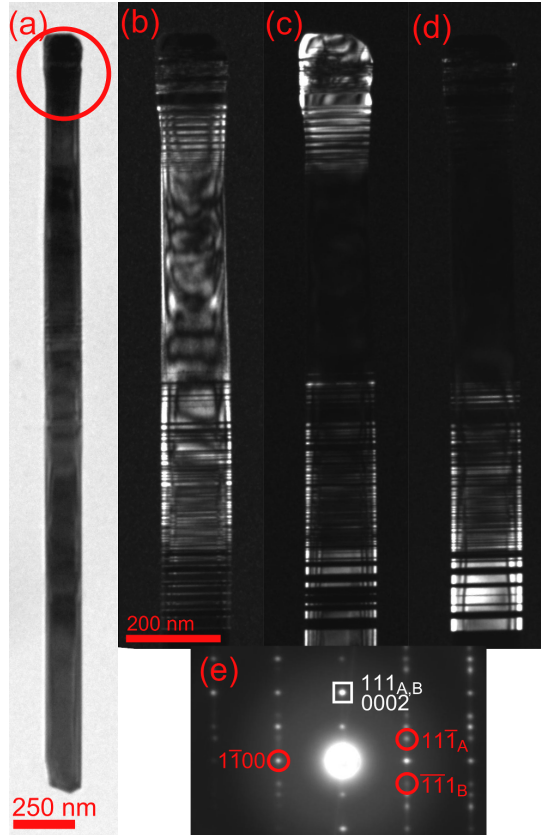


**Figure 4.5:** TEM characterization of NW 134 on sample Random3. (a) BF image of the NW. (b), (c) and (d): DF images of the NW taken using the following reflections: (b)  $000\bar{3}$  (WZ), (c)  $11\bar{1}_A$  ( $ZB_A$ ), (d)  $1\bar{1}1_B$  ( $ZB_B$ ). (e) DP of the tip of the NW.

## 4.2 Positioned NW growth

SEM was used to study the as-grown samples Random3, BareCore and Main. The difference between random and positioned growth can be seen in fig. 4.6,

where (a) and (b) are images of Random3, (c) and (d) are from sample BareCore and (e) and (f) are taken from sample Main.

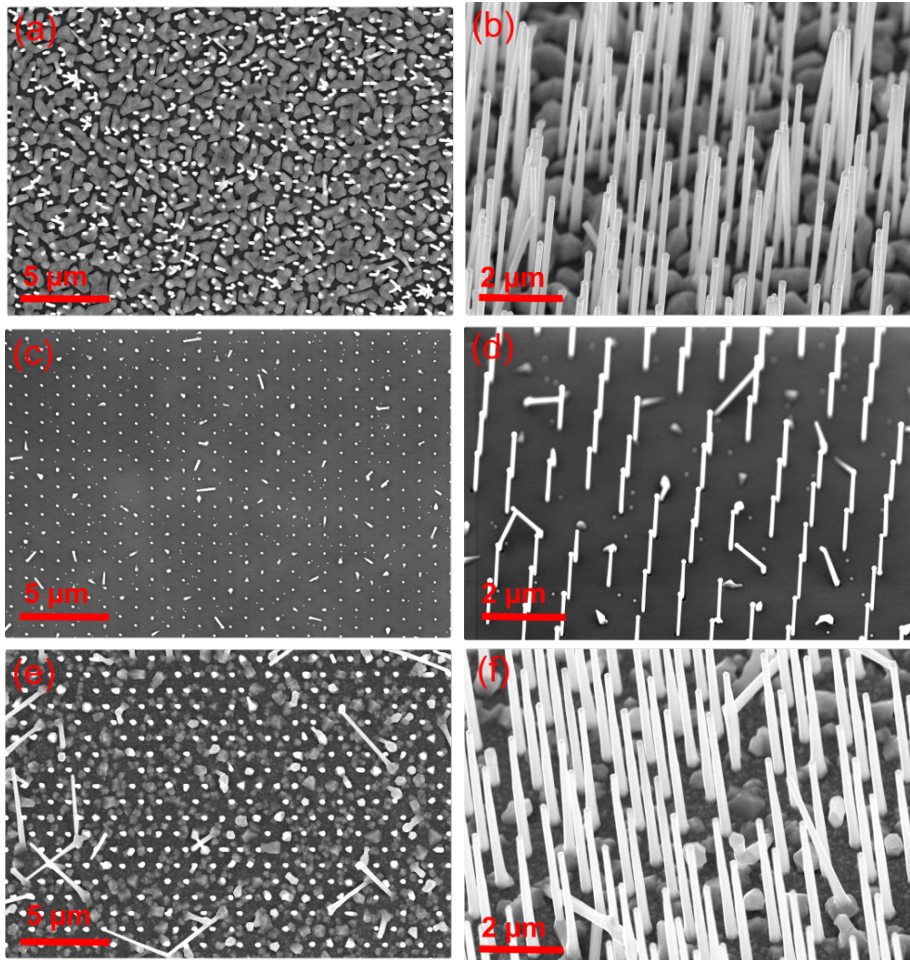


**Figure 4.6:** SEM images illustrating the difference between NIL and random grown samples. (a) and (b): Sample Random1. (c) and (d): Sample BareCore. (e) and (f): Sample Main. The samples Main and Random1 are imaged after the TEM specimens have been prepared, and therefore show a non-clean substrate surface and broken off NWs.

As can be seen from the images, Random3 displays completely random positions for the NW, while the other two samples show a structured growth position. It is about  $1 \mu\text{m}$  between the NWs on these two samples, and al-

most all positions in the pattern has a NW. The broken off NWs as well as the non-clean substrate in fig. 4.6 (a), (b), (d) and (e) are due to the images being taken after the TEM specimen preparation. The NWs that are not standing up straight in fig. 4.6 (c) and (d) are probably due to the handling of the sample, or that the NWs have not grown straight in the MBE.

## 4.3 Sample BareCore

### 4.3.1 Phases

On sample BareCore, five NWs were characterized in TEM. They were found to be very similar, and a representative NW is presented in fig. 4.7. The length and width of the NW is  $1.9 \mu\text{m}$  and  $70 \text{ nm}$ , respectively.

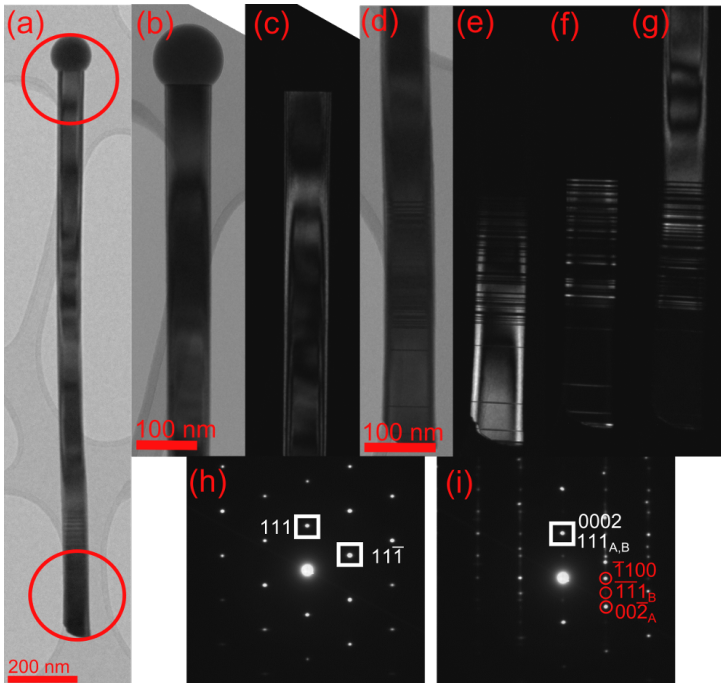


**Figure 4.7:** TEM characterization of a representative NW on sample BareCore. BF images are shown for the tip (b), bottom (d) and entire NW (a). (c) shows a DF image of the tip taken using the  $11\bar{1}$  reflection seen in the DP in (h). (e) - (g) are DF images of the bottom, taken using the (e)  $\bar{1}100$  (WZ), (f)  $\bar{1}11_B$  ( $ZB_B$ ) and (g)  $00\bar{2}_A$  ( $ZB_A$ ) reflections. (h) and (i) are DP of the tip and bottom respectively, taken where indicated by red circles in (a).

As can be seen from the BF image in (a) and (b), the catalyst droplet is not consumed. The tip area does not have any defects, which is opposite to the other NWs in this study which does have a very defect rich region in the tip. These NWs, however, have a different structure in the bottom than previously observed. The NWs on BareCore have a large WZ segment in the bottom, followed by a mixed phase segment, before the phase changes to pure ZB without any twins. For the NW in fig. 4.7, this can be seen in (e) - (g). Here, the WZ segment is 170 nm, while the mixed phase segment is 180 nm, which is close to the average of the NWs measured.

### 4.3.2 Morphology

To determine the morphology of the NWs on sample BareCore, S(T)EM was used. The result for a representative NW can be seen in fig. 4.8.

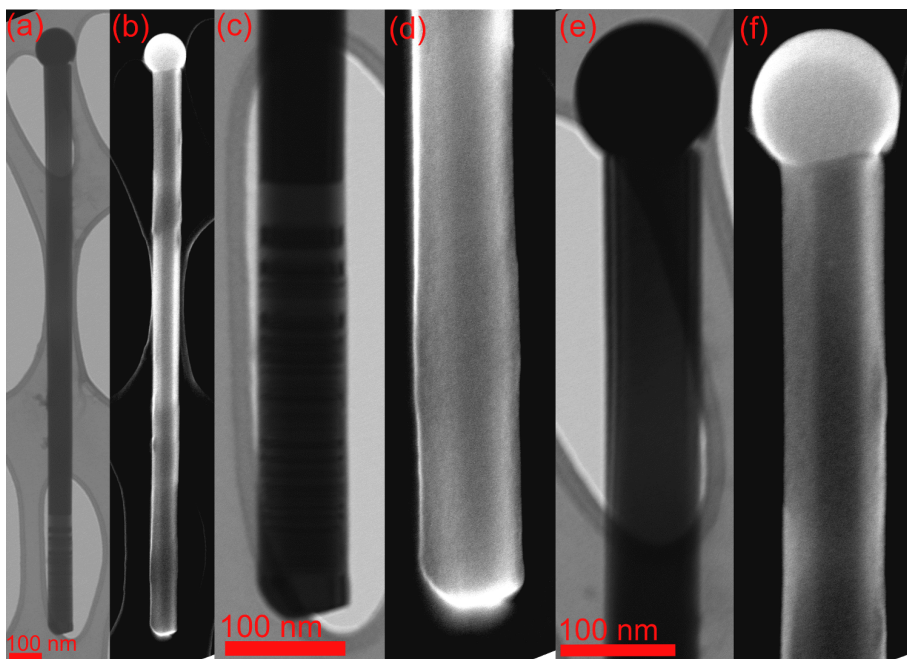


**Figure 4.8:** 30 kV STEM and 10 kV SEM of a representative NW on sample BareCore. (a), (c) and (e) are BF STEM images, while (b), (d) and (f) are SEM images of the entire NW, bottom and tip, respectively.

As expected, the NW has a hexagonal shape with an unconsumed catalyst droplet. There is a slight roughness on the facets, but the thickness is the same throughout the NW. The BF STEM images from the same NW show a defect

free NW, except for the bottom 500 nm, which confirms the findings in TEM.

## 4.4 Sample Main

### 4.4.1 Phases

On sample Main on SiN, 32 NWs were characterized in TEM. A representative NW is presented in fig. 4.9. The NW is 5  $\mu\text{m}$  long, which is close to the average of 5.1  $\mu\text{m}$ , and a difference in thickness is observed between the tip and the bottom.

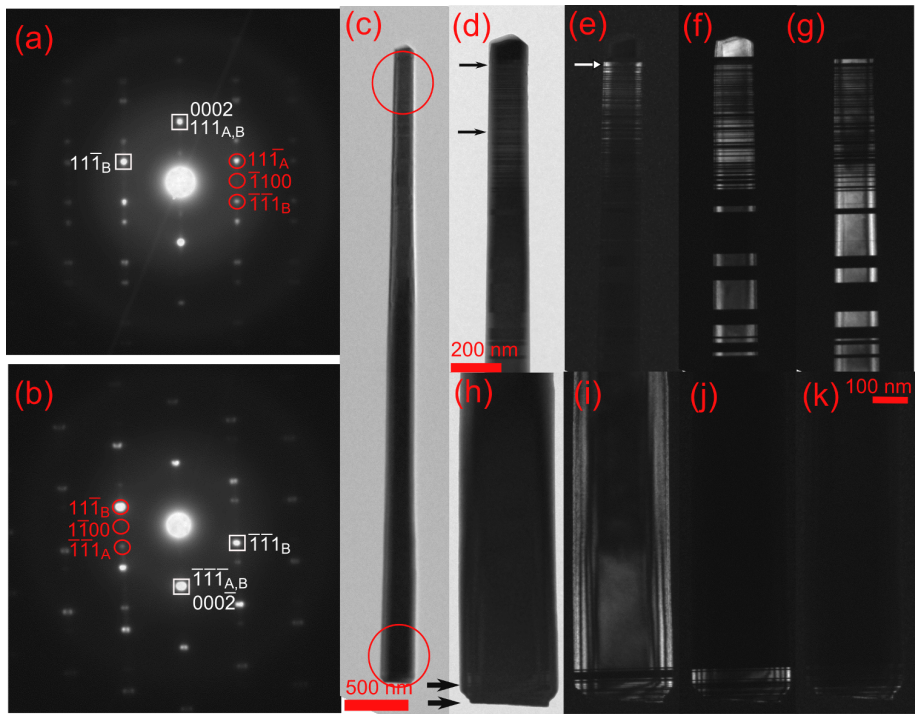


**Figure 4.9:** TEM characterization of NW 212 on sample Main. (a) DP of the tip area of the NW. (b) DP of the bottom area of the NW. (c) BF image of the NW. The red circles indicate where the DPs are created. (d) BF image of the NW tip. The black arrows indicate the mixed phase segment. The DF images of the tip are taken using the (e)  $\bar{1}100$  (WZ), (f)  $11\bar{1}_A$  ( $ZB_A$ ) and (g)  $\bar{1}\bar{1}1_B$  ( $ZB_B$ ) reflections. The white arrow in (e) shows the largest WZ segment. (h) BF image of the bottom of the NW. The black arrows indicate the mixed phase segment. The DF images of the bottom are taken using the (i)  $11\bar{1}_B$  ( $ZB_B$ ), (j)  $\bar{1}\bar{1}1_A$  ( $ZB_A$ ) and (k)  $1\bar{1}00$  (WZ) reflections.

The bottom part of the NW is measured to be 270 nm, while the tip is only 160 nm wide. The decrease in thickness is quite evenly distributed throughout the NW. The DPs of the tip and bottom of the NW can be seen in fig. 4.9 (a) and fig. 4.9 (b), respectively. From the DPs it can be difficult to determine the presence of WZ, but from the DF images, WZ can be detected both in the tip ( $\bar{1}\bar{1}00$  reflection) and in the bottom ( $1\bar{1}00$  reflection) (fig. 4.9 (e) and fig. 4.9 (k)). The largest WZ segment (20 nm) is indicated by a white arrow in fig. 4.9 (e). However, virtually all of the NWs consist of one of the two ZB phases, with an increasing presence of twin planes towards the tip and in the bottom. Figure 4.9 (f) ( $11\bar{1}_A$  reflection) and (g) ( $\bar{1}\bar{1}1_B$  reflection) shows the ZB in the tip, while fig. 4.9 (i) ( $11\bar{1}_B$  reflection) and (j) ( $\bar{1}\bar{1}1_A$  reflection) shows the ZB in the bottom. There are clearly more twins in the tip than in the bottom. The tip does however have a considerable mixed phase segment where both WZ and ZB is present. The segment is about 300 nm long and is indicated by the black arrows in fig. 4.9 (d). The bottom also has a mixed phase segment, but only about 50 nm long.

There are however exceptions to the representative NW, both in defect density, the amount of WZ present, and the shape of the tip and the bottom part. In fig. 4.10 three different NW tips are presented, representing the variety within a batch. Figure 4.10 (a) - (d) shows a NW with a WZ segment of 200 nm, which is considerably longer than the largest WZ segment on the representative NW. Also, the facets of the NW seems to be rough rather than smooth in the same area as the mixed phase segment. Figure 4.10 (e) - (h) shows a NW with a medium long WZ segment, but with no mixed phase region. This is seen as the twinning between the two ZB growth directions in (g) and (h) are not interrupted by any WZ segments before the 90 nm long WZ segment. Figure 4.10 (i) - (l) shows a NW with a small WZ segment (20 nm) like the representative NW in fig. 4.9, but the mixed phase segment of 650 nm is over the double length of the average NW.

The variations between the NWs seen in the bottom are mostly related to the shape. All NWs have a segment with more or less twinning in the bottom, with some elements of WZ segments in between, for the most part in the very bottom part. The structural variations are mostly concerned with the length of the defect segments, and the amount of WZ present. The longest segment was found to be 250 nm long, while some NWs had no defects or mixed phase in the bottom at all. The NWs with the longest mixed phase were also the ones with the most WZ, and had the shape which is seen in fig. 4.13 (b), which will be presented in the next section.

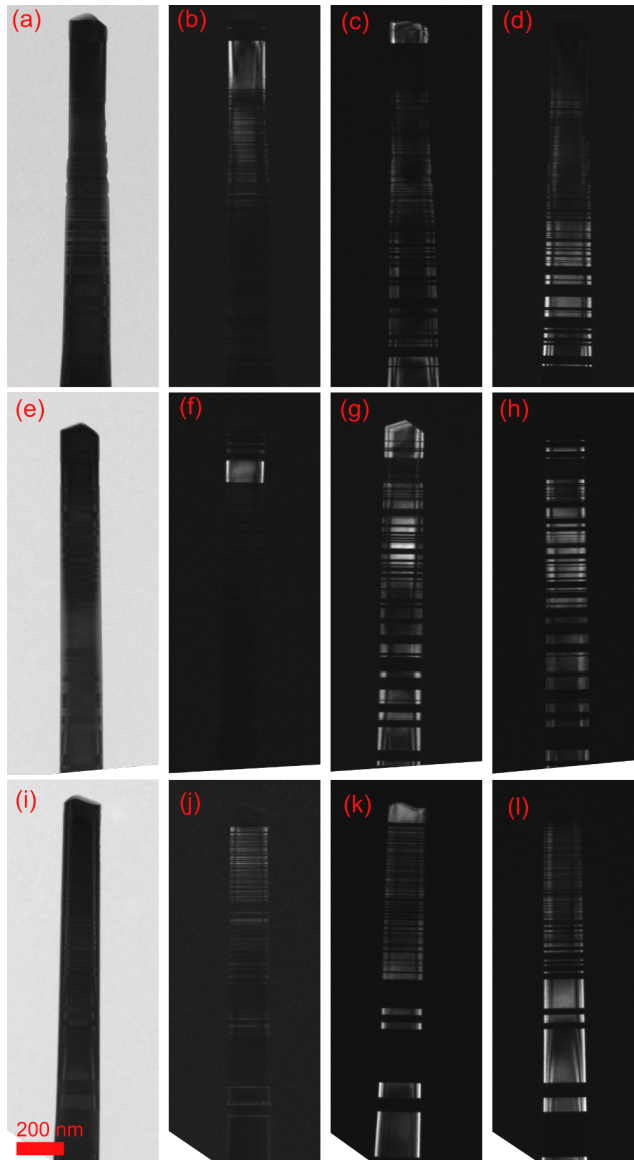


**Figure 4.10:** Overview of the variations seen in the NW tips. (a) - (d): NW with long WZ segment and rough facets. (e) - (h): NW with medium long WZ segment, but with no mixed phase region. (i) - (l): NW with short WZ segment and large mixed phase region, but with straight facets. (a), (e), and (i) are BF images, the others are DF images showing WZ (b, f, j),  $ZB_A$  (c, g, k) and  $ZB_B$  (d, h, l).

### 4.4.2 Morphology

The morphology of the NWs were characterized using 10 kV SEM imaging, and compared with BF/DF TEM and 30 kV BF STEM. The result for a representative NW is seen in fig. 4.11, where the NW is on a graphene support.

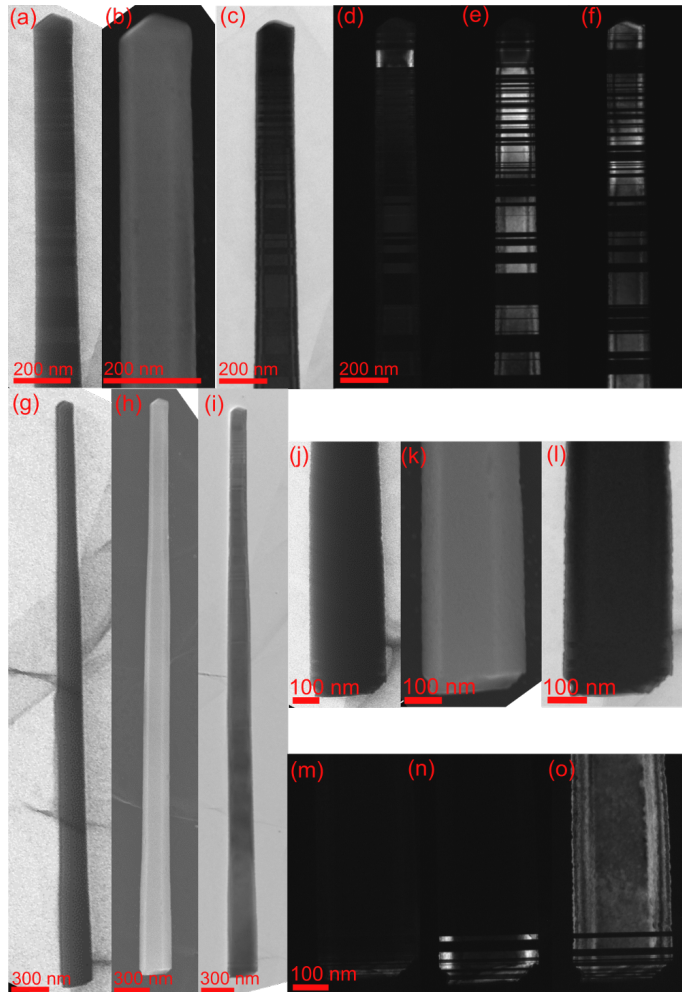


**Figure 4.11:** 10 (30) kV S(T)EM and 200 kV TEM imaging of a representative NW on sample Main. (a) BF STEM, (b) SEM, (c) BF TEM and (d) - (f) DF TEM of the tip of the NW ((d) WZ, (e) ZB<sub>A</sub> and (f) ZB<sub>B</sub>). (g) BF STEM, (h) SEM and (i) BF TEM of the entire NW. (j) BF STEM, (k) SEM, (l) BF TEM and (m)-(o) DF TEM of the bottom of the NW ((m) WZ, (n) ZB<sub>A</sub> and (o) ZB<sub>B</sub>.)

The SEM images in fig. 4.11 (b), (k) and (h) of the tip, bottom and entire NW, respectively, shows the faceting. As was seen in regular TEM imaging, the average NW is straight and tapered from the bottom to the tip. The hexagonal shape of the NWs is visible in the image, as well as the faceting in the tip and bottom.

The image in fig. 4.11 is also a study of what kind of information the different imaging techniques gives about the NW. Clearly, SEM only gives morphological information. More interesting is the difference between BF STEM and BF TEM. When imaging the entire NW in fig. 4.11 (g) and (i) (STEM and TEM, respectively), only TEM gives any information about the defects in the NW. However, in the close up BF images of the top (fig. 4.11 (a) and (c)) and the bottom (fig. 4.11 (j) and (l)), defects can be seen with both techniques, but the contrast is better in TEM. Only TEM can give information about what type of defects are present. Figure 4.11 (d) - (f) and (m) - (o) are DF images of the tip and bottom, respectively, giving information about what phases are present. From these images one can see that a WZ segment is present in the tip and in the bottom, but that most of the other defects are twinning between the two ZB directions.

As mentioned previously, many of the variations between the NWs are concerned with the morphology. Figure 4.12 shows SEM images of the possible morphological variations in the bottom. Most of the NWs look like the one in (a), with a small tapering just before the end. The second most common type is the one seen in (b) with a clear narrowing a few hundred nm before the end. The segment after the narrowing is normally very rich in defect. The bump at the bottom of the NW seen in (c) is also quite common, and comes in many varieties.

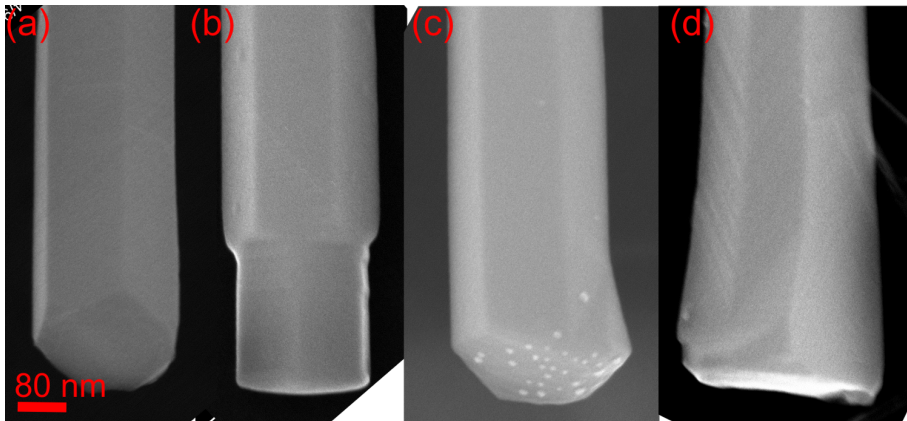


**Figure 4.12:** Variations of the faceting of the bottom of the NWs, as seen in SEM, ranging from the (a) most to (d) least common.

The wide bottom seen in (d) is only seen for a few NWs. The same information can be retrieved from TEM imaging, as seen in fig. 4.13. However, one loses information about the faceting, which is an important feature of the NW in fig. 4.12 (b), where the hexagonal shape is twisted about  $30^\circ$  with respect to the rest of the NW.

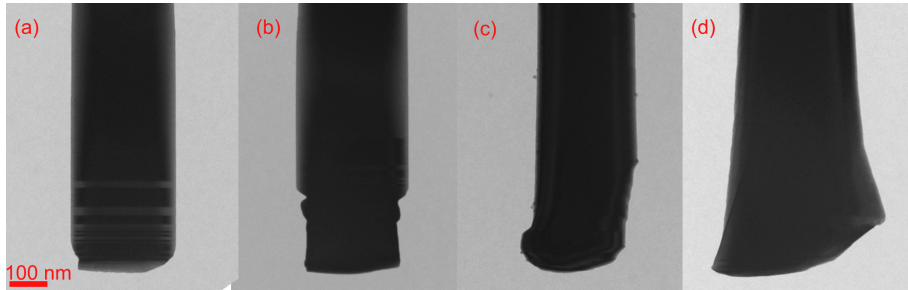


**Figure 4.13:** Overview of the variations in shape of the NW bottom, from most (a) to least (d) common. All four images are taken in BF TEM mode.

Figure 4.14 are SEM images showing the morphological variations in the tip of the NW. The most common shape of the NWs is the one seen in fig. 4.14 (a). The NW in the image has a slight decrease in thickness just below the tip, which is commonly observed in relation to a WZ segment in that area.

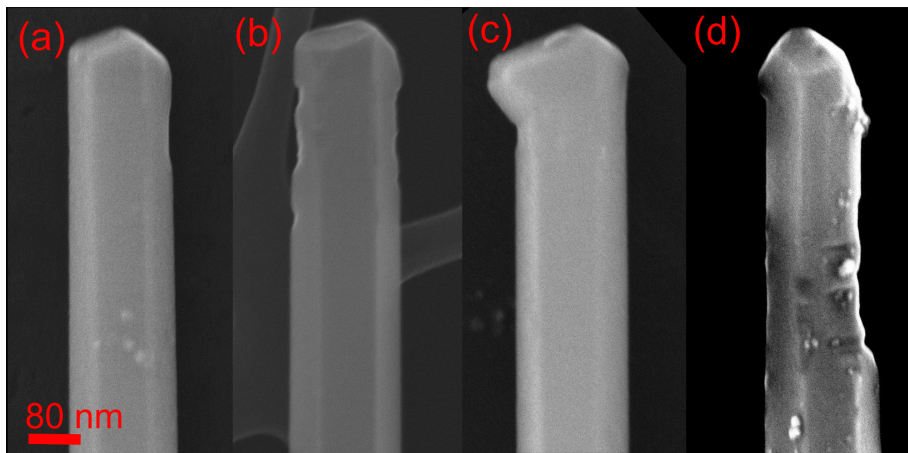


**Figure 4.14:** Variations of the morphology of the tip of the NW, as seen in SEM, from (a) most to (d) least common.

Several NWs show rough facets as seen in fig. 4.14 (b). The roughness is always in the segment below the tip, and can vary from just a little bit as in this image,

to a lot as seen in (d). Figure 4.14 (c) shows a NW with what looks like an incomplete catalyst droplet consumption. This is the least common type of variation seen in the tip of the NWs, not considering NWs with a very rough surface which is often a combination of the two (fig. 4.14 (d)).

### 4.4.3 Defects

The NWs on sample Main contain different types of defects that have been studied using HR TEM. Examples of the type of defects observed can be seen in fig. 4.15 - 4.18. Defects arise in three different areas of the NW: In the bottom, in the tip and in a segment below the tip. Figure 4.15 shows a fairly typical NW. It has a small WZ segment below the tip, about 13 nm thick, which is seen in (c). However, there are larger WZ segments further down on the NW. The presence of WZ is confirmed by the FFT in (e) which is taken from the dotted area in (c). The bright spots in the FFT are somewhat smeared out as short segments of both WZ and ZB is included in the area. Below the WZ there is a long segment with mixed phases and many planar defects such as SFs and polytyping. One edge is also a little uneven, which is seen in several NWs. From this image, it might seem like the thickness is changing with the type of phase observed along the NW. The tip above the WZ segment has defects in a different direction than the rest of the NW, which is also commonly observed. A close up of the defects are seen in fig. 4.15 (e), with an FFT of the dotted area in (f). As the FFT shows, there is only ZB present in the area of the defects, which might indicate that the defects are not related to SFs or a change in phase.

Figure 4.16 shows other types of defects that might be present in the very tip of the NW. As for the NW in fig. 4.15, there are defects in other directions than the one perpendicular to the growth direction. The defects forming the triangular shape observed here are seen in several NWs. The FFT in (d) of the dotted square in (b) shows that the material is oriented in two different directions, as indicated by different colors (yellow and blue). Each of the two directions show twinning, but in a different direction than normally seen for NWs. The arrows indicate spots that do not correspond to atomic planes in the crystal. The close-up image in fig. 4.16 (c) shows an interesting feature near the very tip of the NW. The dark lump seems to be several crystallographic directions on top of each other. The image also show two different growth directions of ZB, which is indicated by yellow and blue in (e) taken from the dotted square in (c).

As mentioned above, some NWs display what may look like an incomplete droplet consumption. This is observed for the NW shown in fig. 4.17 (a). (c) is a close-up of the tip, and shows only one diagonal planar defect, which is very little compared to the other two tips presented above. The FFT in (e) indicates that only one ZB phase is present in the image, thus the defect

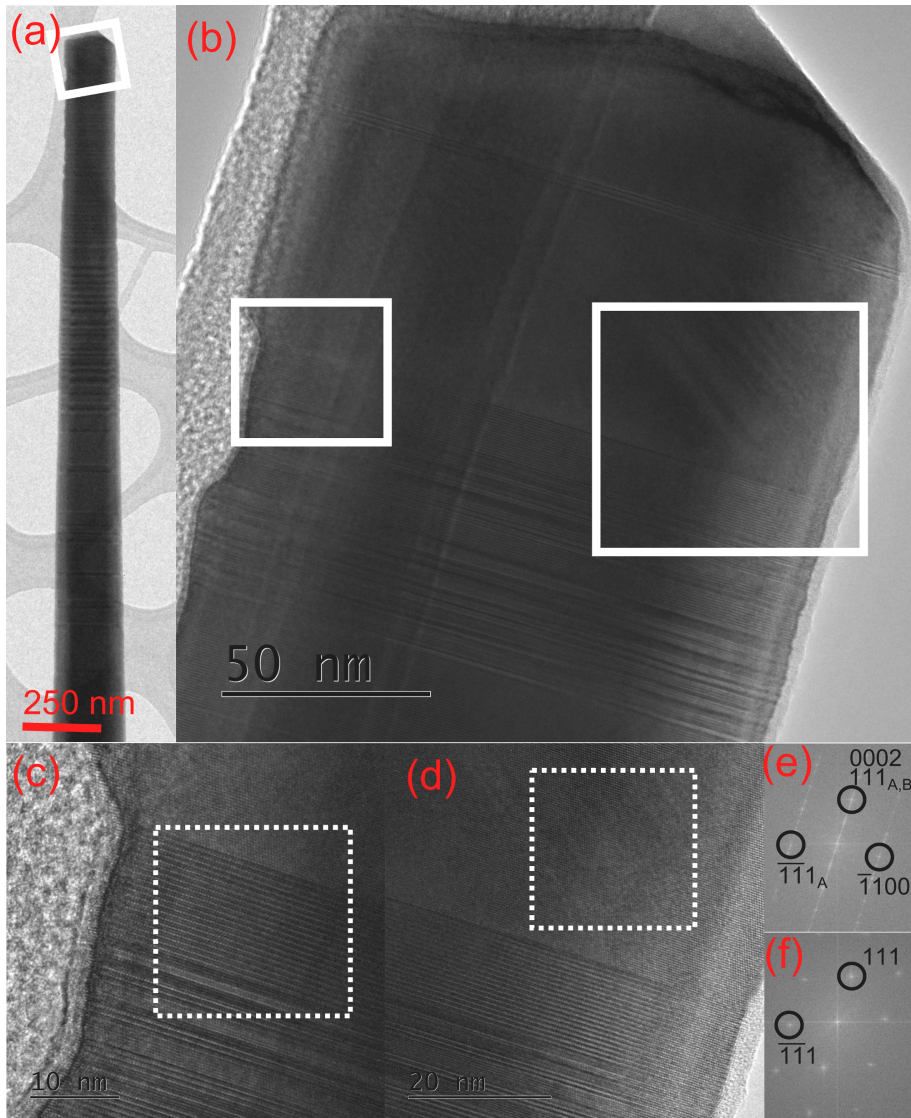


**Figure 4.15:** HRTEM imaging of defects in a NW tip. (a) BF image of the top part of the NW. (b) HR image taken where indicated by the white square in (a). (c) HR image taken from the left square in (b). (d) HR image taken from the right square in (b). (e) FFT from the dotted square in (c). (f) FFT from the dotted square in (d).

is probably a SF. The NW has a long WZ segment followed by a defect region

and a rough edge. The rough edge is seen in fig. 4.17 (b), and shows that there is no apparent connection between defects and faceting. The FFT in (d) shows smeared out reflections indicating that the segments of each phase is very short.

Figure 4.18 shows how the defects present in the bottom of the NW may look like. The imaged NW is one with a rather long defect segment (350 nm), but is typical for NWs with this shape in the bottom. (c) is a close-up of the defect rich area where the thickness of the NW changes, and the FFT from the indicated area is seen in (e). fig. 4.18 (b) is a close up from the bottom edge of the NW. At first glance, the pattern looks like the one from WZ, which is confirmed when indexing the FFT in (d) using the ratios listed [23].

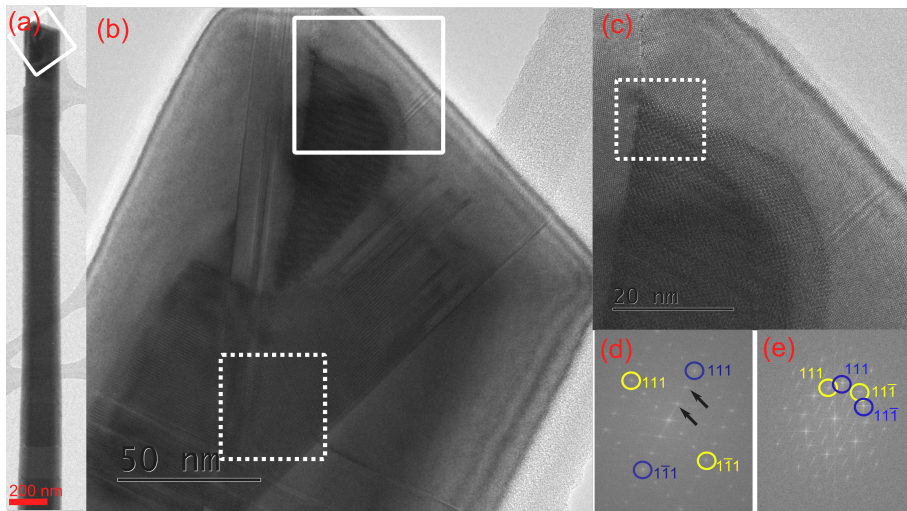


**Figure 4.16:** HRTEM imaging of a NW tip. (a) BF image of the top part of the NW. (b) HR image taken where indicated by the square in (a). (c) HR image taken from the upper square in (b). (d) FFT from the lower square in (b). (e) FFT from the dotted square in (c). Yellow and blue indicate two different directions of ZB that is not twinned with respect to each other. The arrows indicate spots that do not correspond to crystallographic planes.

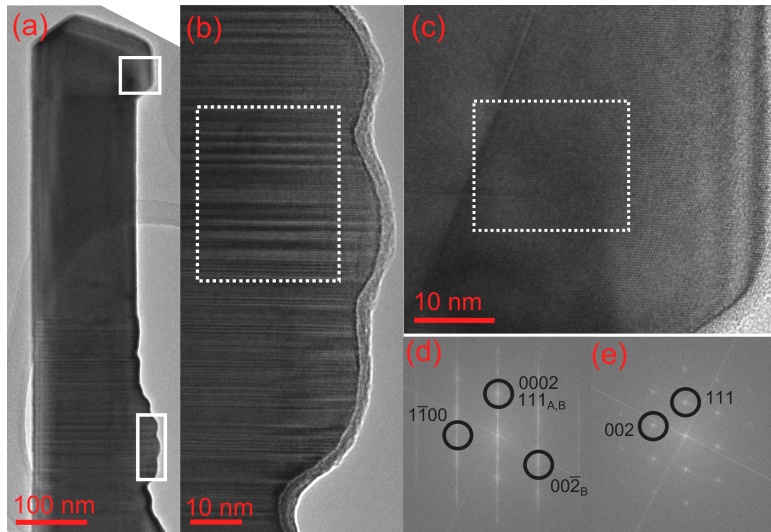


**Figure 4.17:** HRTEM imaging of a rough edge NW with what looks like an incomplete droplet consumption. (a) BF image of the tip area. (b) HR image from the lower square in (a). (c) HR image from the upper square in (a). (d) FFT from the area marked in (b). (e) FFT from the area marked in (c).

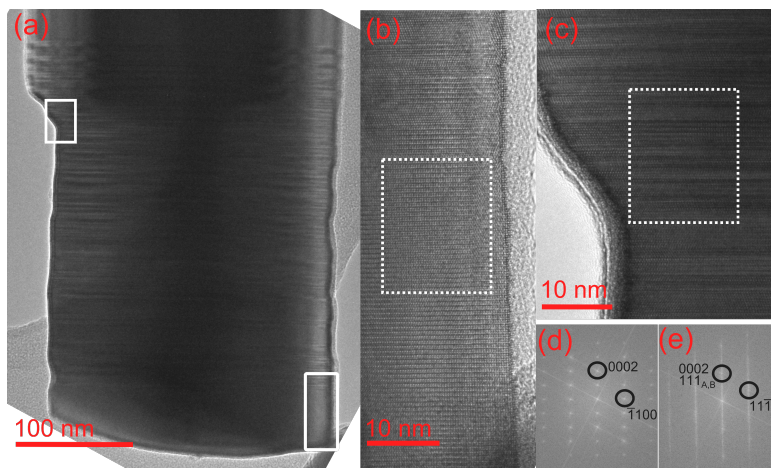


**Figure 4.18:** HRTEM imaging from the bottom of a NW. (a) BF image of the bottom. (b) HR image of from the lower square in (a). (c) HR image from the upper square in (a). (d) FFT from the area marked in (b). (e) FFT from the area marked in (c).

#### 4.4.4 Shell characterization

From comparing the BareCore sample with sample Main, it is clear that there are large differences in structure and morphology between NWs with and without shell. To get a better idea of the properties of the NW shell, around 15 NWs were characterized using HAADF STEM as well as EDX. Some of the NWs were also studied using HETEM, however, they are not correlated with the conventional TEM and PL characterization. This is because the PL-TEM study was done on SiN, which is not well suited for HRTEM purposes. As HAADF STEM shows both compositional and thickness contrast, it might be difficult to distinguish between facets and core-shell structure in the images. However, in combination with EDS, the two techniques will give a more accurate characterization.

Figure 4.19 shows HAADF STEM and EDS characterization of the same NW that is characterized using HRTEM in fig. 4.16. Figure 4.19 (a) and (b) are HAADF STEM images, while (c) and (d) are intensity profiles from the areas marked by yellow squares in (a) and (b). When looking at the intensity profiles, it is evident that the contrast is due to faceting of the NW, as the profiles are flat on top. The only exception is the profile from region B, which from HRTEM images are known to be a WZ segment area (not shown), where the facets are slightly tilted with respect to the rest of the NW. The difference between profiles D and E shows tapering of the NW in the bottom, as profile D is more narrow and less bright than profile E.

The EDS line scans in fig. 4.19 (e) - (h) gives a better picture of the core-shell structure of the NW. Scan (f) - (h), which is not from the tip, show the characteristic dip in the middle of the profile. However, as the scans are very noisy it is not easy to see if there is a corresponding increase in the Ga signal. In fig. 4.19 the Ga and Al signals follow the same profile, and therefore do not have a core-shell structure. From the line scans, the thickness of the shell seems to be changing between 30 - 50 nm, and the core-shell structure is not completely symmetric.

The red profile in all four scans shows Cu, and as this element is not present in any of the NW, it shows the height profile from where the scan is taken. Figure 4.19 (e) looks like it have a different hight profile than what the intensity profiles show in (c). However, it is only because the scan is done in the opposite direction.

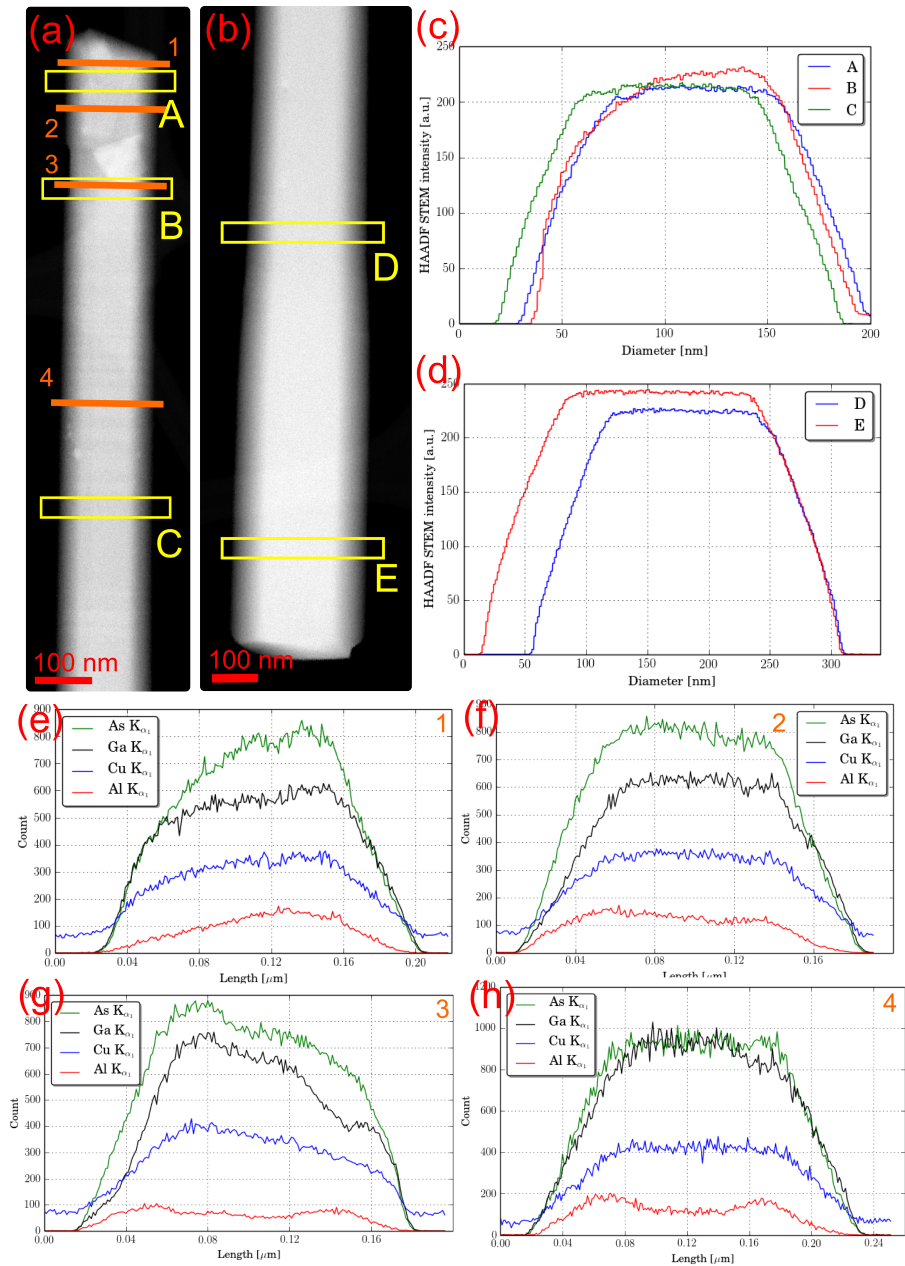


**Figure 4.19:** HAADF STEM and EDS characterization of a NW on sample Main from (a) the tip and (b) the bottom. (c) Intensity profile of the three areas marked in the tip. (d) Intensity profiles of the two areas marked in the bottom. (e) - (h) are EDS linescans from where indicated with orange lines in (a). This is the same NW as imaged by HRTEM in fig. 4.16.

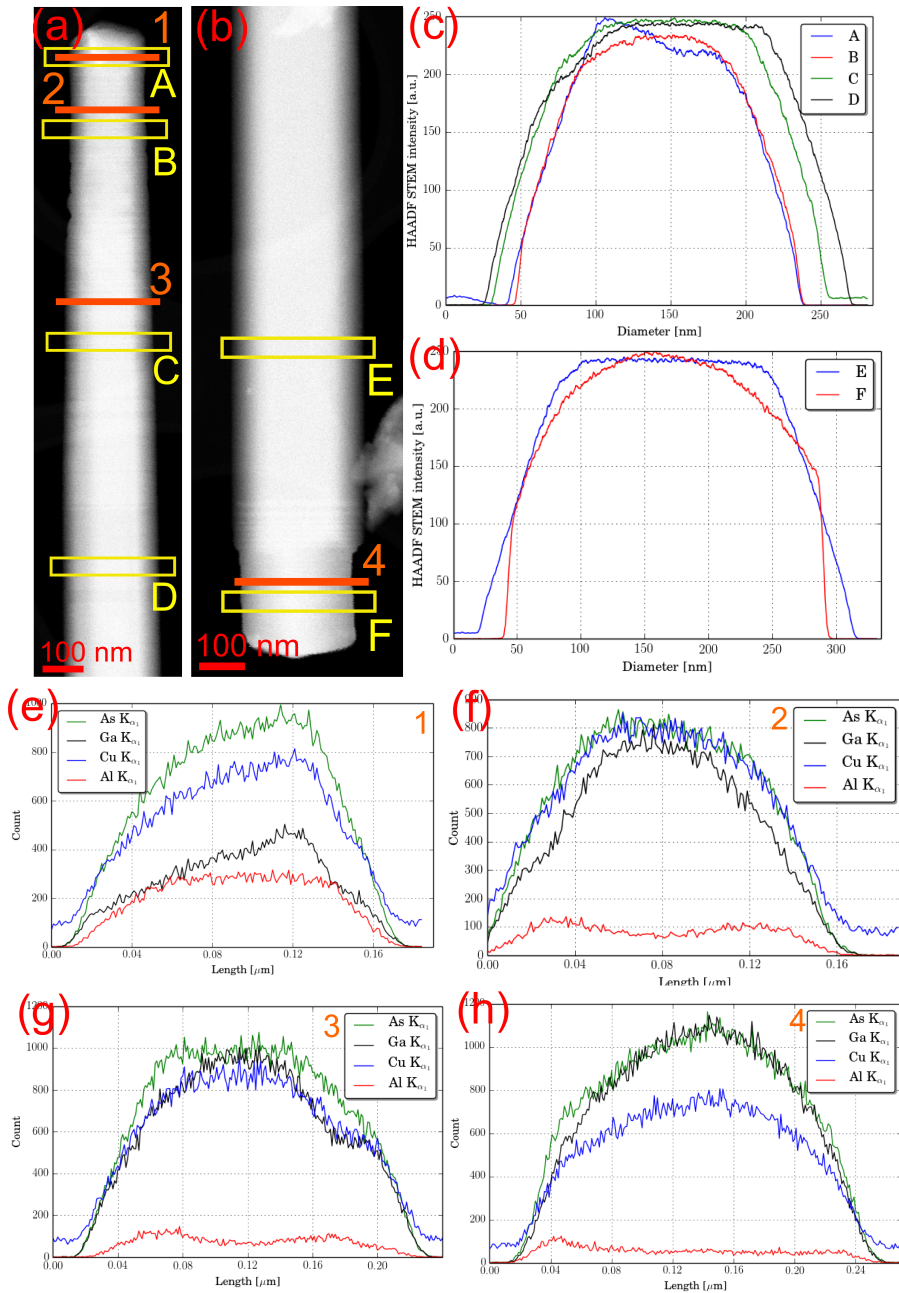
Figure 4.20 shows HAADF STEM and EDS characterization of a NW quite close to the average, except for some roughness in the tip area and a shape of the bottom only seen for a few NWs. As for the NW described above, it is not easy to see a core-shell structure from the intensity profiles in fig. 4.20 (c) and (d). Only profile D shows something that might be a core, but as the NW is a little off zone this is only seen on one side. Profile E and F are clearly thickness dependent, where F is on a different zone axis than E.

Figure 4.20 (e) - (h) shows EDS line scans from the lines marked in orange in the HAADF STEM images. (f) and (g) are from the middle of the NW and show a core-shell structure, while this is not observed in the tip (e). The bottom does show something that might be a very thin shell, about 20 nm. The Al content is clearly very low compared to Ga and As, and different from what is seen for the middle part of the NW, where the shell is found to be about 40 nm thick and quite symmetric.

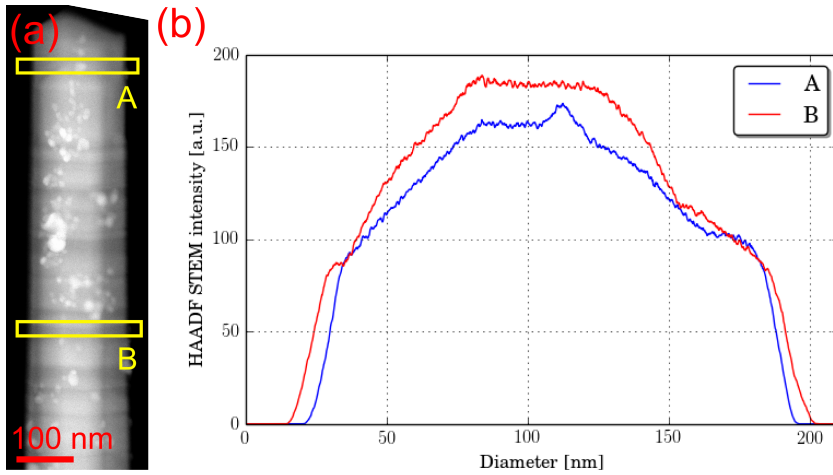
Profile A in fig. 4.20 (c) and the line scan in (e) looks like they are opposite from each other. However, as for the NW above it is the line scan being done in the opposite direction.

Figure 4.21 (a) shows a HAADF STEM image from the tip of a NW, with the appurtenant intensity profile in (b). From the latter, one can immediately interpret the contrast as due to the core-shell structure. This is because profile B has a stepwise shape. Profile A is from the tip and does not have the same shape, and the tip is therefore not core-shell. The abnormalities in the profiles are due to the contamination of the NW. An interesting note is that the core-shell structure in the NW is non-symmetric, as the core is located much closer to one side.

The HAADF STEM image of a different NW tip in fig. 4.22 (a) cannot immediately be interpreted as a core-shell structure contrast, as the profile in (b) does not have a clear stepwise shape. However, there is a very interesting feature in the tip in a diagonal direction. From the profile, it might look like a sudden change in thickness of the NW, but it might as well be a change in composition. It is possibly an AlGaAs rich area, and as was observed in the NW in fig. 4.15, the lines might be due to decomposition of AlGaAs in the shell.



**Figure 4.20:** HAADF STEM and EDS characterization of a NW on sample Main from (a) the tip and (b) the bottom. (c) Intensity profile of the three areas marked in the tip. (d) Intensity profiles of the two areas marked in the bottom. (e) - (h) are EDS line scans from where indicated with orange lines in (a) and (b).



**Figure 4.21:** (a) HAADF STEM image with (b) corresponding intensity profile from a NW showing an asymmetric core on sample Main.

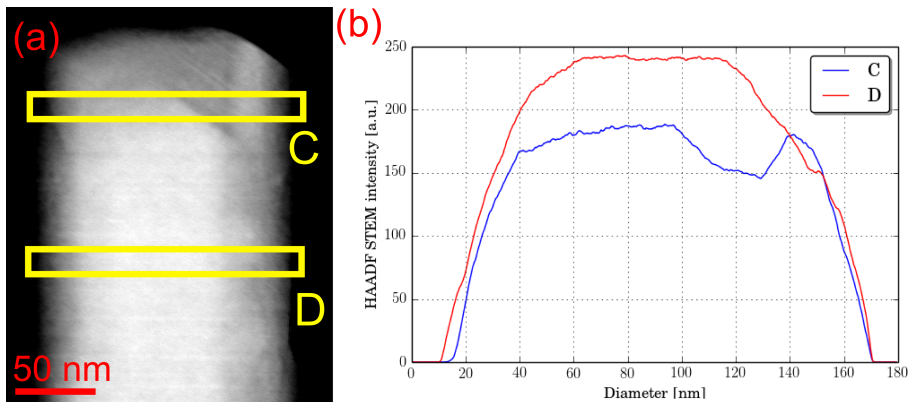


**Figure 4.22:** (a) HAADF STEM image and (b) corresponding intensity profile of a NW showing possible AlGaAs decomposition in the shell.

Figure 4.23 shows a EDS line scan along the length of a NW. The scan was done to see the changes in Al concentration in the NW, as the NW was grown with an axial AlGaAs core insert. However, this segment cannot be directly detected; the Al signal is constant until the very tip of the NW where it increases drastically. The thickness of the NW is decreasing steadily, as seen by the red line (which is Cu and not present in the NW), confirming tapering of the NW. The Ga and As signal, on the other hand, seem to start decreasing more rapidly about  $2 \mu\text{m}$  from the tip. As the Al signal is constant, the relative

concentration of Al is increasing. The profile in the tip is very representative for all the NWs; the Al signal goes up as the Ga signal goes down.

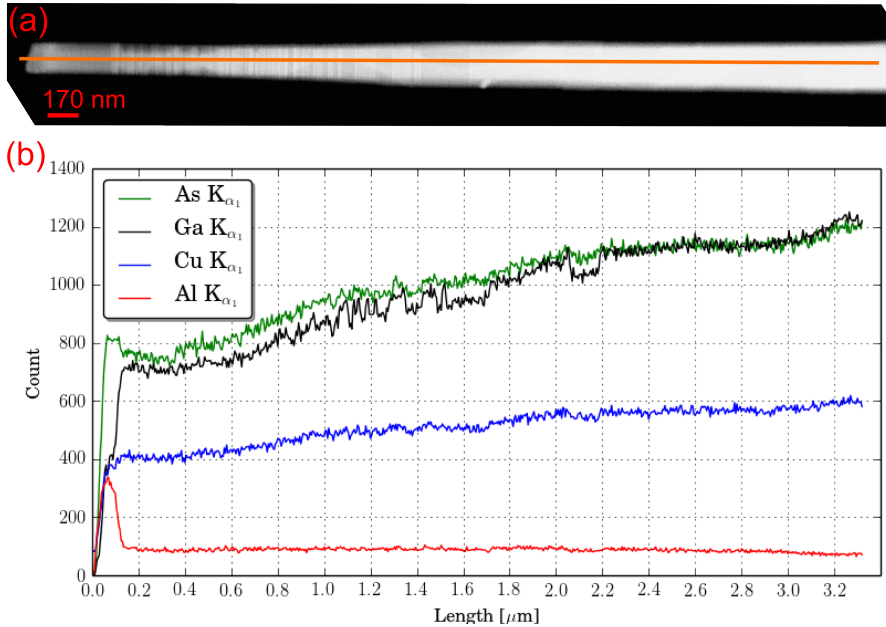


*Figure 4.23: EDS line scan of a NW on sample Main.*

## 4.5 Optical characterization

### 4.5.1 Sample Random1

The PL characterization of sample Random1 on SiN shows that most of the NWs have an emission peak at  $\sim 1.45$  eV which blue-shifts considerably with higher excitation power. NW 225 however, which was found to be structurally representative for the NWs studied, has a stable peak at  $\sim 1.45$  which does not blue-shift with higher power. Additionally, it shows a peak at  $\sim 1.48$  eV with a shoulder at higher energy, but this is not representative for the batch (fig. 4.24).

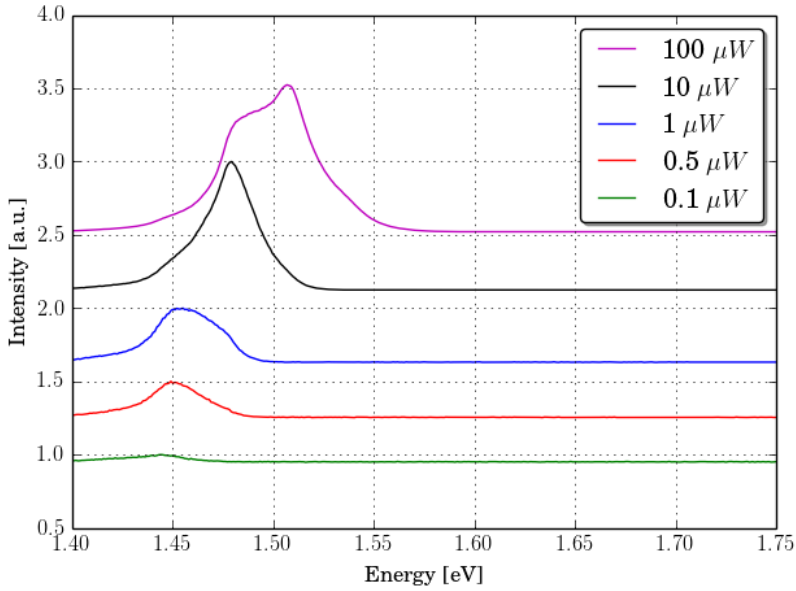


**Figure 4.24:** Power dependent PL spectrum for NW 225, a structurally representative NW on sample Random1. The spectrum is recorded with increasing excitation power.

## 4.5.2 Sample Random2

Despite the large variations in length of the WZ segment and mixed phase on the NWs on Random2, the PL spectra are very consistent. There is a broad emission peak at 1.47 - 1.48 eV as seen for the representative NW 311 in fig. 4.25. The peak does for some NWs develop a small shoulder peak to the low energy side (not shown).

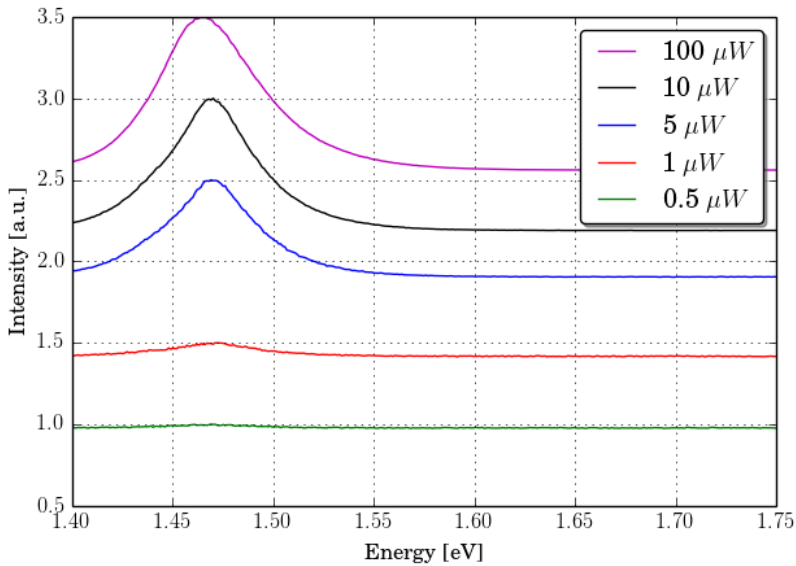


**Figure 4.25:** Power dependent PL spectrum for NW 311, a structurally and optically representative NW on sample Random2. The spectrum is recorded with increasing excitation power.

### 4.5.3 Sample Random3

For the NWs on sample Random3, the NWs had three considerably different types of structures. The power dependent PL emission spectra for these three NW types are presented below. Figure 4.26 shows the PL spectrum for NW 126 which did not have any WZ present. A clear peak at about 1.52 eV is visible and do not blue-shift with increasing excitation power. The peak does also have a shoulder at lower energy, about 1.495 eV.

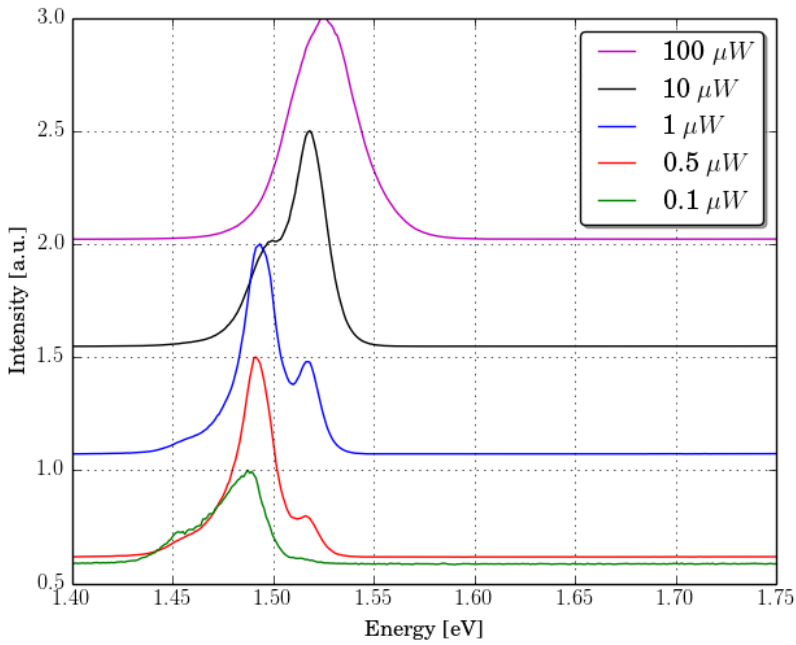


**Figure 4.26:** Power dependent PL spectrum for NW 126 on sample Random3, which does not have any WZ segments. The spectrum is recorded with increasing excitation power.

The spectrum in fig. 4.27, which is for the NW with a small WZ segment and a long mixed phase segment, is very similar to the one in fig. 4.26: A stable peak at 1.52 eV with a shoulder at 1.495 eV. However, the shoulder peak is a little more dominating for this NW than the one without any WZ segment.

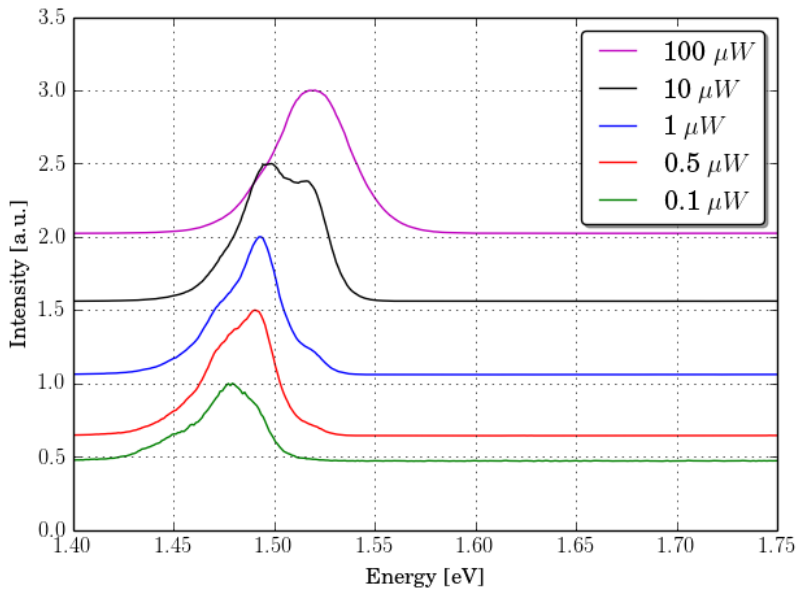


**Figure 4.27:** Power dependent PL spectrum for NW 127 on sample Random3, which has a short WZ segment and a long mixed phase segment. The spectrum is recorded with increasing excitation power.

The spectrum for NW 134 in fig. 4.28 is very different than the two others presented for this sample. This NW was different as it had a large WZ segment, but it does not show a stable peak at 1.52 eV. Rather, it has a broad, blue-shifting peak starting at 1.48 eV, making it more similar to the PL spectra for sample Random1 and Random2.

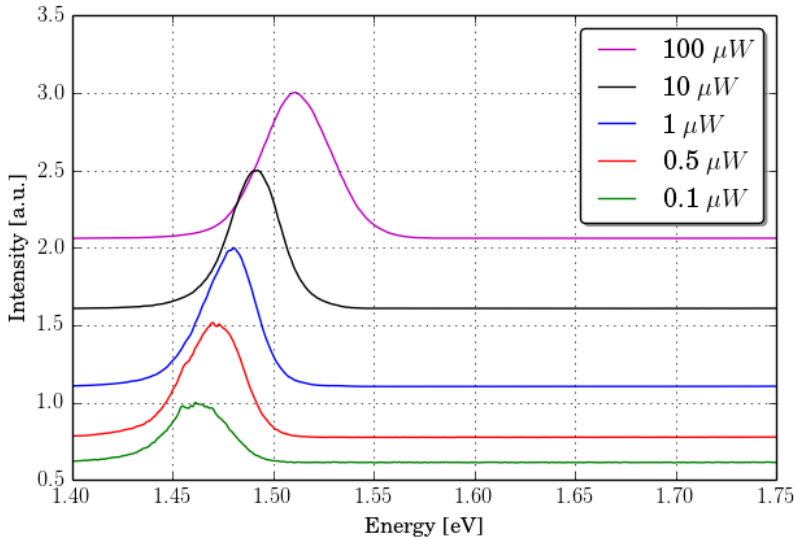


**Figure 4.28:** Power dependent PL spectrum for NW 134 on sample Random3, which has a long WZ segment as well as a mixed phase segment. The spectrum is recorded with increasing excitation power.

#### 4.5.4 Sample Main

30 NWs on sample Main was studied using PL, where 22 of them were correlated PL-TEM studies. The NWs showed very similar characteristics, and the PL emission spectrum for NW 212, the structurally representative NW shown in fig. 4.9, is presented in fig. 4.29. As was seen for all the NWs, NW 212 has a stable emission peak at about 1.51 eV, a little lower than the free exciton energy. The spectrum also shows a quite stable peak at about 1.48 eV, which is seen in most NWs. In addition to the exciton peak and the lower energy peak, many of the NWs on sample Main had one or more small higher energy peaks not seen for any of the Random samples. These peaks are normally in the range 1.6 - 1.8 eV, and for NW 212 there are two peaks at 1.69 eV and 1.71 eV, respectively. In the spectrum, these energy levels are saturated at the highest excitation power. However, this is not the case for all NWs.

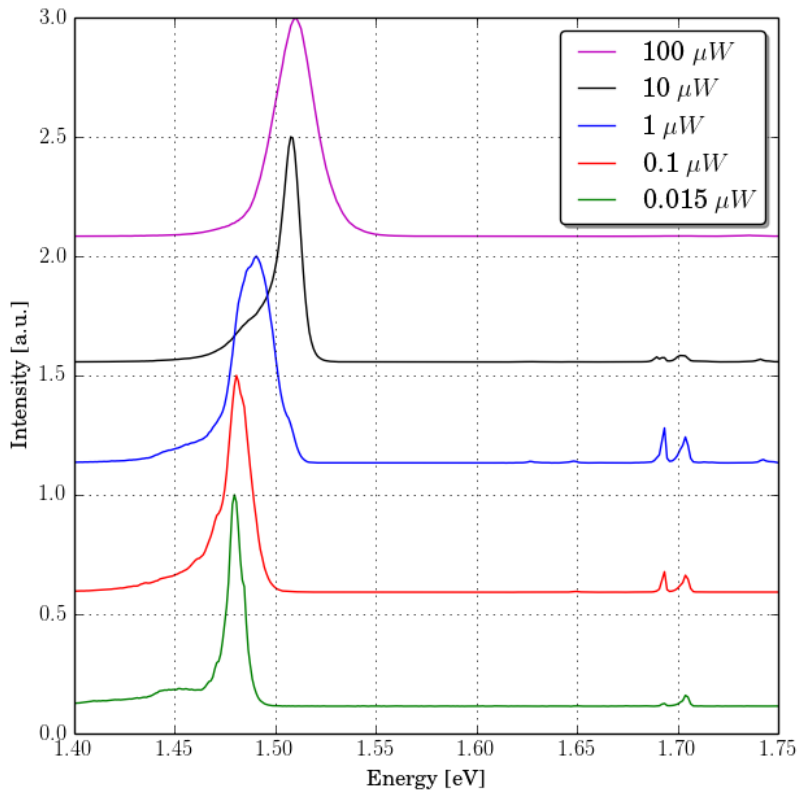


**Figure 4.29:** Power dependent PL spectrum for NW 212 on sample Main. The NW is representative for the structural properties of the NWs, and its characterization can be seen in fig. 4.9. The spectrum is recorded with increasing excitation power.

Not all the NWs had a high energy peak, and one of them is NW 125, seen in fig. 4.30. Rather, this NW has several low energy peaks around 1.45 eV that saturate at higher excitation power. However, these two types of peaks were not exclusive; some NWs had both, while others had only one or even non of them. NW 125 is very similar to NW 212 in structure and morphology, except for the bottom of the NW looking more like what is seen in fig. 4.13 (c).

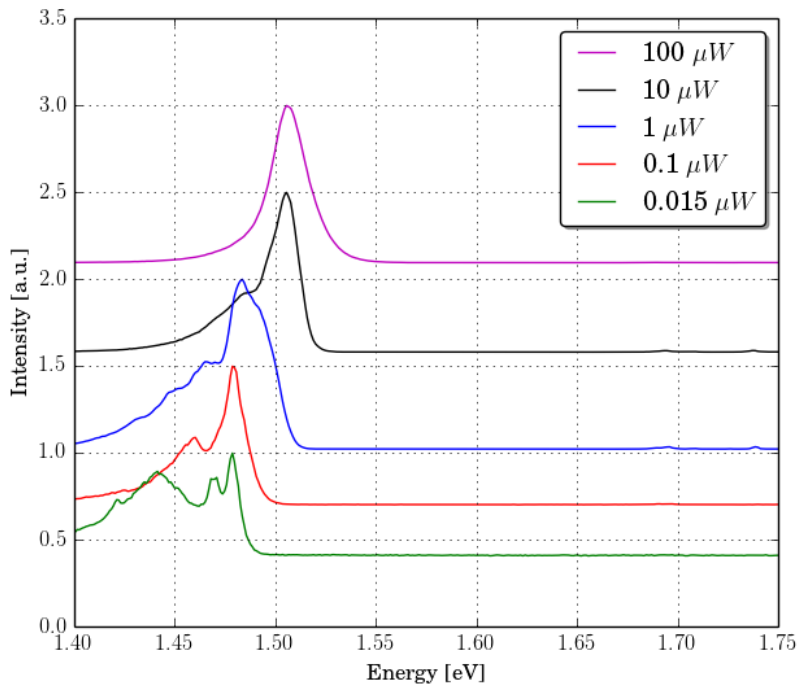


**Figure 4.30:** Power dependent PL spectrum for NW 125 on sample Main. The NW has a very similar structure as NW 212 presented in fig. 4.9. The spectrum is recorded with increasing excitation power.

# Chapter 5

## Discussion

In this chapter, the results presented in chapter 4 will be discussed. The aim of this work has been to find out whether the positioned grown NWs are more uniform than the NWs grown randomly on the substrate. In this discussion, four properties of the NWs will be considered: Their morphology, the shell growth, their crystal structure and defects, and their optical properties. In the end, a discussion comparing the techniques used will be presented, as it is relevant for the further work on this project.

### 5.1 Morphology

The NWs on samples Random1, Random2 and Random3 were characterized in TEM and findings about their morphology are interpretations of fig. 4.1-4.5. All NWs on the three samples have a similar morphology in the sense that they are straight, except for a narrowing related to the WZ segment. The tip part of the NWs are somewhat thicker than the rest, which might be related to an incomplete droplet consumption, or possibly a reforming of the catalyst droplet during shell growth. The thickness of the NWs on the three samples are different, which is likely related to the size of the droplet during growth. The droplet size decrease with increasing V/III ratio because a higher ratio leads to faster Ga consumption and a smaller equilibrium droplet [41]. This explains why the thickness of the NWs decrease with the increasing V/III ratio. The length of the NWs are somewhat arbitrary as it is not known where they have broken off during sample preparation, but overall the longest NWs are those with the highest V/III ratio (and therefore growth rate), even though an attempted to compensate for this was done by changing the growth time (see table 3.4). Also from the SEM image of the as-grown NWs on Random3 in fig. 4.6 (b) it can be seen that the length of the NWs are varying. The morphology of the NWs on sample Random1, Random2 and Random3 have

**Table 5.1:** Average length and thickness for the NWs on the five samples studied in this work, as well as the length of the different phases in the top and bottom. The Random samples rarely had their bottom intact for them to be characterized. Sample Main is listed with two different thicknesses which correspond to maximum and minimum as the NWs were tapered. Sample Random3 have two values for the WZ segment length as two different lengths seems to be equally common.

Sample	Length [ $\mu\text{m}$ ]	Thickness [nm]	Largest WZ segm. [nm]	Mixed phase segm. tip [nm]	Defect segm. bottom [nm]
Random1	3.2	200	160	180	na
Random2	4.4	160	140	400	na
Random3	4.0	140	420/100	563	na
BareCore	1.8	70	-	-	340
Main	5.1	166/295	37	314	104

also been thoroughly described in [42], where they were studied on graphene. The average length and thickness of the NWs on the three samples as well as sample BareCore and Main are listed in table 5.1 together with structural data to be discussed in a later section.

The NWs on sample Main were expected to be slightly different than the random grown NWs, as the growth conditions were changed in addition to the change from random to positioned growth (see table 3.2). The average NW on the sample is straight with a slight tapering from the bottom to the tip, while the random grown samples do not show any tapering. The average thickness of the bottom was found to be 300 nm, while in the tip about 170 nm.

Looking at the growth parameters presented in chapter 3, the droplet was consumed with a lower As flux in sample Main than in sample Random1, 2 and 3. In addition, it is grown an axial AlGaAs core segment in sample Main before the consumption process. However, as seen in fig. 4.11, the tapering seem to be present throughout the entire NW, and not start somewhere close to the tip where the AlGaAs segment and droplet consumption segment is expected to be found. The NWs on sample BareCore, on the other hand, which do not have a shell layer, are completely straight (fig. 4.8). This leads to the conclusion that the tapering of the NWs on sample Main are due to shell growth. However, this will be investigated more when the shell growth is discussed in the next section.

Another large difference between sample Main and the random grown samples is the shape of the tip. For all four samples, the Ga droplet was consumed for 10 minutes before shell growth, but with different As flux as mentioned above. For sample Main, the droplet seems to be fully consumed, as the thickness of the droplet is the same as the rest of the NW, while the tip on the random grown NWs looks like the droplet is completely consumed. However,

as the consumption of the random grown NWs are at a higher temperature and with a higher As flux, the consumption should have been faster than for the Main sample, suggesting that thicker tip in the Random samples is not catalyst droplet residues. It is possible that it is the subsequent shell growth that is causing the shape of the tip, and not the consumption of the droplet. For a random grown sample, the NWs can be grown very close to each other, and most of the gaseous growth species will reach the tip of the NW and diffuse further down. For lower temperatures, such diffusion will be slower, and more atoms will be incorporated into the structure in the top of the NW before they diffuse further away. As the temperature of the shell growth on the Random samples are lower than on sample Main, this might be a possible explanation. In addition, the positioned grown NWs have a larger average distance between them and therefore more of the growth species will be absorbed directly on the sidewalls of the NW.

As the NWs on sample Main are grown position controlled, it is possible to harvest them while keeping the bottom of the NW intact, whereas the NWs grown randomly are broken off at a more arbitrary distance from the bottom. This can be seen when comparing the structural images in fig. 4.1-4.5 of the Random samples with that of the Main sample (fig. 4.9) and the BareCore sample (fig. 4.7). The randomly grown NWs do not show any structural defects in the bottom, while twinning and a mixed phase segment is present for almost all the position controlled NWs (see also the structural data in chapter A). This is a great advantage as earlier, focused ion beam (FIB) had to be used for sample preparation if the bottom of the NW was to be characterized [43]. An indication that the NWs are all broken off in the interface between the substrate and the NW is that all NWs are very equal in length. The average length was found to be  $5.1 \mu\text{m}$ , ranging between  $4.6 - 5.5 \mu\text{m}$  (with two exceptions). This is also true for the BareCore sample, where the length varied between  $1.7$  and  $1.9 \mu\text{m}$ . For the random grown NWs that were broken off arbitrary, the difference could be several micrometers.

With the bottom of the NW intact for position controlled NWs, the morphology in this area was characterized in SEM (and TEM) for the BareCore and Main samples. The average NW on sample Main has a slight tapering in the bottom of the NW over a few tens of nm. The same type of tapering is also visible for the BareCore sample, indicating that the effect is due to the etched holes in the oxide mask not being perfect. An incomplete etching of the holes has been reported previously [21]. For several NWs the tapering is accompanied by a sharp edge, like NW 212 in fig. 4.9 presented as the representative NW on the sample. This might correspond to the thickness of the oxide mask, and that the NWs grow out of the holes in the oxide. As this is not visible in the BareCore sample, it is uncertain whether the holes in the oxide is filled during shell growth or whether the core of the NW fills the entire hole. This will be considered more in the next section when EDS is used to characterize

the cross section of the NW.

As the morphology of the random grown NWs showed to be quite uniform within a growth batch, this was expected for the positioned grown NWs as well. For sample BareCore, this is also the case. All the NWs look the same, with uniform thickness and the catalyst droplet intact. For the sample Main, however, there is a variation in morphology of the NWs. When the NWs are grown randomly, variations are expected because of differentiated growth conditions due to a shadowing effect. For the NIL samples, however, the growth conditions should be equal for all NWs on the sample. The morphological differences within the growth batch is found in the tip and in the bottom, as presented in section 4.4.2, and will be discussed next.

Several NWs have an area below the tip where the facets are rough and uneven, either on one or both sides. This roughness was not observed for any of the NWs grown randomly, therefore it is unlikely caused by an uneven flux of the growth species due to shadowing. The roughness is not present in the BareCore sample either, hence it does not occur during GaAs core growth. Accordingly, the roughness is most likely due to growth of the axial AlGaAs core segment, the consumption of the droplet or the shell growth. Both the shell growth parameters and the previously mentioned Ga droplet consumption is different for the Main sample and the three Random samples. Looking at the BF and DF images of the tip in fig. 4.10 (a-d), one can see that the rough area is limited to the mixed phase region. However, HRTEM images can prove that there is no correlation between changing phase and surface roughness (fig. 4.17 (b)). It does, however, look like there is no roughness connected to the longer WZ segment sometimes found below the droplet in the tip, and the thickness of the NW is many times sharply decreasing when this segment is introduced, and the roughness is in those cases below the straight WZ segment, as seen in fig. 4.17 (a).

A possible explanation for this might be that the high temperature during shell growth of the NWs on sample Main causes a faster and thereby more uneven shell growth, as the atoms do not have time to diffuse to the right place in the lattice. However, as mentioned above, the roughness is only present in the defect rich area. An explanation for this might be that the WZ phase, as the NW often is more thin in this area, have a slower shell growth than the ZB phase. As the atoms diffuse faster at higher temperatures, there will be a different flux of atoms in the areas next to the WZ area, causing changed conditions for growth. However, if the temperature is low enough, as in the Random samples, the atoms will not diffuse as far and the facets will grow more evenly. Also, there will be fluctuations within the mixed phase as the ZB facets will grow faster, enhancing the roughness in this area.

The variations found in the bottom of the NWs are more diverse compared to the variations in the tip. The most common variation is a NW with a bottom that is considerably less thick than the rest of the NWs, as in fig. 4.12 (b) and

fig. 4.13 (b). At a first sight one might relate this to the oxide layer on the patterned Si substrate, but as the narrow part is several hundred nm long, and the oxide layer is only a tenth of this, there must be a different reason for the abrupt change in thickness. As the thickness of the NW is related to droplet size, there might be fluctuations in droplet size causing the change, as the droplet might not have reached a stable phase and still be increasing in size in the beginning of the NW growth. However, this kind of change in thickness was not observed for the BareCore sample, although caution must be taken in making generalizations as too few NWs were characterized for the selection to be statistically significant. However, they all looked very uniform, which might indicate that the thickness change comes from the shell growth, and that the shell grows slower, or not at all, on the lower part. As can be seen from the SEM images, the hexagonal facets of the lower part is twisted  $30^\circ$  compared to the upper. If the upper part is oriented in the  $[110]$  direction, the lower part is oriented in the  $[112]$  direction. The change in thickness might be explained by the change in facets and perhaps a shadowing effect giving less shell growth, but the facet change is most likely be do to a large fluctuation in the growth conditions.

For some NWs, the bottom seems to be abruptly wider rather than tapered, as in fig. 4.12 (d) and fig. 4.13 (d). As this shape was not observed for the BareCore sample either, it is likely that it is due to uneven shell growth. It is possible for the AlGaAs shell to grow on top of the oxide layer, which has been observed in [21] (supporting information). Additionally, it seems unlikely that the Ga droplet has diminished in size before stabilizing. Some NWs has a little bump instead of a widening in the bottom (fig. 4.13 (d)). Looking at the image, it might look like the Ga droplet has drifted somewhat during growth, causing this effect.

To summarize, most of the NWs on sample Main are uniform in their morphology, except for some roughness in the facets in the tip most likely caused by shell growth. The NWs kept the bottom part intact during sample preparation, and characterization in this area show a varying structure most likely due to a combination of shell growth and an uneven etching of holes in the oxide layer.

## 5.2 Nanowire shell growth

An important part of the study of sample Main, was to characterize the shell to better understand the shell growth of the NWs, as there are large changes in structure and morphology after the core is grown. In the previous section, it was suggested that the tapering of the NW is mainly caused by an uneven shell growth. There is also a question regarding whether the rough facets are caused by the same reason or not. Also, the shape of the shell might be important for the optical properties, as will be discussed later.

The shell characterization using HAADF STEM and EDS confirm the presence of a core-shell structure of the NW. In the cases where thickness contrast dominated in HAADF STEM, EDS could confirm that the structure was present. Based on the intensity profiles for HAADF STEM and the element profiles for EDS (fig. 4.19 - 4.22), the shell was found to be between 20 - 50 nm thick, with the average being 40 nm. Most NW were found to be close to, but not completely, symmetric. For some NWs, however, the difference could be up to 20 nm, which means that the shell thickness could vary with up to 50%. In addition, EDS and HAADF STEM only looks at the projection of the NW. Thus, variations in the shell thickness is not necessarily present in the image and the asymmetry might be present in more NWs than observed. A possible explanation for the asymmetry might be that despite equal growth conditions, small fluctuations can lead to one facet becoming larger. Once it is formed, further shell growth will enhance this difference and the asymmetry will be enhanced.

As the average thickness of the NW in the tip is about 170 nm, a shell thickness of 40 nm means that the core is only 90 nm thick, which is close to the thickness of the NWs on BareCore. In other words, the shell constitutes almost 50% of the NW thickness, which is a considerable amount. If the NW core is straight all the way to the bottom, and the shell causes the tapered shape of the NW, more than two thirds of the thickness of the NW in the bottom is constituted by the shell. Thickness variations in the form of tapering seem to be related to the shell growth, but studies have claimed that it is due to a tapered core [21]. During growth, some of the species are deposited directly from the gas phase onto the NW surface. However, many of the atoms deposit on the substrate first, before they diffuse to the NW. In that case, the growth will naturally be larger in the bottom and cause tapering as the atoms will not diffuse far up on the NW before they are incorporated into the structure. The lack of tapering in the random grown NWs, which are located closer to each other and has a lower shell growth temperature, both limiting the surface diffusion, further supports this explanation.

In addition to the shell of the NWs, there is also a segment in the tip with pure AlGaAs. This non core-shell structure seen in all NWs is roughly 100 nm long, considerably longer than the thickness of the NW shell. Clearly, there is a difference in growth speed for the NW sidewalls and the tip, and there are two likely explanations for this. The AlGaAs growing in the tip grow in the  $[111]$  direction, while the shell on the sidewalls grows in the  $[1\bar{1}0]$  direction. As the growth is slower in the latter direction, it is also natural that the thickness of the shell on sidewalls is less than the axial AlGaAs segment in the tip.

However, when taking a closer look at the tip of the NW, the projection often shows two different facets in the growth direction as for example in fig. 4.19. In addition, the EDS and intensity profiles in fig. 4.19 - 4.20 shows an uneven thickness of the tip, indicating faceting in more than two directions. As men-

tioned above, some NWs display an incomplete consumption of the Ga catalyst droplet. Even though the consumption need not be as incomplete as this, there might be some part of the droplet left to catalyze the growth. Also, a small Ga droplet can reform in the tip when growing the shell as Ga has a very low melting point compared to the two other species [24]. In the case of a catalyst droplet, the shell growth will be faster in the tip as VLS growth is much faster than the VS growth on the sidewalls.

Another interesting feature of the AlGaAs shell is the possible presence of quantum wells in the shell, which was possibly observed in the HAADF STEM image in fig. 4.22. Earlier studies show the presence for such structures in AlGaAs/GaAs core-shell NWs, and that they are detectable in HAADF STEM due to the considerable difference in mass between Al and Ga [44]. The formation of quantum wells in the NW shell has two likely causes. First of all one has to consider the growth process of the NW. After the GaAs core has been grown, an axial AlGaAs core segment is grown before the consumption of the droplet. During axial growth of the NW, there will always be some unintentional VS growth on the sidewalls. Thus, some AlGaAs will be grown on the sidewalls when growing the axial AlGaAs core segment. When the droplet is consumed, GaAs will be grown on top of the unintentional AlGaAs layer on the sidewalls, followed by the AlGaAs shell. In other words, there will be one band of GaAs and one band of AlGaAs between the GaAs core and the AlGaAs shell in the NW. As AlGaAs represents a barrier, the GaAs band could cause quantum confinement if its thickness is in the nm range. A schematic illustrating a layer of confined GaAs in the AlGaAs shell can be seen in fig. 5.1.

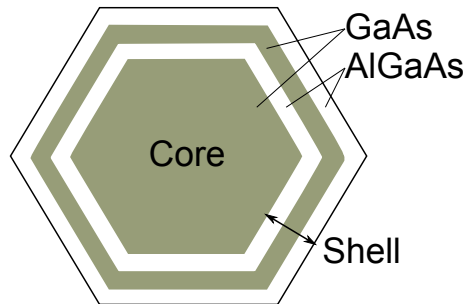


**Figure 5.1:** Schematic showing the cross section of a NW with a layer of confined GaAs in the AlGaAs shell, acting as a quantum well in the NW.

However, this does not explain the possible presence of nm sized bands in the tip of the NW. As this area does not have a core-shell property, it is formed during the shell growth and should therefore be pure AlGaAs. The contrast in the HAADF STEM image must either be explained by a change in thickness or mass, and a uniform AlGaAs composition would mean that the contrast is due

to a large height difference. However, the image in fig. 4.22 shows alternating bright and dark lines, indicating decomposition of AlGaAs in the shell into Al rich bands and thus the formation of quantum wells. This type of contrast is also very similar to what was found in [44]. If such quantum wells are present in the tip of the NW, it is likely that they are formed in the shell on the sidewalls of the NW as well. However, since the NW cross section both has a thickness and mass variation, such contrast will be smeared out. Also, it is observed that the corners of the NWs are more rich in AlGaAs [45,46], making as-grown characterization very difficult. Neither was it possible to detect the change in composition by EDS as the resolution is too poor to distinguish such small features.

As presented in fig. 4.23, attempts were made to see how the Al concentration were changing along the length of the NW using EDS. When doing the line scan, it was expected to see a change in Al concentration where the AlGaAs segment was grown, but as this change was not clearly detected, it is not sure if the attempt to grow the segment was successful. However, as the Ga and As concentrations are decreasing with decreasing thickness of the NW, the Al concentration is constant, indicating that the relative amount of Al is in fact increasing. The segment was meant to act as a barrier so that the defects in the tip area would not affect the optical signal. However, as will be discussed later, there are defect related optical emissions for some NWs indicating that even if the segment is there, it is not working as a barrier. Due to thickness and possible Al composition variations as well as the effect of crystal orientation, no quantitative EDS could be done.

To summarize, shell growth seems to be causing the variations observed between the NWs on sample Main and thus needs optimization. However, it is also a source of interesting, nanostructural properties that will be investigated further when discussing the optical properties of the NW.

### 5.3 Crystal structure, phases and defects

The crystal structure and defects of the NWs were studied by conventional TEM. The findings on Random1, Random2 and Random3 were in essence the same as studied previously in [42]. However, the most important aspects together with the new findings will be discussed here to shed light over the growth process both for the random grown and positioned grown samples. The findings for the Random samples are summarized in fig. 5.2.

The characterization on SiN confirmed the findings on graphene for all three samples. They all have a similar structure with pure ZB with some occasional twinning for most of the NW, with a WZ segment (for lengths see table 5.1) below the droplet in the tip and a mixed phase segment between the pure WZ and pure ZB segments. The mixed phase segment is rich in SFs and the layers of each phase are only a few nm thick. The twinning in the ZB phase

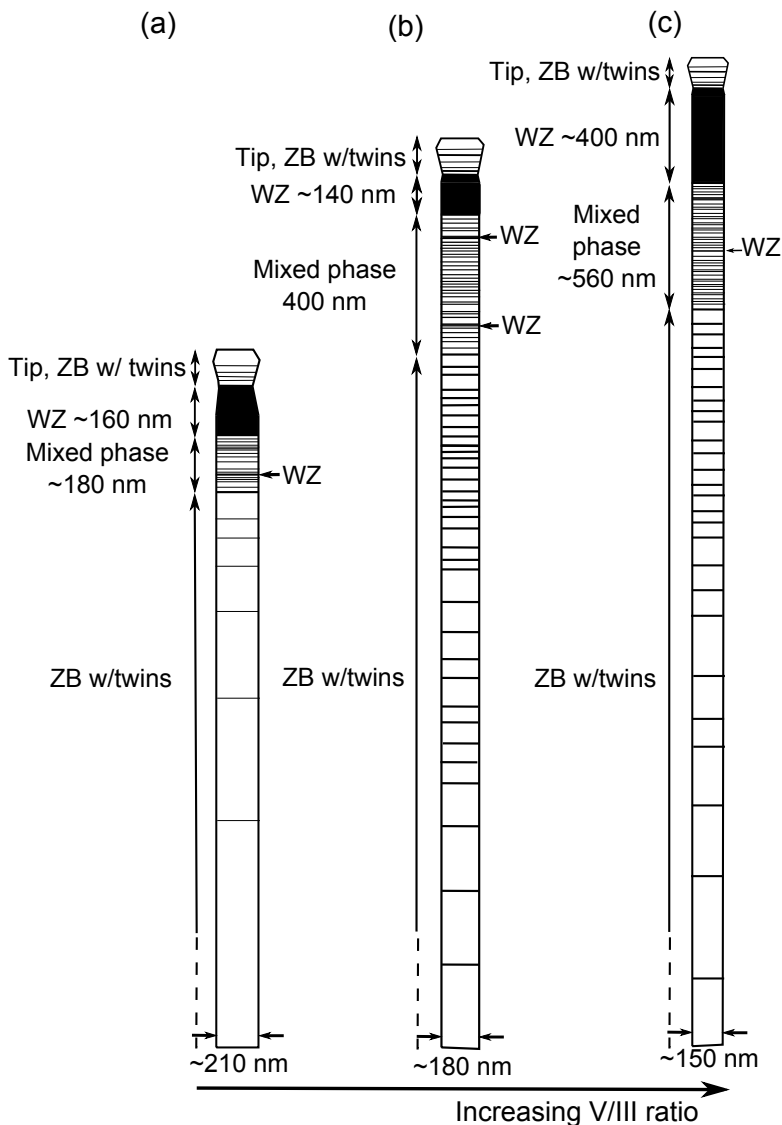


**Figure 5.2:** A schematic of the average NWs on sample (a) *Random1*, (b) *Random2* and (c) *Random3*. The WZ segment is indicated in black, while the mixed phase segment below is altering black and white. The lines further down and in the tip illustrate twinning. The thickness of the NWs are also indicated. For sample *Random3*, the NW is drawn with a long WZ segment. However, it might as well have been drawn with a short WZ segment as this was equally common.

is increasing with the height of the NW. Twinning is also present in the tip, but only in directions parallel to the growth direction. Defects in the bottom was only seen rarely, due to the NWs breaking off at a random height during sample preparation. The differences between the three growth batches are the length of the different segments and the amount of twinning in the ZB segment. Sample Random1 has the NWs with the least defects on average where both the WZ segment and the mixed phase segment is short, and the ZB segment has the least twinning of the average NWs on the three random samples. The average NW on sample Random2 does also have a short WZ segment, but the mixed phase segment is long and the ZB phase rich in twinning. For the NWs on sample Random3, the mixed phase segment was long as in Random2, but the length of the WZ segment was varying. Equal amounts of NWs with a long WZ segment as a short WZ segment was found. In addition, two NWs were found to not contain any WZ, which was not found for the NWs studied on graphene. Looking at the images of this NW in fig. 4.3, the tip is not wider than the rest of the NW as is the case for the other NWs. A possible explanation might be that the catalyst droplet fell off, thus preventing further growth.

It was suggested for the study on graphene that the mixed phase and WZ segment arises because of the termination process where the droplet gets consumed. The size of the droplet determines what phase is energetically favorable, where WZ will be favored for smaller droplets where the contact angle is lower [37, 47, 48]. The mixed phase arises as the two phases for a while during consumption will be approximately equally favorable for a certain droplet size. The difference in length for the segments is probably due to the size of the droplet when the consumption starts. For Random1, the droplet is larger and the supersaturation will be the lowest, therefore the droplet shrinks more slowly and will probably not reach the unstable size right away. For sample Random3, the supersaturation will be highest as the droplet size is smallest. The droplet will more quickly reach the phase where WZ is equally or more favorable than ZB. This will also explain the long WZ segment found in many of these NWs, however, it does not explain why the mixed phase region is differing in length. On the other hand, as the mixed phase is so much shorter in the NWs on Random1 than in the NWs on the two other samples, despite the growth rate being different for all three samples, it might indicate a threshold growth rate below which the precipitated molecules will have time to diffuse to the right position in the lattice.

Sample Main displays some of the same characteristics as the Random samples. Most of the length of the NW is pure ZB, with increasing defect density towards the tip. However, the ZB segment seems to have less twinning, and the tip area a higher density of defects. In addition, the defects in the bottom are visible. A schematic of the structure of the average NW on sample Main is shown in fig. 5.3. The average defect segment length in the bottom is 104 nm, with the longest being 250 nm and some NWs showing no defects at all.

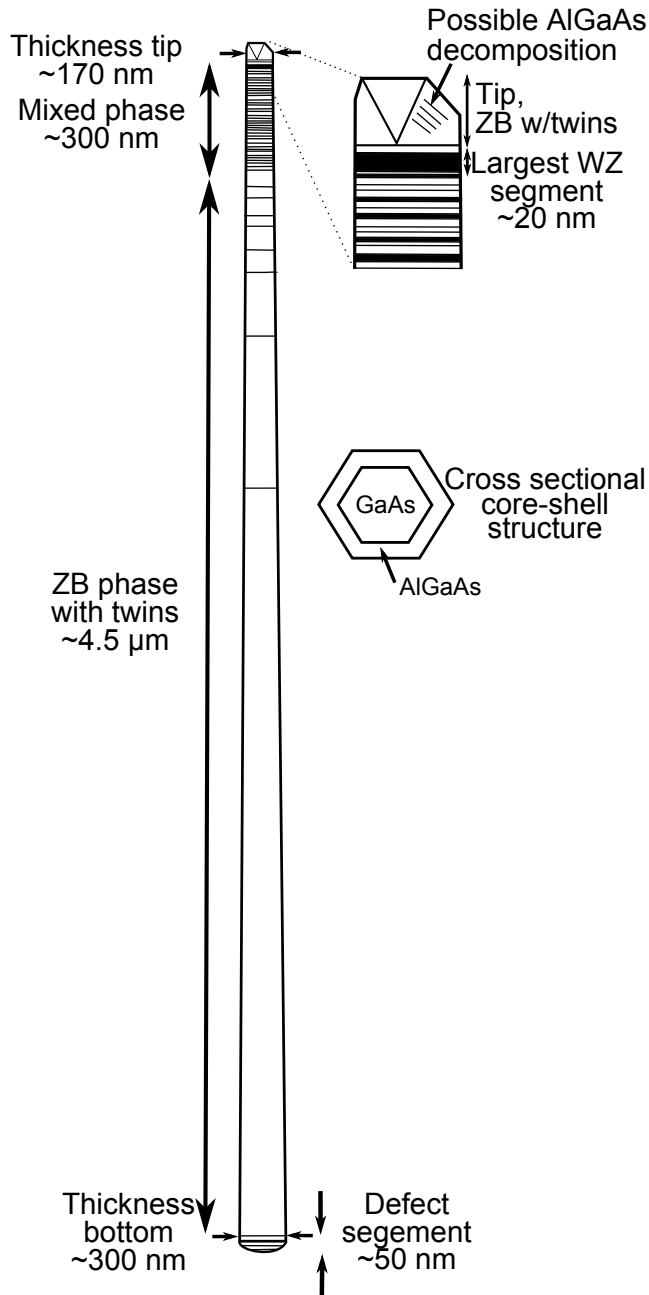


**Figure 5.3:** The figure shows a schematic of the average NW on sample Main, indicating the main structural features and their dimensions. The WZ segment indicated is the largest WZ segment in the NW.

The latter might be because the NW is broken off above the very bottom. The longest segments are found for the NWs having the shape seen in fig. 4.13 (b). The amount of WZ is varying, with more WZ towards the very bottom, but most of the defects are ZB twinning. This is also logical considering the findings on the random grown samples: In the very beginning of growth, the droplet has not yet reached equilibrium size, and if it is small enough the WZ phase will be present. Looking at the DF image in fig. 4.9 (k), the WZ is present only where the NW is tapered, i.e. not as thick as the rest of the NW, which further confirms the explanation. It was found that the NWs with the most WZ in the bottom also were the ones with a long, narrow segment like the one in fig. 4.13 (b), and the NWs with the least WZ in the bottom also were the widest ones.

Further up, there is a long pure ZB segment with occasional twinning. The twin density is increasing towards the mixed phase region which constitutes the last few hundred nm before the droplet in the tip. For most of the NWs, there were no distinct WZ segment found between the mixed phase and the tip. The average size of the largest WZ segment was found to be only 37 nm, not considering two larger segments of 200 and 110 nm, respectively (see structural data in table A.5). This average is considerably smaller than the smallest segments found on the Random samples. Some of the segments were only 10 nm wide, and in some cases there would also be some mixed phase between the WZ segment and the droplet in the tip. The mixed phase segment however, was on the same scale as what was found in Random2 and Random3. As for the Random samples, the mixed phase and WZ region in sample Main are probably due to droplet consumption. The mentioned differences might be due to different conditions during droplet consumption in addition to the changed growth conditions with the attempt to grow an axial AlGaAs core segment. When introducing Al in the core of the NW, the Ga flux was lowered at the same time to achieve the desired stoichiometry. By reducing the Ga flux to the half, a natural consequence would be shrinking of the droplet, as Al does not work as a catalyst in this case due to its high melting point. Thus, introducing Al in the core might cause WZ to be formed as the droplet shrinks making this phase favorable. The reason for the small WZ segment is more uncertain. As suggested previously, there are indications that AlGaAs does not grow as fast on the WZ facets during shell growth. It might be an indication that AlGaAs grow slower in the WZ phase during VLS growth as well, and because of the growth of the axial core AlGaAs segment in the NWs there will be less WZ than observed for the random grown NWs.

To better understand what is causing the defects below the tip of the NW, core-only NWs with similar growth conditions were studied as a reference. The growth of these NWs were terminated before droplet consumption, and as expected, they do not have any defects in the tip area, supporting the belief that droplet consumption causes defects. However, these NWs are quite short,

and it is likely that they would form defects when grown longer, as the Ga flux to the droplet also is dependent on surface diffusion. When further away from the surface this flux will be lower, thus inducing defects in the NW. In addition, these NWs do not contain any AlGaAs segment, still leaving the effect of changing the composition ambiguous. On the other hand, the NWs were rich in defects in the bottom. All the NWs studied had a very similar structure: First an almost defect free segment of WZ in the bottom with an average length of 164 nm. The rest of the NW consisted of almost defect free ZB, except for a segment between the WZ and ZB where both phases were present about 180 nm long. A summary of the structure of the NW can be seen in fig. 5.4. The structure in the bottom is quite different than the one found in sample Main, especially with the long WZ segment before the mixed phase. However, the NW was also grown with a lower As flux which might cause the Ga droplet to reach its stable size much slower, and the droplet size will be favoring WZ for a longer period of time than in sample Main in the beginning of the growth.

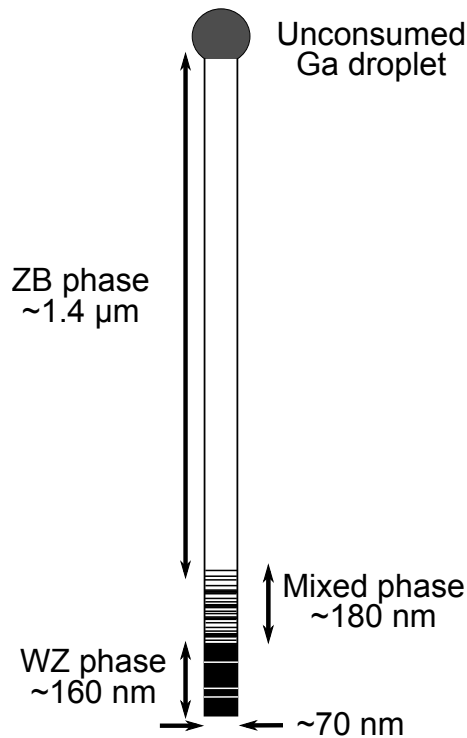


**Figure 5.4:** The figure shows the average NW on sample BareCore. The dimension of the segments of the different phases are indicated, as well as the thickness of the NW.

Another difference between the Main sample and the Random samples is the defects found in the tip. For the Random samples, only planar defects in the form of twinning in the growth direction are observed. For the Main sample, however, the twinning defects are in several NWs found in all possible [111]-directions, including in depth. This can be seen if studying the FFT in fig. 4.16 (d). In addition to that the pattern shows two different growth directions, the pattern itself is confusingly similar to a WZ pattern. However, if measuring the distance between the points in the FFT, it is not equivalent to that of WZ [23]. Rather, the FFT can be indexed as seen in the figure, and the points in between are  $\frac{1}{3}$  and  $\frac{2}{3}$  of the distance between the central spot and the (111) reflection. These spots do not correspond to an actual crystal plane, but rather an effect from two twin directions on top of each other, as described in [49] as well as [50]. As seen from the HAADF images of the tip, the area in the tip above the WZ segment does not have a core-shell structure. As was discussed in the previous section, the droplet might have several facets after consumption, and therefore when growing the shell layer there will be several growth directions.

On the same NW presented in fig. 4.16 and discussed above, another interesting defect is present. Looking at fig. 4.16 (c), it is evident that vertical defect neither is a twin nor a boundary between phases, but rather a grain boundary. It is possible that the catalyst droplet has not been fully consumed, but rather divided in two and then grown back together. This is also evident from the FFT in fig. 4.16 (e) of the interface between the two areas; they are not twinned with respect to each other, but oriented in two arbitrary directions. The area with a darker contrast in the image is what is giving rise to the third feature in the FFT. The pattern is probably due to a Moiré effect caused by several different crystallographic lattice directions [49].

A third type of defect observed in the tip and not seen in the Random samples is the one seen in fig. 4.15 (d). In an area that otherwise looks like ZB phase, which is also confirmed by the FFT in fig. 4.15 (f), alternating dark and bright bands are seen in what looks like the [110]-direction. If this was the direction for shell growth, a possible explanation for the observed contrast in the image is changing Al concentration arising from Al decomposition during shell growth. As a similar structure was found in HAADF STEM imaging (fig. 4.22), the observed contrast in the HRTEM images further confirms the quantum well hypothesis, as it is likely that the contrast in both imaging types are arising from the same structure in the NW.

Figure 4.18 shows a HR characterization of defects found in the bottom. As seen in SEM, the bottom part of the NW looks like it is oriented  $30^\circ$  different than the zone axis for the rest of the NW, which means that if the NW is on the [110] zone axis, the bottom part is on the [112] axis. Because of this, one can not directly interpret in HR image in fig. 4.18 (b), but when measuring the distances between the spots in the FFT in (d) and comparing with the values

in [23], the pattern is found to be from WZ with  $\{2110\}$  facets. However, if doing the same for the HR image from the WZ phase in the tip of the NW, which is seen in fig. 4.17 (a), one gets the same result, despite that the HAADF STEM intensity profile (fig. C.1) shows that the facets in the bottom are tilted with respect to the rest of the NW (i.e. both are on the same facets, grown in the  $[0001]$  direction). This could be explained by that for the ZB phase, a rotation of  $30^\circ$  would cost energy, and thus the  $\{2110\}$  facets are energetically preferred [51]. Further away from the bottom, a mixed phase structure is observed, (fig. 4.18 (c)). As both images is from an area of changing thickness, the interpretation is more challenging, but it is evident that in the beginning of the growth process, the droplet has not yet reached equilibrium size, making the WZ phase preferable.

To summarize, all NWs where the droplet have been consumed display defects in the tip area. However, when growing the NWs position controlled, these defects are more consistent from NW to NW. Defects and variations in morphology are also seen in the bottom. Non-planar defects are found in the axial tip segment grown during shell growth, probably caused by the high growth temperature as these defects are not seen in the Random samples.

## 5.4 Optical properties

As far as the final applications of the NWs are concerned, it does not matter what the NWs look like or if they are uniform or not, as long as the desired optical properties are consistent from NW to NW within the growth batch. In this case, the desired optical property is a stable, bright emission peak at about 1.52 eV coming from the free exciton. In this work, the main concern is to explain the observed emission with the results from the structural and morphological characterization. Even though the study of the samples Random1, Random2 and Random3 on graphene also discussed this topic [42], few certain conclusions were drawn, and the three samples will therefore be thoroughly discussed here as it might bring new insight to the argument, and provide understanding for the emission observed for the Main sample. Sample BareCore was not studied in PL as the lack of an outer shell gives a very weak emission.

On sample Random1, most of the NWs have a low energy peak at about 1.45 eV in the emission spectrum that blue-shifts with increasing excitation power. A possible explanation for this peak is the Ga-antisites, i.e. Ga on an As lattice position. These antisites are point defects working as an electron trap in the NW, and are arising from the Ga rich growth as the As flux is not high enough to make the growth stoichiometric, and since the As flux is increased for the two other NWs, this effect is expected to be less prominent. However, the peak does not blue-shift for all the NWs, suggesting that there might be a different explanation. Possibly, it might be due to the varying defect density within the mixed phase region. On the other hand, most of the NWs

does not show any emission at the free exciton energy, despite the presence of a long, seemingly defect free ZB segment which in theory should display such a property. Only two of the NWs measured on the growth batch, one of which is presented in fig. 4.24, have what might be the free exciton peak. The absence of emission at the exciton energy might be explained by recombination of the free exciton at non-radiative defects such as Ga-antisites. In any case, if this type of point defect is present it does not optically deactivate the entire NW, and it is difficult to conclusively assign any part of the emission spectrum to it.

The emission from sample Random2 is very consistent, but none of the NWs emits at the desired free exciton energy. Rather, they have a broad, quite stable peak centered at about 1.47 - 1.48 eV (fig. 4.25). A possible origin for this emission peak might be the mixed phase region of the NW. Although the NWs on the sample have a large variation in length of this region, the energy is consistent with quantum confined states arising from the structure being rich in planar defects [52]. The broadness of the peak can be contributed to the varying size of the microstructures in this region, and that the peak is the sum of all the individual contributions. Also for this NW, the absence of a free exciton peak might be explained by Ga-antisites, as this sample also is grown quite Ga rich. However, the NWs do not show any peak that might be the emission from this type of defect. This might indicate that there is no presence of such antisites, or that they are not emitting.

As the free exciton emission peak for WZ and ZB are very similar in energy, it is often difficult to conclude what is the origin of the observed peak when segments of both phases are present in the NW, as most NWs in the Random samples have. However, on sample Random3, two NWs were found to have no WZ segment at all (and thereby no mixed phase region either), but the spectra had a stationary peak at the free exciton energy at about 1.52 eV [53], as seen in fig. 4.26. The free exciton can therefore safely be attributed to the ZB phase. The same two NWs did also have a peak close to 1.5 eV. As there is no mixed phase in these NWs, this peak can not be assigned to quantum confinement between WZ and ZB segments only a few atomic layer thick, as it was for sample Random2. Rather, the energy level seems to fit well with the carbon acceptor level [54]. The presence of carbon is probably due to impurities coming from a contamination problem during growth in the MBE.

The other NWs on sample Random3 did have a WZ segment and a mixed phase region. The two NWs with a longer WZ segment had only one peak in the emission spectrum (fig. 4.28), and having an energy at about 1.48 - 1.49 eV, it is probably coming from the mixed phase region as was suggested for the NWs on sample Random2. The NW with the short WZ segment did also have the peak at  $\sim 1.49$  eV which can be explained by the same reasoning, but in addition it had a shoulder at higher energy that became more pronounced with higher excitation power (fig. 4.27). This shoulder at about 1.52 eV is probably

explained by the free exciton emission, but in this case the WZ free exciton can not automatically be excluded. Considering that the WZ segment is small compared to the pure ZB segment making up most of the NW, the signal is most likely coming from the ZB phase.

As sample Random3 is grown with the highest As flux of the three randomly grown samples, it is expected to have the least Ga-antisites. If the hypothesis that these antisites suppress the exciton signal due to recombination is right, the presence of an exciton peak in sample Random3 should mean that the antisite level is low enough to not affect the signal. However, a peak at the exciton energy was observed for sample Random1 as well, where the antisite level theoretically should have been too high. In addition, some NWs on sample Random3 did not have the exciton peak, despite that the antisite level should be low enough. This suggests that there are possibly other mechanisms controlling whether one has an exciton emission or not. On the other hand, these samples are grown randomly, and the fact that point defects are not detectable in TEM, there might be variations in the Ga-antisite level within each growth batch since the growth conditions are not equal for all the NWs on the sample. One could possibly measure the average signal for a large number of NWs, thus excluding NWs deviating from the average.

To avoid the problem of varying growth conditions due to variations in growth environment, the NWs on sample Main, which was grown position controlled, was studied in PL. The NWs were grown with the same As flux as sample Random1, but with a lower Ga flux, so the V/III ratio is more similar to the one for Random2 and Random3. From the structural appearance of the NW, it is also more similar to the NWs on these two samples, but the WZ segment is considerably shorter. On the other hand, the effect of an axial AlGaAs core segment in the NW is expected to have an effect on the PL spectrum not seen in the random grown samples.

The NWs on sample Main display three types of energy peaks: One or several peaks with energy below 1.5 eV, one stable peak at roughly the free exciton energy (about 1.52 eV), and one or several high energy peaks in the range 1.6 - 1.8 eV (see fig. 4.29 - 4.30). The exciton peak is stable and present for all the NWs, however, it does have a slightly lower energy than the free exciton energy found in literature [30], and there are some variations between the NWs. This could be consistent with studies showing a red shift of the exciton energy with increasing shell thickness due to strain imposed from the shell to the core [55]. According to the study, a 40 nm thick shell would give a PL exciton emission of 1.51 eV which fits well with the measured signal in this work. The variations between the NWs on the sample can be explained by fluctuations in the shell thickness both between the NWs and within the NW itself. Also, some of the NWs were observed to have an asymmetric core-shell structure, which will give variations depending on the wavelength of the laser beam used to excite the electrons. As most of the NWs does not have a

WZ segment of considerable length, the free exciton peak can quite safely be assigned to the ZB phase.

The broad range of peaks at lower energy (1.43 - 1.5 eV) are probably due to some kind of lattice defects that get saturated at higher excitation power. This could be either point defects or planar defects, however, the emission spectra show a different, sharper shape than what was observed for the Random samples. More precisely, the energy levels for Random1 and Random2 did not seem to saturate and had a much broader shape. For sample Main, the low energy peaks seems to saturate, except the peak at about 1.49 eV, which seems to be stationary and more pronounced at higher excitation power. This makes Main more similar to Random3, which has a sharp, stable peak at  $\sim 1.49$  eV possibly coming from deep carbon levels. As the peaks at sample Main are not consistent in energy level, this is not a certain explanation for this sample. It might also be coming from the mixed phase as observed for sample Random3, but then again it should have been broader.

The axial AlGaAs core segment was grown to act as an energy barrier between electrons excited in the pure ZB area and the defect area below the tip. The presence of low energy emission in the spectra indicates that this barrier is not successfully grown, which was also suggested from the characterization in HAADF STEM and EDS. On the other hand, these NWs have defects present in the bottom of the NW, which might be contributing to the signal. Thus, it is very difficult to say if the AlGaAs segment has an effect of the optical emission. A different sample preparation should be used where the defects in the bottom are not present to answer this question.

The main difference between the samples Main and the Random samples is the presence of high energy peaks, which was not observed at all for the randomly grown NWs. These high energy peaks are not present at a specific value, but ranging between 1.6 - 1.8 eV. They are not present for all the NWs on the sample either, and only pronounced for a few of them. Neither are they blue-shifting with increased power. It does not seem to be anything structurally different about these NWs; they are all very average looking and with no facet roughness. Two of them had a slightly larger WZ segment (50-60 nm), but nothing about these NWs that the other NWs didn't have could be found.

Two possible reasons for these high energy peaks have been considered, and both of them are concerned with the growth of an axial AlGaAs core segment. One possibility is that the signal is coming from the axial AlGaAs core segment itself, passivated with an AlGaAs shell with a higher Al content. According to [56], this kind of emission should be at roughly 1.8 eV, which is higher than what is observed for most of the NWs in this work. If this segment is pure and defect free, only one energy level should be observed, but these measurements show several peaks, all of them varying in energy from NW to NW. However, when this axial segment was grown, the Ga flux was reduced considerably when Al was introduced to achieve the desired stoichiometry. As mentioned earlier,

this will reduce the droplet size which in turn introduces defects in the AlGaAs segment. These defects could be a source for the observed variety in energy levels. On the other hand, as suggest above, a mixed phase structure most likely would give a broadening of the emission band rather than many different peaks. In addition, as discussed in section 5.2, this axial AlGaAs segment was not detected in EDS and it can thus not be concluded if it is present or not. Thirdly, the AlGaAs shell of about 100 nm in the tip constitutes a considerably axial AlGaAs segment that is expected to give a signal in the emission spectrum [57]. This is, however, not observed for the random grown NWs that are also expected to contain this segment [58].

On the other hand, both HAADF STEM and HRTEM characterization suggested that there might be decomposition of AlGaAs during shell growth which possibly can create quantum confined states in the shell causing the observed peaks in the spectrum. Alternatively (or additionally), it might be unintentional AlGaAs growth on the NW sidewalls during growth of the axial AlGaAs segment, also giving the same effect. Studies show that 4 nm wide quantum wells in the AlGaAs shell in core-shell NWs have an emission energy a little above 1.7 eV [59], which is consistent with the emission energies in this work. The varying energy levels of the peaks in the spectra could then be explained by a variation of the size of the GaAs layer in the shell, and several peaks might be caused by several layers of confined GaAs. As shell growth seems to be random for the NWs on the sample, it is also likely that the size of the quantum wells would vary between the NWs. If these energy levels come from quantum confinement, however, the peaks in the spectrum should be very sharp. This is the case for some, but not all the NWs having high energy peaks. In addition, the AlGaAs decomposition in the sidewall shell was not possible to see when characterizing the NWs as many other effects contributed to the image, leaving the question still ambiguous.

## 5.5 Method

A part of this work was to investigate the possibilities of using S(T)EM for mapping and screening of NWs. A more powerful mapping tool would make the correlated PL-TEM work more efficient since not that many NWs would have to be studied as the selection of NWs would not be at random. As mentioned previously, NWs exposed to 200 kV in a TEM are optically dead afterwards, and therefore the PL has to be done prior to structural characterization [57]. Attempts have been made at doing TEM at 80 kV, but it still seems to lower the signal when measuring the NWs in PL compared to before TEM exposure. The NWs are known to optically survive an acceleration voltage of 30 kV in the S(T)EM, and the attempts in this work was to see how much information about the structure and morphology of the NW could be extracted from this type of characterization tool.

The BareCore and Main samples were studied both in S(T)EM and TEM, and the images are displayed together in fig. 4.8 (BareCore) and fig. 4.11 (Main) for easier comparison. The NWs on sample BareCore are easier to image in STEM than the NWs on Main as they are much thinner, and therefore more transparent for electrons, a significant effect at low acceleration voltage. In addition to the NWs on sample Main being a little too thick for S(T)EM characterization, the S(T)EM only has possibilities for tilting in one direction, meaning that the NW cannot be tilted on zone unless it is positioned in the right direction compared to the tilting direction. For screening purposes, the work will be considerably easier with a specimen with many NWs to choose between, which is not always the case for a Cu/graphene PL-TEM specimen.

As can be seen from the images, it is possible to detect planar defects in the NWs in BF STEM mode at 30 kV. S(T)EM do not have diffraction mode to check if the NW is positioned on zone. However, it is possible to switch to SEM mode and look at the faceting of the NW to see how it is positioned. If the NW is located with the flat side down it should be close to the zone axis. But even if on zone, one can not be sure to detect all the defects as the NW might be too thick for the transmission of electrons, especially in the bottom where the NWs, depending on growth conditions, might be several hundred nm thick. Also it is not possible to tell what type of defect it is, e.g. if it is a twin or a WZ/ZB interface. However, if the sample has been screened using TEM beforehand, one has a general idea of what the NWs should look like, and one can make a qualified guess. For example, it would be possible to determine the size of the normally found WZ segment below the tip. As can be seen when comparing the images, fine details such as SFs are hard to detect in STEM, but this might not be necessary when one is only interested in the general idea of the structure of the NW. In addition, the morphology of the NWs can be characterized in SEM at the same time. For example, if facet rotation should be specifically studied in PL, these NWs could be found using S(T)EM.

If quantification of defects are not necessary, and one knows that the sample is homogeneous, as it should be for positioned grown NWs, characterization using S(T)EM can give a good enough image of the NW. In addition, one can screen the sample so that time is not wasted characterizing abnormal NWs, e.g. contaminated or broken, in PL.

# Chapter 6

## Conclusions

In this work, position controlled grown GaAs/AlGaAs core-shell NWs were studied using TEM, S(T)EM, HAADF STEM, EDS and PL to investigate whether position controlled growth gives more uniform structural and optical properties of the NWs. These NWs also had an axial AlGaAs core segment is grown before Ga catalyst droplet consumption. The properties of the NWs were compared with three samples of randomly grown NWs characterized in TEM and PL. In addition, a reference sample with position controlled grown, core-shell NWs was studied in TEM and S(T)EM to get a better understanding of the core growth process of the NWs in the MBE.

Both structurally and optically were the positioned grown NWs found to be more uniform than the NWs grown on random positions on the sample. All NWs on the Main sample were mostly pure ZB phase with some mixed phase ( $\sim 300$  nm) and a small pure WZ segment ( $\sim 30$  nm) below the tip probably formed during growth of the axial AlGaAs core segment and consumption of the droplet. Also, all NWs showed a good optical response as indicated by the free exciton peak in the emission spectrum, which was found to come from the almost defect free ZB segment. For the Random samples, the variations in the length of the different segments would vary considerably within a growth batch, and the excitonic behavior were only observed occasionally.

The structure and morphology of sample Main were different from the randomly grown samples in four different ways: (1) Tapering of the NW and rough faceting, which are due to an imperfect shell growth as well as the axial core AlGaAs growth. (2) Defects in the tip in different directions than the growth direction, probably caused by a high growth temperature during shell growth ( $630^\circ\text{C}$  vs  $460^\circ\text{C}$ ). (3) The presence of the defects in the bottom, whose variation in shape is due to an uneven etching of the holes in the oxide layer on the substrate. (4) A tip with the same thickness as the NW, probably an improvement due to the positioned growth.

Besides the consistently bright free exciton peak, the PL emission spectra

had two additional features slightly varying between the NWs: (1) Low energy peaks below the free exciton energy most likely coming from defects that saturate at higher excitation energy, while the peak at  $\sim 1.49$  eV might be a deep carbon acceptor level. The defects can either be Ga-antisites, planar defects or the alternating WZ and ZB phase in the mixed phase region. (2) High energy peaks in the range 1.6 - 1.8 eV, which has been substantiated that arise from quantum confined GaAs layer in the AlGaAs shell of the NW.

It is evident that growing NWs position controlled should be the preferred method of growth as they display less variations which makes it easier to understand how the growth parameters affects the final properties of the NWs. However, shell growth, catalyst droplet consumption as well as the beginning of the growth need optimization to give more uniform NWs. Further studies are also needed to shed light over still ambiguous questions concerning the growth process and the emission in the PL spectra. 30 kV S(T)EM should be the preferred tool for mapping NWs for PL-TEM studies as it makes the selection process and subsequent characterization more targeted, as defects and morphology are visible.

# Chapter 7

## Further work

Although the central question is answered in this study, further work is necessary to understand the different steps in NW growth and how the structure and morphology of the NWs affect their optical properties. In order to see the pure effect of growing the NWs position controlled, two samples should be grown, one positioned and one random, otherwise with equal growth parameters (flux, temperature, time, density). Only then can the effect of growing positioned NWs be fully understood.

It is also still uncertain what growth step contributes to the final structure and morphology of the core-shell NWs. One possibility is to not only study a core-only sample, but after each step in the process, i.e. after core growth, after the axial AlGaAs core growth, after droplet consumption and after shell growth, keeping the growth parameters the same all the way. Only then can it be certain whether the AlGaAs segment is grown or not, and if the shell growth is causing tapering and the rough facets. It can also be made clear how large the AlGaAs segment is, and how far the NW grows during droplet consumption.

Sample Main should be investigated further to clarify the possibilities of quantum wells. One possibility is to make a sample using FIB and study the cross section of the NW. With the use of HAADF STEM, HRTEM and quantitative EDS, a very precise characterization of the NW shell can be made. However, this is very tedious work as many samples have to be made in order to study an entire NW or several NWs. An easier approach would be to use HAADF STEM and EDS with the NW tilted to the [112] direction, which will give a better contrast. Also, several NWs with a rough facet should be studied to see if the roughness affects the signal possibly coming from confined GaAs, as these NWs would not have perfect quantum wells. In order to select only the desired NWs, S(T)EM should be used for the mapping process.

In addition, it is possible to analyze the already gathered data even further. PL measurements of bundles of NWs from sample Main have already been

conducted, and if the PL data from this single NW work is summed up, one could compare the two to gain a better understanding of the average properties of the NWs. If the average signal is similar to that measured for a bundle of NWs, and as positioned NW growth gives more uniform NW, PL from many NWs can be obtained easier and without any specimen preparation.

PL as done now, with a probe of about 200 nm, will excite large parts of the NW illuminated. This makes it hard to decide if the low energy signal comes from the defect region in the bottom or in the tip. Near-field scanning optical microscopy (SNOM) could be attempted to investigate where on the NW the different signals are coming from in PL. In SNOM, the light can be focused to only specific part of the NW, thus the signal will mainly come from that part of the NW, even though carriers might be able to diffuse far in a defect free material. For example, if the probe is focused on the defect free segment, and no low energy signal is detected, one can say with more certainty that this signal is due to the mixed phase in the tip, and not Ga-antisites. In addition, if there are high energy peaks in this area, it would be more likely that they are coming from quantum confined states in the shell, and not from the axial AlGaAs segment.

For the samples Random1, Random2 and Random3, advance PL data such as temperature dependent, polarization and lifetime measurements are available, but has not yet been processed. However, the structural characterization is already done in this work, and interpreting the advanced PL data in relation to the structure of the NWs can give more answers to emission observed for the samples presented here. It would also be interesting to do advanced PL on sample Main, for example to see if the free exciton emission is present at room temperature.

The findings in this work regarding structure and method development should be useful for future studies aimed at NW growth optimization and understanding the relation between the optical properties and the NW structure as determined by TEM techniques.

# Bibliography

- [1] Law, M., Goldberger, J. & Yang, P. Semiconductor nanowires and nanotubes. *Annu. Rev. Mater. Res.* **34**, 83–122 (2004).
- [2] Yang, P., Yan, R. & Fardy, M. Semiconductor nanowire: What's next? *Nano letters* **10**, 1529–1536 (2010).
- [3] Garnett, E. C. & Yang, P. Silicon nanowire radial p- n junction solar cells. *Journal of the American Chemical Society* **130**, 9224–9225 (2008).
- [4] Tsakalakos, L. *et al.* Silicon nanowire solar cells. *Applied Physics Letters* **91**, 233117 (2007).
- [5] LaPierre, R. Numerical model of current-voltage characteristics and efficiency of gaas nanowire solar cells. *Journal of Applied Physics* **109**, 034311 (2011).
- [6] Qian, F., Gradecak, S., Li, Y., Wen, C.-Y. & Lieber, C. M. Core/multishell nanowire heterostructures as multicolor, high-efficiency light-emitting diodes. *Nano letters* **5**, 2287–2291 (2005).
- [7] Bao, J., Zimmler, M. A., Capasso, F., Wang, X. & Ren, Z. Broadband zno single-nanowire light-emitting diode. *Nano letters* **6**, 1719–1722 (2006).
- [8] Hayden, O., Greytak, A. B. & Bell, D. C. Core-shell nanowire light-emitting diodes. *Advanced Materials* **17**, 701–704 (2005).
- [9] Colinge, J.-P. *et al.* Nanowire transistors without junctions. *Nature nanotechnology* **5**, 225–229 (2010).
- [10] Goldberger, J., Sirbully, D. J., Law, M. & Yang, P. Zno nanowire transistors. *The Journal of Physical Chemistry B* **109**, 9–14 (2005).
- [11] Bryllert, T., Wernersson, L.-E., Froberg, L. & Samuelson, L. Vertical high-mobility wrap-gated inas nanowire transistor. *Electron Device Letters, IEEE* **27**, 323–325 (2006).

- [12] Ning, C. Semiconductor nanowire lasers. *Chapter 12*, 455–486 (2012).
- [13] Duan, X., Huang, Y., Agarwal, R. & Lieber, C. M. Single-nanowire electrically driven lasers. *Nature* **421**, 241–245 (2003).
- [14] Johnson, J. C. *et al.* Single gallium nitride nanowire lasers. *Nature materials* **1**, 106–110 (2002).
- [15] Kavanagh, K. L. Misfit dislocations in nanowire heterostructures. *Semiconductor Science and Technology* **25**, 024006 (2010).
- [16] Dick, K. A. A review of nanowire growth promoted by alloys and non-alloying elements with emphasis on au-assisted iii–v nanowires. *Progress in Crystal Growth and Characterization of Materials* **54**, 138–173 (2008).
- [17] Mandl, B. *et al.* Growth mechanism of self-catalyzed group iii–v nanowires. *Nano letters* **10**, 4443–4449 (2010).
- [18] Garnett, E. C., Brongersma, M. L., Cui, Y. & McGehee, M. D. Nanowire solar cells. *Annual Review of Materials Research* **41**, 269–295 (2011).
- [19] Hochbaum, A. I. & Yang, P. Semiconductor nanowires for energy conversion. *Chemical reviews* **110**, 527–546 (2009).
- [20] Todorovic, J. *Correlated Transmission Electron Microscopy and Microphotoluminescence Studies of GaAs-based Heterostructured Semiconductor Nanowires*. Doctoral thesis, Norwegian University of Science and Technology (2012).
- [21] Munshi, A. M. *et al.* Position controlled uniform gaas nanowires on silicon using nanoimprint lithography. *Nano letters* (2014).
- [22] Kittel, C. & McEuen, P. *Introduction to solid state physics*, vol. 8 (Wiley New York, 2005).
- [23] Williams, D. B. & Carter, C. B. *The Transmission Electron Microscope* (Springer, 2009).
- [24] Callister, W. D. *Materials science and engineering, an introduction* (John Wiley & Sons, Incorporated, 2007).
- [25] Giacovazzo, C. *Fundamentals of crystallography*, vol. 7 (Oxford University Press, 2002).
- [26] Kelly, A. A. & Knowles, K. M. *Crystallography and crystal defects* (John Wiley & Sons, 2012).
- [27] Ramsdell, L. S. *Studies on silicon carbide* (Mineralogical Society of America, 1947).

- [28] Egerton, R. F. *Physical principles of electron microscopy* (Springer, 2005).
- [29] De Graef, M. *Introduction to conventional transmission electron microscopy* (Cambridge University Press, 2003).
- [30] Gilliland, G. Photoluminescence spectroscopy of crystalline semiconductors. *Materials Science and Engineering: R: Reports* **18**, 99–399 (1997).
- [31] Hemmer, P. C. *Kvantemekanikk* (Tapir, 2005).
- [32] Dupas, C., Houdy, P. & Lahmani, M. *Nanoscience: Nanotechnology and nanophysics* (Springer, 2007).
- [33] Quirk, M. & Serda, J. *Semiconductor manufacturing technology*, vol. 1 (Prentice Hall Upper Saddle River, NJ, 2001).
- [34] Wagner, R. & Ellis, W. Vapor-liquid-solid mechanism of single crystal growth. *Applied Physics Letters* **4**, 89–90 (1964).
- [35] Wu, Y. & Yang, P. Direct observation of vapor-liquid-solid nanowire growth. *Journal of the American Chemical Society* **123**, 3165–3166 (2001).
- [36] Glas, F., Harmand, J.-C. & Patriarche, G. Why does wurtzite form in nanowires of iii-v zinc blende semiconductors? *Physical review letters* **99**, 146101 (2007).
- [37] Cirilin, G. *et al.* Self-catalyzed, pure zincblende gaas nanowires grown on si (111) by molecular beam epitaxy. *Physical Review B* **82**, 035302 (2010).
- [38] Yeh, C.-Y., Lu, Z., Froyen, S. & Zunger, A. Zinc-blende–wurtzite polytypism in semiconductors. *Physical review B* **46**, 10086 (1992).
- [39] Adachi, S. *Properties of aluminium gallium arsenide*. 7 (IET, 1993).
- [40] Dheeraj, D. *et al.* Zinc blende gaassb nanowires grown by molecular beam epitaxy. *Nanotechnology* **19**, 275605 (2008).
- [41] Paek, J., Nishiwaki, T., Yamaguchi, M. & Sawaki, N. Catalyst free mbe- vls growth of gaas nanowires on (111) si substrate. *physica status solidi (c)* **6**, 1436–1440 (2009).
- [42] Nilsen, J. S. *The effect of the V/III ratio on the structural and optical properties of self-catalyzed GaAs/AlGaAs core/shell nanowires*. Project thesis, Norwegian University of Science and Technology (2013).
- [43] Munshi, A. M. *et al.* Vertically aligned gaas nanowires on graphite and few-layer graphene: generic model and epitaxial growth. *Nano letters* **12**, 4570–4576 (2012).

- [44] Kauko, H. *et al.* Compositional analysis of gaas/algaas heterostructures using quantitative scanning transmission electron microscopy. *Applied Physics Letters* **103**, 232111 (2013).
- [45] Rudolph, D. *et al.* Spontaneous alloy composition ordering in gaas-algaas core-shell nanowires. *Nano letters* **13**, 1522–1527 (2013).
- [46] Heiss, M. *et al.* Self-assembled quantum dots in a nanowire system for quantum photonics. *Nature materials* **12**, 439–444 (2013).
- [47] Munshi, A. M. *et al.* Crystal phase engineering in self-catalyzed gaas and gaas/gaassb nanowires grown on si (111). *Journal of Crystal Growth* (2013).
- [48] Krogstrup, P. *et al.* Impact of the liquid phase shape on the structure of iii-v nanowires. *Physical Review Letters* **106**, 125505 (2011).
- [49] Den Hertog, M. *et al.* Hidden defects in silicon nanowires. *Nanotechnology* **23**, 025701 (2012).
- [50] Cayron, C. *et al.* Odd electron diffraction patterns in silicon nanowires and silicon thin films explained by microtwins and nanotwins. *Journal of applied crystallography* **42**, 242–252 (2009).
- [51] Pankoke, V., Sakong, S. & Kratzer, P. Role of sidewall diffusion in gaas nanowire growth: A first-principles study. *Physical Review B* **86**, 085425 (2012).
- [52] Ba Hoang, T. *et al.* Engineering parallel and perpendicular polarized photoluminescence from a single semiconductor nanowire by crystal phase control. *Nano letters* **10**, 2927–2933 (2010).
- [53] Nam, S. *et al.* Free-exciton energy spectrum in gaas. *Physical Review B* **13**, 761 (1976).
- [54] Kim, H., Mair, R., Li, J., Lin, J. & Jiang, H. Time-resolved photoluminescence studies of al x ga 1-x n alloys. *Applied Physics Letters* **76**, 1252–1254 (2000).
- [55] Hocevar, M. *et al.* Residual strain and piezoelectric effects in passivated gaas/algaas core-shell nanowires. *Applied Physics Letters* **102**, 191103 (2013).
- [56] Singh, J. *Smart electronic materials: fundamentals and applications* (Cambridge University Press, 2005).
- [57] Todorovic, J. *et al.* Correlated micro-photoluminescence and electron microscopy studies of the same individual heterostructured semiconductor nanowires. *Nanotechnology* **22**, 325707 (2011).

- 
- [58] Zhou, H. *et al.* Wurtzite gaas/algaas core-shell nanowires grown by molecular beam epitaxy. *Nanotechnology* **20**, 415701 (2009).
- [59] Fickenscher, M. *et al.* Optical, structural, and numerical investigations of gaas/algaas core-multishell nanowire quantum well tubes. *Nano letters* **13**, 1016–1022 (2013).

# Appendix A

## Nanowire structural data

The structural data for each of the NWs studied in this work are given in table A.1 - A.5 below.

**Table A.1:** *Structural data for the NWs on sample Random1*

NW	Length [ $\mu\text{m}$ ]	Thickness [nm]	Largest WZ segm. [nm]	Mixed phase segm. tip [nm]
111	3.6	215	190	180
112	2.9	169	130	160
113	3.6	173	120	440
221	3.6	196	140	190
222	2.7	178	100	200
223	3.3	205	200	120
224	3.0	209	200	140
225	3.2	218	160	160
226	3.6	202	190	120
227	3.6	216	240	90
228	3.4	202	230	260
229	3.8	232	180	170
2210	2.5	201	190	140

**Table A.2:** Structural data for the NWs on sample Random2

NW	Length [ $\mu\text{m}$ ]	Thickness [nm]	Largest WZ segm. [nm]	Mixed phase segm. tip [nm]
111	5.1	183	130	120
117	3.9	162	250	520
311	4.2	150	50	580
312	4.0	136	590	530
313	4.9	175	150	50
314	4.2	263	450	490
315	4.1	169	120	930
316	4.5	166	170	240
317	5.0	178	130	100

**Table A.3:** Structural data for the NWs on sample Random3

NW	Length [ $\mu\text{m}$ ]	Thickness [nm]	Largest WZ segm. [nm]	Mixed phase segm. tip [nm]
126	4.6	146	-	-
127	4.9	144	100	670
132	3.9	103	-	-
133	3.6	157	400	500
134	3.0	149	440	520

**Table A.4:** Structural data for the NWs on sample BareCore

NW	Length [ $\mu\text{m}$ ]	Thickness [nm]	Largest WZ segm. [nm]	mixed phase bottom [nm]
1	1.9	70	170	110
2	1.8	70	170	180
3	1.9	80	100	250
4	1.7	60	170	150
5	1.7	70	210	190

**Table A.5:** Structural data for the NWs on sample Main characterized in BF and DF TEM.

NW	Length [ $\mu\text{m}$ ]	Thickness [nm]	Largest WZ segm. [nm]	Mixed phase segm. tip [nm]	Defect segm. bottom [nm]
122	5.1	190/280	30	200	250
123	5.0	170/300	20	300	79
124	5.1	160/280	20	170	30
125	5.1	170/350	30	200	50
211	5.1	160/380	10	300	60
212	5.0	160/270	20	300	100
221	5.1	160/320	30	640	50
223	5.1	150/310	20	190	100
225	5.3	130/300	na	na	na
226	4.8	170/270	20	350	120
227	5.5	170/300	90	0	70
228	5.2	160/400	50	500	50
231	5.5	180/290	50	200	60
232	5.6	180/300	60	0	40
233	4.6	160/290	20	650	110
234	5.2	260/260	20	230	100
311	5.2	170/290	20	170	60
312	4.9	170/290	20	230	180
313	5.1	170/290	10	330	150
314	4.9	160/310	110	450	40
321	5.2	200/290	20	330	220
322	5.3	170/260	70	400	70
323	5.6	160/300	50	220	100
325	5.1	160/320	20	490	160
326	5.2	270/310	80	140	60
327	4.9	190/280	70	530	120
328	5.2	250/270	60	160	140
329	5.1	170/270	50	340	80
331	5.0	160/280	200	500	270
332	5.0	160/300	20	330	100
333	4.3	170/240	80	0	0
334	3.9	160/240	10	250	na

# Appendix B

## Indexing diffraction patterns

Below, a method for indexing DPs obtained in TEM is given. The theory is based on [23].

When obtaining DPs in TEM, each reflection can be assigned to a set of planes in real space through certain fundamental and geometrical relationships. The distance between the direct beam and a diffracted spot in the DP,  $R$ , is related to the inter planar spacing in real space  $d$  by

$$Rd_{hkl} = \lambda L. \quad (\text{B.1})$$

Since the electron wave length  $\lambda$  and the camera length  $L$  is constant in a given DP, one knows that

$$R_1d_1 = R_2d_2 = R_3d_3 = R_4d_4\dots \quad (\text{B.2})$$

If the lattice parameter of the unit cell is known, some candidate  $d$ -spacings can be found. In reality, however, there is an error in  $R$ ,  $L$  and  $\lambda$ , which makes these candidates rather uncertain. The  $d$ -spacings can be checked if measuring the angle between the  $\mathbf{g}$ -vectors (for a cubic structure):

$$\cos \phi = \frac{h_1h_2 + k_1k_2 + l_1l_2}{(h_1^2 + k_1^2 + l_1^2)^{1/2}(h_2^2 + k_2^2 + l_2^2)^{1/2}} \quad (\text{B.3})$$

If combining (B.2) and (B.3), one can deduce the ratio method for a cubic lattice, used to determine the crystal structure and what zone it is indexed on:

$$\frac{R_1}{R_2} = \frac{d_2}{d_1} = \frac{\sqrt{h_2 + k_2 + l_2}}{\sqrt{h_1 + k_1 + l_1}}. \quad (\text{B.4})$$

When three  $\mathbf{g}$ -vectors have been found, the orientation or the zone axis of the material can be deduced. The indices of the zone axis  $[uvw]$  is defined by two lattice planes  $h_1k_1l_1$  and  $h_2k_2l_2$ :

$$\frac{u}{\begin{vmatrix} k_1 & l_1 \\ k_2 & l_2 \end{vmatrix}} = \frac{v}{\begin{vmatrix} l_1 & h_1 \\ l_2 & h_2 \end{vmatrix}} = \frac{w}{\begin{vmatrix} h_1 & k_1 \\ h_2 & k_2 \end{vmatrix}} \quad (\text{B.5})$$

when indexing DPs it is important to know that the zone axis is parallel to the incoming beam. This is true when the Weiss zone law is met:  $hU+kV+lW = 0$ . Three planes are known to have a common zone axis when they satisfy the relation

$$\begin{vmatrix} h_1 & k_1 & l_1 \\ h_2 & k_2 & l_2 \\ h_3 & k_3 & l_3 \end{vmatrix} = 0, \quad (\text{B.6})$$

which can be used as a check when indexing a DP that one is at the zone axis. When recording a DP, the most information is obtained when on a low-index axis.

## Appendix C

# HAADF STEM imaging

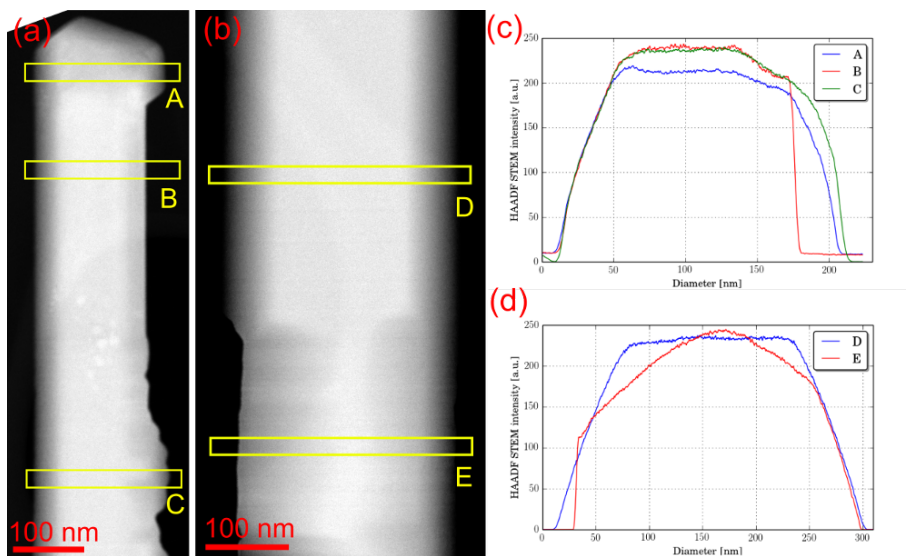


*Figure C.1: HAADF STEM characterization of a NW on sample Main. The NW shows rough facets in the tip (a) as well as twisted facets in the bottom (b). (c) and (d) are intensity profiles from the areas marked in (a) and (b).*